THIN FILM COATINGS WITH ULTRA–HIGH STABILITY FOR PRECISION GLASS MOLDING

AWAIS AKHTAR

PhD

THE HONG KONG POLYTECHNIC UNIVERSITY

2023

The Hong Kong Polytechnic University

Department of Mechanical Engineering

Thin Film Coatings with Ultra–high Stability for Precision Glass Molding

Awais Akhtar

A Thesis Submitted in Partial Fulfilment of the Requirement for the Degree of Doctor of Philosophy

August 2022

Certificate of Originality

I hereby declare that this thesis is my own work and that, to the best of my knowledge and belief, it reproduces no material previously published or written, nor material that has been accepted for the award of any other degree or diploma, except where due acknowledgement has been made in the text.

_____ (Signed)

Awais Akhtar (Name)

Abstract

Precision glass molding (PGM) is an advanced glass manufacturing technology employed by the glass industry for the high-volume production of precision glass components. One of the key breakthroughs is the use of anti-sticking coatings that extend the tool life and render a molded glass surface polish-free. The improvement in oxidation resistance and anti-sticking performance of coatings is a major challenge, particularly when the PGM technology is to be adapted for thermoforming of glasses with high glass transition temperature (T_g). In this thesis, first, a systematic review was conducted, and the recent developments and progress of surface protective coatings for PGM applications were summarized. Specifically, the most important and recent breakthroughs in deposition processes, microstructural features, and anti-sticking performance were emphasized, as they establish the foundation for developing high-performance thin film protective coatings for thermoforming high-T_g glasses in PGM. Furthermore, based on these explorations, a perspective for further improving the reliability of PGM coatings was also provided.

Second, a new multilayer Ru–Pt coating design on graphite substrate was developed to evaluate its performance in PGM applications. Different from previous evaluations with other types of coatings for PGM temperatures below 650 °C, the anti-stick behavior of the developed coatings was studied by annealing them at 750 °C with aluminosilicate glass (ASG) coverage in a rough vacuum environment. Glass adhesion was not observed even after 40 h of annealing, suggesting the high chemical inertness of these coatings at high temperatures. In addition, Ru–Pt multilayer coatings exhibited a better anti-sticking property than monolayer (Ru or Pt) coatings.

The microstructure, surface morphology, and hardness were further characterized. High-resolution transmission electron microscopy (HRTEM) analysis confirmed the preservation of the layered structure after annealing at 750 °C and the hindrance effect on dislocation motion and diffusion arising from the Ru–Pt interfaces. After long-term annealing, interdiffusion led to Pt–Ru solid solutions, which further enhanced the mechanical performance and stability of the noble metal coatings, which are beneficial for prolonging the lifespan of PGM molds and the optical quality of molded glass. The high anti-sticking and mechanical performances of the developed coatings were confirmed in industrial tests.

Finally, considering the high performance of Ru-based coatings, the concept was further extended, and another cost-effective coating design was prepared by deposition of Ru–Cr coatings on graphite substrates to examine its feasibility for the PGM industry. Ru–Cr coatings with varying Ru thicknesses were fabricated, revealing columnar morphology with preferred orientation and the effect of annealing on the microstructure and mechanical properties of the developed coatings at the desired molding temperature (750 °C) for different time durations (10–20 h) was studied. The outward diffusion of Cr and its preferential oxidation to the Cr-oxide scale resulted in the improvement of mechanical properties of the coatings. Furthermore, the nanostructure characterization revealed the expansion of the Cr coating layer and Ti interlayer and the disappearance of the Ti–Cr interface, indicating the formation of Ti–Cr alloys. In contrast, the Ru thickness remained unchanged after annealing, indicating stability. In addition, the TEM investigation demonstrated that Ru–Cr coatings with increased Ru thickness inhibited the outward movement of Cr and served as a diffusion barrier. Furthermore, phase field modeling data validated

the experimental findings and showed that the varied Ru layer thickness impeded outward diffusion of Cr at different degrees and demonstrated external oxide scale stability after annealing.

Overall, the findings of this thesis provide insights into stable coating materials with high performance for PGM applications and could potentially benefit the glass industry.

Publications arising from the thesis

Journal papers:

[1] **A. Akhtar**, H. Ruan, Review on thin film coatings for precision glass molding, *Surfaces and Interfaces*, 30 (2022) 101903.

[2] **A. Akhtar,** J. Wang, R. He, E.Y.C Wong, K. Hung, H. Ruan, Microstructural evaluation of sputtered Ru–Pt multilayer anti-stick coatings for glass molding, *Materials & Design*, 220 (2022) 110898.

[3] **A. Akhtar**, W. Wei, H. Ruan, Annealing and oxidation study of Ru-Cr coatings, under preparation.

Conference presentations:

A. Akhtar, H. Ruan, Thermal stability of Ru-based coatings for precision glass molding, *Structural Nanomaterials Gordon Research Conference*, Les Diablerets Conference Center, Switzerland, May (2022).

Acknowledgements

All praise and acclamation be to Allah Almighty, the most beneficent and merciful. First, I would like to express my sincerest gratitude to my supervisor Dr. Haihui Ruan for his constant support, valuable guidance, motivation, encouragement, and ongoing interest in seeing me through this research project. Without his kindness and help, this research would not have been possible. His consistent enthusiasm for science and positive mindset profoundly influenced me. Second, I would like to thank my senior colleague Dr. Jianbiao Wang and group member Wang Wei for their help with my research. I would also like to thank my group members Mr. Jinan Liu, Mr. Yi Yang, Mr. Yifei Wu, Mr. Jens Krarup, and all the other group members.

My deepest gratitude to The Hong Kong Polytechnic University for the funding and support received throughout the three years of my PhD studies in Hong Kong. Last but not least, I am profoundly grateful to my parents and siblings for their unending love, care, and support.

Nomenclature

AFM	Atomic force microscopy
ASG	Aluminosilicate glass
BF-TEM	Bright field transmission electron microscopy
CLS	Confined layer slip
CTE	Coefficient of thermal expansion
CVD	Chemical vapor deposition
DLC	Diamond like carbon coatings
E	Young's modulus
E-beam	Electron beam evaporation
EDX	Energy dispersive x-ray spectroscopy
FIB	Focused ion beam
FCC	Face-centered cubic
H	Hardness
HCP	Hexagonal close-packed
HRTEM	High-resolution transmission electron microscopy
HAADF	High angle annular dark field
IBD	Ion beam deposition
MS	Magnetron sputtering
PGM	Precision glass molding
PFM	Phase field modeling
PVD	Physical vapor deposition
R_a	Surface roughness
R_q	Root mean square roughness
RTA	Rapid thermal annealing
SAED	Selected area electron diffraction
SEM	Scanning electron microscopy
SPM	Scanning probe microscope
S-TEM	Scanning transmission electron microscopy
TBs	Twin boundaries

T_g	Glass transition temperature
TiC	Titanium carbide
TBs	Twin boundaries
T_g	Glass transition temperature
XPS	X-ray photoelectron spectroscopy
XRD	X-ray diffraction

Table of contents

Chapter 1: Introduction

1.1 Research background

High precision glass components with a wide variety of simple and complex geometric patterns are essential in modern world technology [1, 2]. They are extensively employed as optical equipment in fields such as laser technology [3-6], in smartphones [7, 8], space telescopes [9], sensor devices [10], medical equipment [1] and for lithography process in semiconductors technology [11-13].

As the production chains strive to promote efficiency, large-scale production of these high-precision optical components poses a major challenge when traditional grinding and polishing procedures are utilized [14]. Grinding and polishing techniques were first employed in the 1500s when microscopes [15] and telescopes [16] were developed. The laborious technique, deemed as time-consuming, demanded highly skilled craftsmanship, and production was mainly confined to lenses of simple geometrical shapes [11, 17]. Precision glass molding (PGM) technology, therefore, can speed up the production process and, at the same time, provide optical components with complex geometrical shapes and remarkably well-developed surfaces. In addition, PGM can significantly reduce the costs and production time compared to the conventional machining process.

1.1.1 Precision glass molding technology

PGM is a replicative method that enables the mass-scale production of high precision optical components without the requirement of grinding/polishing. Fig. 1.1 shows the process chain in PGM to fabricate high-quality glass components. First,

glass preforms are positioned in coated mold insertions (pressing tool-system) and thereafter heated under nitrogen gas or vacuum environment. After reaching the forming temperature (above the glass transition temperature (T_g) [18]), the glass preforms are pressed strongly for a few minutes until the glass homogenously fills the mold form. After a controlled cooling process, the pressed glass lens acquires the final product shape. Thus, a typical PGM procedure includes heating and soaking, molding, followed by initial cooling, demolding, and then finally cooling process, during which the mold experiences thermo-mechanical deformation. Consequently, the PGM process and cost efficiency are heavily dependent on the lifespan of the glass molding tools.

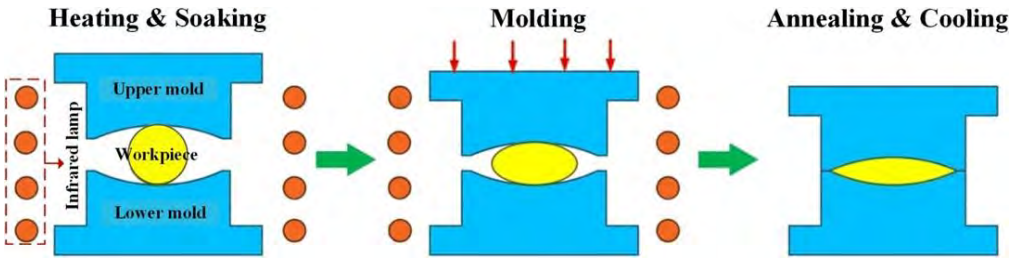

Figure 1.1 Schematic of the glass molding process [19].

Mold material selection impacts significantly on the micro/nanoscale imprinting of the molded glass. Therefore, to obtain the required replication quality, fabrication of the mold with a high degree of accuracy and efficiency is required. The primary requirements for mold materials include excellent mechanical stability with enhanced wear resistance characteristics, a low coefficient of thermal expansion (CTE), high machinability and thermal stability, high pressure workability, and ability to endure repeated heating/cooling.

For opting a mold material, the T_g of the specific glass type is the first consideration. For ultra-low-T_g glasses ($T < 400$ °C), a nickel–phosphor (Ni–P) mold

is generally employed owing to its hardness and high resistance to wear at moderate temperatures [20-22]. In addition, it offers high machinability [23, 24]; however, beyond 400 °C, crystallization leads to the deterioration of its properties [25]. Therefore, the electroless Ni–P mold is mainly appropriate for low-T_g PGM processes. For higher PGM temperatures (T > 400 °C), a substrate with high hardness and strength is required, which can withstand thermo-mechanical stresses at high temperatures, for example, silicon carbide (SiC) and tungsten carbide (WC) [26-28].

WC is employed as a mold material owing to its high hardness, thermal stability, and wear resistance [29]; however, its poor machinability owing to its inherent brittleness raises the cost because diamond grinding is the primary method for shaping the molds [17]. Additionally, the interfacial reaction of glass with binder materials (e.g., Co) and W of the WC mold can significantly reduce the service lifetime of the molds [30]. Some other mold materials, such as amorphous glass/carbon, can be used at high temperatures [31]; nonetheless, a recent study [32] revealed that the deterioration of properties induced by oxidation and thermal-mismatch difficulties in such materials could cause mold instability. Table 1.1 summarizes the different mold materials employed for PGM processes.

Table 1.1 Selection of mold materials based on the T_g of the PGM processes

Process	**Ultra-low T_g**	**Low-T_g**	**High-T_g**
Glass-T_g	< 400 °C	400 °C < T_g < 620 °C	> 620 °C
Mold material	Nickel–Phosphor	Carbides / ceramics	Carbides / ceramics
Manufacturing method	Single point turning	Diamond-grinding	Diamond-grinding
Cost	Low	High	Very high
Tooling-life	Low	Medium	Very low

Graphite is frequently employed as a mold material owing to its thermal stability and, more importantly, excellent machinability [33], which results in low manufacturing cost in production trials for compensating form errors. However, in an oxygen-containing environment, it can quickly oxidize, which affects the reliability and performance of both glass materials and mold. In addition, graphite is low-strength and brittle; thermomechanical loading and glass sticking in the molding process quickly damage the surfaces of graphite molds, leading to the adherence of graphite powders on the molded glass surfaces.

At molding temperatures, the mold can wear quickly owing to its direct contact with heated glass. This can lead to the occurrence of physical diffusion and chemical reactions on the glass–mold contact area, which results in premature mold failure and significantly affects the surface quality of the glass. Thus, the application of protective coating is critical for extending the service lifespan of the molds and increasing the surface quality of molded glass lenses [34].

1.1.2 Coatings technology

Thin film coatings, as a keystone of innovative advanced technologies, have been swiftly broadening their scope into a variety of emergent research fields and growing rapidly to fulfil the demands from both academics and industry in the past decades [35]. Thin films are layers of material that range in thickness from nanometers to several micrometers [36] and are usually employed to enhance the surface characteristics of solid materials such as reflection, absorption, hardness, corrosion, wear, and oxidation resistance [37, 38]. Thin film coatings serve the purpose of modifying the physiochemical properties and morphology of surfaces, which

establishes them as a broad subgroup of surface engineering. Fig. 1.2 displays three possibilities for using a thin-film (conductive) material, where the optical, electrical, and electrochemical properties of a depositing material can be employed for various applications.

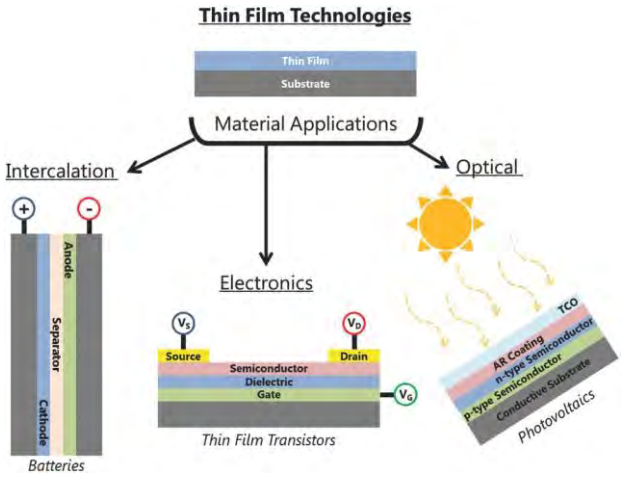

Figure 1.2 Examples of various applications utilizing thin film materials that modify optical, intercalative, and electronic properties with different designs [39].

The synthesis of protective surface coatings has attracted increasing attention owing to their exceptional physicochemical properties required in optical, magnetic, and electrical applications [40-43]. Among them, an important coating development enables the production of molded precision optics, thus shifting the optical industry from the conventional expensive and time-consuming manufacturing processes via grinding, polishing, and lapping [11, 44] to an efficient and scalable PGM technology. At glass molding temperature, the molten glass preform interacts with the mold and develops load on the cavity surface. Owing to the shear effect induced by the molten glass flow, it will cause significant damage or even failure to the molds. Furthermore, glass preform stickiness with the mold cavity is likely to occur, which will lead to an unsatisfactory demolding performance. Hence, improvement in the mold-stability

under high-temperature working conditions and demolding efficiency is vital for extending the mold lifespan and lowering PGM process costs. Surface protective coatings for PGM are critical for advancing it into a single-step process in mass production [45], which must withstand thermomechanical stresses and a corrosive thermochemical environment owing to the softened glass at molding temperatures [34]. Therefore, the structural behaviors of these coatings should exhibit sufficient strength and hardness to resist thermal shocks, adhesion, and wear at high temperatures [46]. The essential requirements for such surface coatings are (1) superior thermal stability, (2) high hardness with sufficient thermal-shock resistance, and (3) high chemical inertness with glass elements.

In PGM production, the harsh heating/cooling environment and cyclic mechanical stresses lead to fatigue and wear of the mold. Therefore, an appropriate assessment is essential while selecting the mold and coating material. The repetitive heating/cooling cycles not only induce significant variations in the thermal stresses of the mold, but also potentially trigger chemical reactions (e.g., corrosion and diffusion [47]) and sticking between the workpiece and mold. The chemical reactions are principally caused by coating adhesion to the molten glass and corrosive attack on the protective coating surface, both of which significantly shorten the mold lifetime. Together with the considerations of wear and fatigue, the CTEs of the mold and coatings should also be considered carefully. Preferably, the entire molding system consisting of the mold material, protective coating, and the working glass piece should have the identical CTE to minimize the friction at the (glass–mold) interface and maximize the accuracy of the molded glass piece. This is certainly unachievable in reality; however, attempts should be made to minimize the mismatch between CTEs.

In brief, PGM coatings can be classified into three types, namely: diamond-like carbon (DLC) coatings [48], ceramic coatings (e.g., TaN, TiAlN, CrWN) [49-51], and noble metal coatings [17, 52, 53]. Although DLC coatings have excellent anti-wear and self-lubrication performances at low temperatures, their poor thermal stability (they transform to graphite at temperatures over 600 °C) and high fabrication cost (a special facility is required) restrict the application for PGM in the glass industry [54, 55]. Ceramic coatings demonstrated better thermal stability than DLC coatings. However, at temperatures higher than 500 °C [56], oxidation of metallic elements occurs easily, resulting in glass adhesion and coating deterioration.

Based on the previous studies, noble metal coatings are considered to be the most reliable for PGM and have been widely utilized industrially owing to their superior resistance to corrosion and oxidation and high operating temperatures (typically 600–700 °C) [57]. Noble metals, for instance, platinum (Pt), iridium (Ir), and rhenium (Re) were widely studied in the past years for PGM application. Among them, the Pt–Ir coating system is the most employed because of its high oxidation and corrosion resistance and excellent anti-sticking performance. However, for high-T_g glasses (e.g., ASGs), noble metal coatings may still suffer from oxidation and sticking problems when $T > 700$ °C. Furthermore, Ir is three to four times more expensive than Pt, which discourages its use in the glass industry. In addition, the real challenge is to thermoform aluminosilicate glasses (ASGs), which are ubiquitously used as screen covers and will find further applications in virtual/augmented reality (VR/AR) glasses and smart vehicles. The molding temperatures for ASGs must be in the range of 700–800 °C, which is an unattempted temperature range for PGM coatings. Thus, new coating systems must be explored to address these challenges.

Although several coatings for PGM have been used, their failure mechanisms have been fragmentedly discussed in the literature. As the current trend of PGM migrates towards glass with high glass transition points, such as ASGs, there is a need to consolidate the existing know-how and, if possible, to improve the high-temperature performance for more stringent applications.

1.2 Research objectives

The primary aim of the thesis is to design a new coating system with high performance and stability for PGM, particularly for high-T_g glasses. The main objectives are listed below.

1. To design and develop noble-metal-based economical protective coatings for glass molding dies to enhance their lifetime and achieve high anti-stickiness.
2. To investigate the microstructural evolution of the developed coatings at glass molding temperatures.
3. To develop cost-effective functional coatings for mass scale production.

1.3 Thesis outline

This thesis presents the development of new, cost-effective, and highly stable coating systems for PGM applications. This thesis is organized into six chapters:

Chapter 1 provides a brief overview of the precision glass molding process, including mold materials and coating technology. It also addresses the unresolved challenges and defines the research objectives of this study.

Chapter 2 systematically reviews the state of the art of PGM coatings with a focus on their deposition techniques, anti-sticking, microstructural, and mechanical

properties, and their degradation mechanisms in glass molding cycles. With these findings, a viewpoint for improving the reliability of PGM coatings is proposed.

Chapter 3 describes the materials and methods employed in the deposition of thin film coatings on substrate materials and the characterization techniques used to evaluate the sputtered coatings.

Chapter 4 demonstrates the performance of multilayer Ru–Pt coatings with Ti as the interlayer deposited on the graphite substrate for PGM applications. After high temperature annealing (750 °C) for varied time durations, glass adhesion was not observed, suggesting the high chemical inertness of the Ru–Pt multilayer coatings at the glass molding temperature (for high-T_g glasses). The microstructure, thermal stability in terms of surface characteristics, and mechanical properties were further characterized. The high-resolution transmission electron microscopy (HRTEM) study showed the preservation of the layered structure after long time annealing at 750 °C. The performance of multilayer coatings was also validated using an industrial testing system.

Chapter 5 investigates the annealing and oxidation studies of varied Ru–Cr coatings for PGM. As demonstrated by experimental and simulation results, outward diffusion of Cr during annealing phenomena lead to the formation of oxide scale on the top of the coating, which is regarded as stable oxide layer,. With increasing thickness of Ru in Ru–Cr coatings, a reduction in the outward diffusion of Cr was observed.

Chapter 6 summarizes the main research findings and future work recommendations.

Chapter 2: Literature review

2.1 Deposition methods

Thin films exhibit distinctive performances compared with bulk materials because the majority of the deposition processes are nonequilibrium in nature; thus, a thin film formation can be outside the permissible region of the corresponding (equilibrium) phase diagram [58-60]. Deposition techniques practically determine the properties of a thin film and can be used to modify the properties of the bulk material. These techniques require proper consideration according to the area of utilization because they do not result in identical properties, such as surface morphology, microstructure, hardness, and corrosion resistance [61]. In general, thin-film deposition phenomena are classified into two main groups: physical vapor deposition (PVD) and chemical vapor deposition (CVD) (Fig. 2.1). For PGM, the coatings developed based on them in the open literature have been summarized in Table 2.1

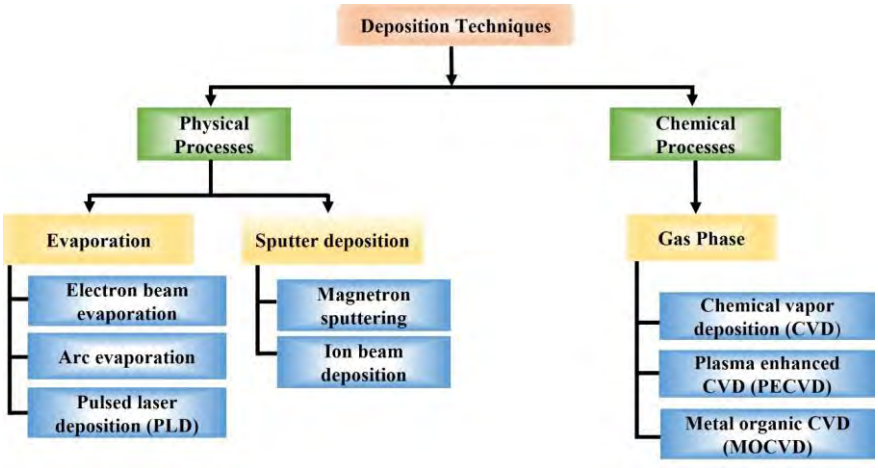

Figure 2.1 Classification of deposition techniques.

2.1.1 Physical vapor deposition

PVD encompasses a broad range of vapor-phase technologies, where atoms or molecules are physically ejected from a material and subsequently condensed and nucleated onto a substrate [62]. Generally, PVD methods are employed in film deposition with thicknesses ranging from several nanometers to several micrometers. Their applications include graded composition deposits, multilayer coatings, free-standing structures, and dense deposits. Owing to their versatile features, sustainable and environment-friendly PVD methods have received increasing interest in modern times [63]. It is employed primarily to improve the tribological, optical, and mechanical properties of a substrate material [64, 65]. The main PVD processes are sputtering, electron beam evaporation, and ion beam deposition.

2.1.1.1 Sputtering

Sputtering is a vacuum coating technique in which cathodic targets (source materials) are bombarded by energetic ions of inert gases such as argon (Ar) or helium (He). The development of cations is caused by the plasma that ignites between the (cathode) targets and (anode) substrates. The positive ions (cations) driven in an electric-field hit the surface of a target [66]; the transfer of kinetic energy to atoms of the target establishes a thin film onto a substrate surface (Fig. 2.2). This process has several advantages, such as high purity, remarkable adhesion, high deposition rates, and simplicity of depositing either metallic or ceramic coatings. Sputtering also facilitates the formation of materials with a high melting point. Reactive gases, such as oxygen or nitrogen, can be added to form metal oxides, nitrides, or other compound films. Generally, the sputtering process has common types: direct current (DC) and

radio frequency (RF) sputtering. In a DC sputtering system, the glow discharge is maintained by a DC current between the metallic electrodes. However, in RF sputtering, an AC current is applied to neutralize the charge build-up in an insulating target material.

Table 2.1 lists the PGM coatings reported in the literature. It can be seen that sputtering is the most extensively applied in the development of PGM coatings owing to the process simplicity and flexibility to offer a broad range of materials deposition. For example, Wu et al.[67] utilized magnetron sputtering to develop Ir-based anti-stick coatings on WC substrates. The preparations of thin films (rhenium, chromium, and iridium) were accomplished by a multi-target sputtering system. The obtained results have demonstrated that the surface roughness and morphology remained unchanged before and after heat treatment at 500 ºC for 4 hours indicating an excellent thermal stability. CrWN coatings deposited by magnetron sputtering on cemented carbide exhibited increase in nano-hardness up to one thousand thermal cycles at 600 °C [68]. PtIr coating with interlayer material (Cr, Ni) was deposited on WC substrates by magnetron sputtering [69], which has been the most popularly used in the industry.

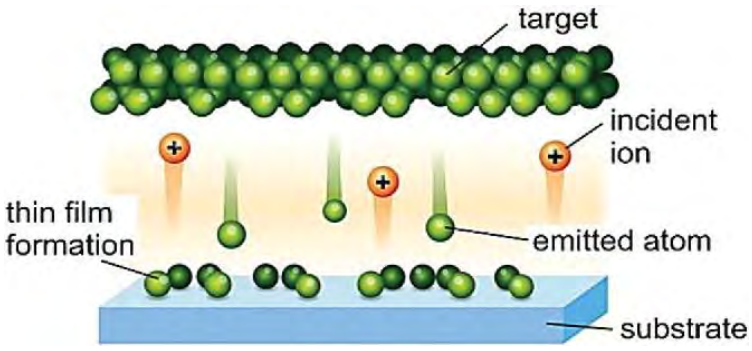

Figure 2.2 Illustration of sputtering procedure on an atomic scale [70].

2.1.1.2 Electron beam evaporation

An intensive electron-beam (e-beam), produced from a filament and driven by both magnetic and electric fields, can also vaporize a target material in a vacuum (Fig. 2.3). Even materials with high melting points (e.g., metal oxides) can be effectively vaporized with e-beams [71]. E-beam evaporation is a rapid process with deposition speeds of several micrometers per second, although the quality and adhesion of the developed film on a substrate could suffer owing to the low-energy of the vaporized particles. Therefore, more advanced evaporation methods utilize excess plasma. The vaporized particles passing through the plasma region ionize, consequently, they can be accelerated to produce a film [72] denser than the columnar grains resulting from the conventional e-beam deposition because high-energy ionized particles can disrupt columnar growth. Thin films developed by this technique are of high quality and purity [73]. Recently, plasma driven e-beam evaporation is referred as an effective method in the manufacturing of anti-reflected coatings on the lenses for optical-spectacles [74]. Wen et al. [75] adopted the e-beam evaporation technique to deposit Ni/Ru multilayers to evaluate the thermal stability of the developed coatings at temperatures below 600 ºC. However, substantial reduction in hardness was observed at 600 ºC owing to the break-down of the periodic structure in deposited layers.

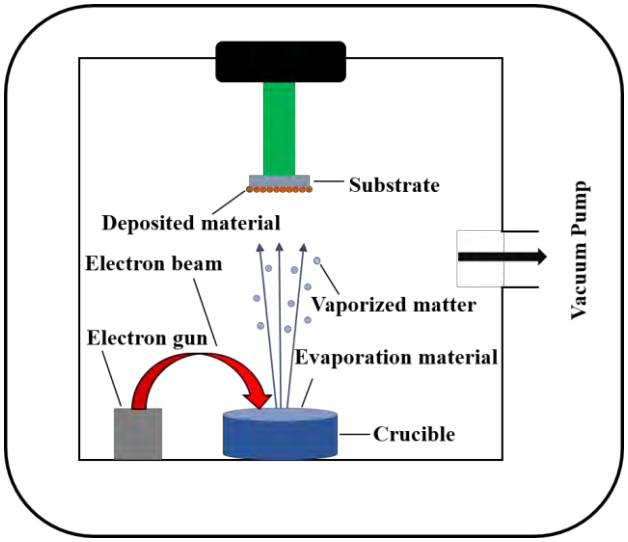

Figure 2.3 Schematic of e-beam evaporation [76].

2.1.1.3 Ion beam deposition

Similar to e-beam evaporation, energetic ions ejected from an ion source can also sputter material off a target, which, after plume formation, is deposited onto the substrate surface. A schematic of the ion beam deposition (IBD) is shown in Fig. 2.4(a). Technically, the significance of IBD is the controllability of ionic energies and the impact of ion occurrence on a developing surface. An additional ion gun can be utilized to assist deposition through bombardment with a developing film, called ion-beam assisted deposition (IBAD). Dual ionic beams facilitate stoichiometry control in thin films [77]. In addition, the bombardment of ions eliminates the columnar microstructure (which is commonly observed in low-temperature PVD) to establish very dense and adherent films. Lin et al. [51] obtained CrWN coatings on the WC substrates by IBAD method with Cr as adhesive interlayer between coating and the substrate. The experimental results exhibited that the increase in tungsten composition from 4.4 to 16.7 at. % resulted in improved hardness and lower surface roughness at 600 ºC. TiAlN coatings were prepared by IBAD on silica substrates utilizing TiAl

target. The impact of residual stress on the wear behavior at 650 °C were studied [78]. It was found that the initial stress state played a crucial role in the wear behavior of the coatings. Coatings with initial tensile stresses experienced failure at low loads. In contrast, excellent resistance to micro-cracking was observed if initial compressive stresses were developed in the TiAlN coating.

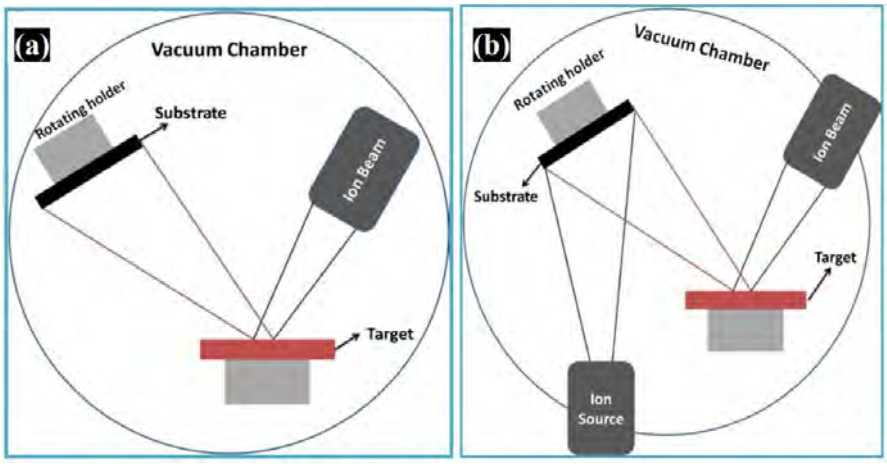

Figure 2.4 Schematic of (a) IBD and (b) IBAD [79].

2.1.2 Chemical vapor deposition

CVD is a broad term used for the process of preparing thin films through a series of chemical reactions. In CVD, material synthesis occurs when target constituents in the vaporized state react near the surface or into the substrate surface, resulting in film growth [80]. Various factors of this process are responsible for film quality, such as temperature, pressure and flow rate [81, 82]. The main distinctive features of CVD are its versatility in forming either simple or complex compounds with comparative ease in terms of frequently low temperature, outstanding throwing power, uniform coating thickness, high growth rate, and easiness of epitaxial growth. CVD can be used to deposit materials that are difficult to vaporize, and it is more adaptable to depositing on substrates of complex shapes than other deposition techniques [62, 83].

Major CVD techniques include plasma-enhanced atomic layer deposition (PEALD), PECVD, and metal-organic CVD.

He et al. [84] established carbide bonded graphene coating on silicon molds by CVD method to avoid silicon adhesion to glass at a molding temperature of 560 °C. In this CVD coating, benzene was utilized as a carbon source material to produce a covalent bonded graphene-like network at 950 ºC under inert gas atmosphere. Zhang et al.[85] developed α-Al_2O_3 coatings on WC substrates by CVD technique in order to achieve better anti-sticking property for barium crown optical glass (D-ZK3) at 600 °C. Before the deposition of ceramic (Al_2O_3) coating, an interlayer containing layered structure of TiN, Ti (C, N), and Ti (C, O) was deposited at temperature of 950°C, 850°C and 1000 °C, respectively, to enhance adhesion between both the protective coating and substrate. Kim et al. [33] deposited SiC coatings on graphite substrate by CVD in a furnace at a temperature range of 800-1200 ºC. SiC coating was used to improve oxidation resistance in order to prevent the fast oxidation of graphite molds at elevated temperatures. It should be noted that CVD requires a fine control of chemical processes, i.e., for developing a coating, the gaseous reactants and by-products must be well known and pressure and temperature must be accurately determined based on the thermodynamical calculation of the reactions [86, 87].

Table 2.1 Deposition of coatings for PGM applications

Reference (Year)	Coating material / Interlayer	Substrate	Deposition technique[a]	Annealing temperature (°C)	Glass type	Major findings
Wu et al. [67] (2003)	PtIr, IrRe, IrReCrN /-	WC	RF-M.S.	500 °C	-	Thermal stability of the Ir-based coatings was observed at 500 °C
Lin et al. [51] (2006)	CrN, CrWN / -	Si, WC	IBAD	750 °C	-	Cr_2O_3 formation caused the increase in surface roughness of coatings and higher content of W in CrWN coatings demonstrated improvement in hardness
Chen et al. [88] (2006)	MoRu / Ni	WC	DC-M.S.	600 °C	-	Adequate thermal stability under 600 °C was observed w.r.t hardness and surface roughness
Kang et al. [40] (2007)	MoRu / Ni	WC	DC-M.S.	550 °C	-	An increase in surface roughness of the coatings was observed with an increase in interlayer (Ni) thickness and a decrease in hardness with a decrease

						in Mo content at 550 °C
Wen et al. [75] (2008)	NiRu /-	Si wafer	E.B.E.	600 °C	-	Substantial reduction in hardness at 600 °C was observed owing to the breakdown of the periodical multilayer structure
Chen et al. [89] (2009)	MoRu / Cr, Ti(O)	WC	RF-M.S.	600 °C	-	Better oxidation resistance and higher hardness with the increase in Ru content were observed at 600 °C
Chien et al. [90] (2010)	PtIr / TaN	WC/Co	M.S.	700 °C	L-BAL42	Restriction of WC/Co diffusion with the TaN interlayer was observed
Bobzin et al. [14] (2010)	PtIr / Ni, Cr	WC	PVD	-	-	Evaluation of the protective coatings via a nanoimpact test revealed the better adhesion property with Cr interlayer than Ni interlayer
Sakurai et al. [91] (2010)	PtZrNi / -	WC	RF-M.S.	450 °C	BK7	An increase in Zr content in PtZrNi coatings deteriorated the anti-sticking performance

Fischbach et al. [50] (2010)	PtIr, TiAlN / Ni	WC, Si	DC-M.S.	550 °C	P-SK57	Superior anti-sticking performance was observed with PtIr coating than TiAlN coating in actual PGM condition
Masuda et al. [92] (2011)	PtIr, IrRe / Ni	Steel	RF-M.S.	570 °C	-	Faster Ni diffusion in PtIr coating was observed than in IrRe coating after heat treatment at the same temperatures
Chen et al. [49] (2011)	TaN / -	WC-Co	DC-M.S.	500–800 °C	-	Diffusion of oxygen occurred through the columnar structure of the annealed TaN_x coatings above 500 °C, making the TaN-based coatings unapplicable for PGM
Tseng et al. [93] (2011)	PtIr, NiIr / Cr	WC	ISAMSS	700 °C	L-LAH83, N-KZFS5, K-LaK8	Less oxidation resistance with NiIr coating than PtIr coating at 700 °C
Klocke et al. [69] (2011)	PtIr / Ni, Cr	WC	PVD	-	-	Improvement in adhesion and effective strength with either Ni or Cr interlayer (Cr interlayer is

						relatively more effective)
Bobzin et al. [94] (2012)	PtIr / Cr	WC/Co	MSIP-PVD	650 °C	P-LASF47, N-FK5	Diffusion of Cr interlayer was observed into the PtIr coating, increased glass defects at the glass–coating contact zone with the increase in interlayer thickness
Lin et al. [56] (2013)	CrWN / -	Si, WC	M.S.	500 °C	K-PG325	CrWN coatings demonstrated improved anti-sticking with glass at 400 °C
Chao et al. [44] (2013)	PtIr / Ta	WC/Co	M.S.	596–607 °C	N-PK, N-FK, P-SK, L-NB, N-PS	PtIr coating displayed enhanced anti-sticking performance for different optical glasses.
Liu et al. [53] (2013)	ReIr / -	Si	M.S.	600 °C	-	The annealed ReIr coating with increased Ir content exhibited better thermal stability at 600 °C
Bobzin et al. [95] (2014)	PtIr / Ni, Cr	WC/Co	M.S.	590–645 °C	L-BAL42, P-LASF47, N-FK5	Severer interfacial reaction between coating and glass with an increase in Co content in the substrate

Chen et al. [96] (2014)	TaSiN / -	Si	DC-M.S.	600 °C	-	The preferential oxidation of Si occurred in TaSiN coatings. During 600 °C annealing, the inward diffusion of oxygen was restricted by the development of Si oxide scales.
Chen et al. [97] (2014)	TaN, CrTaN, TaSiN, CrTaSiN / -	Si wafer	M.S.	600 °C	BK7	Thermal stability of as-deposited Ta-nitride coatings (TaN, CrTaN, TaSiN, CrTaSiN) after cyclic annealing were evaluated. CrTaSiN demonstrated the best mechanical properties with the lowest roughness, making it a suitable candidate for glass molding.
Chen et al.[98] (2014)	CrTaSiN / -	Si, WC	M.S.	600 °C	SiO_2-ZnO-La_2O_3 and SiO_2-B_2O_3-BaO glasses	Increased nanohardness was observed for CrTaSiN coatings in comparison with Cr-free coatings and outward diffusion of glass elements (Ca, Na, Zn) during thermal

						cycling resulted in the reduction of coatings (CrTaSiN) surface quality.
Zhu et al. (2015)	ReIr / Ta	WC/Co	RF-M.S.	631 °C	D-ZK3	The Re/Ir multilayer exhibited better anti-stick performance than Re and Ir monolayers for barium crown optical glass.
Chen et al.[68] (2015)	CrWN / Cr	Si, WC	DC-M.S.	600 °C	SiO_2-B_2O_3-BaO-based glass	Higher W content resulted in the reduction of nano hardness at 600 °C, owing to WO_3 formation.
Klocke et al.[30] (2016)	PtIr / Ni	WC	M.S.	640 °C	B270	Selective oxidation of Ni was occurred owing to the grain boundary diffusion.
Peng et al.[99] (2017)	PtIr / Cr, Ni	WC	M.S.	630 °C	-	Outward diffusion phenomena were observed for Ni and Cr interlayer owing to grain boundary segregation in which Ni diffusion is faster than that of Cr.
Chang et al.[100] (2018)	ZrSiN / Ti	Si, WC	DC-M.S.	600 °C	SiO_2-B_2O_3-BaO	ZrSiN coatings with higher Si contents (>30 at. %) exhibited an amorphous

					based glass	phase with increased hardness, which was ascribed to the variation in the bonding characteristics.
Lee et al.[101] (2018)	AlCrN / -	WC	M.S.	800–900 °C	-	The atomic ratio of Al/Cr was nonuniform, causing a detrimental effect on the oxidation resistance at higher temperatures.
Wei et al. [102] (2019)	ReIr / Ta	WC	M.S.	631 °C	D-ZK3	Enhancement in mechanical performances and restriction of atomic diffusion were observed with a Re/Ir multilayer compared with Re and Ir monolayers.
Friedrichs et al. [57] (2020)	PtIr / Cr	WC	DC-M.S.	640 °C	B270	PtIr coating surface deteriorates (increasing defects) with increased molding cycles.
Huang et al. [103] (2020)	CrWN / -	Si, WC	PEMS	650 °C	BK7	Severe oxidation of the annealed coatings occurred in air and the higher W content increased the surface

						roughness and coating thickness.
Chen et al. [104] (2020)	CrSiN, TaSiN, ZrSiN / Cr, Ti	WC	DC-M.S.	600 °C	SiO_2-B_2O_3-BaO-based glass	ZrSiN coatings exhibited better anti-sticking in glass molding than CrSiN and TiSiN coatings.
Zhang et al. [85] (2020)	α-Al_2O_3 / TiN	WC	CVD	280 °C, 540 °C	D-ZK3, IRG206	α-Al_2O_3 multilayer coatings developed using CVD exhibited better anti-sticking properties with D-ZK3 glass and chalcogenide glass compared with DLC coatings
Li et al. [105] (2020)	CrWN / -	WC	PEMS	650 °C	BK7	Increased W content resulted in the enhancement of Young's modulus and nanohardness and a decrease in the surface roughness.
Guo et al. [106] (2020)	CrWN / -	Si, WC	PEMS	650 °C	-	The as-deposited coatings exhibited the nonuniform distribution of the solid-solution matrix, whereas annealing caused homogenizatio

	n, resulting in considerable age-hardening.

[a] RF-M.S.: radio frequency magnetron sputtering; DC-M.S.: direct current magnetron sputtering; E.B.E: Electron beam evaporation; PEALD: Plasma enhanced atomic layer deposition; PVD: Physical vapor deposition; M.S.: Magnetron sputtering; ISAMSS: Ion source assisted magnetron sputtering system; MSIP-PVD: magnetron sputter ion plating physical vapor deposition; PEMS: plasma-enhanced magnetron sputtering; IBAD: ion beam assisted deposition; CVD: chemical vapor deposition

2.2 Anti-sticking and durability

2.2.1 Overview of coating materials

Among the various coatings developed for PGM, as identified in several papers [67, 107], noble metal coatings are generally employed in industries because of their superior oxidation and corrosion resistance and better reliability than other coatings. Noble metals are nonreactive with cations, anions, and network atoms in glasses in the temperature range for PGM (typically 600 – 700 °C) [67]. Another advantage over other coatings is that the coating process for noble metals is simple, as an industrial sputtering facility can serve this purpose. Klocke et al. [108] compared nitride and noble metal coatings on tungsten carbide (WC) substrates and observed that noble metal coatings exhibited a significantly better resistance to oxidation and anti-sticking properties than nitride coatings at or below 700 °C. Another study by Tseng et al. [93] demonstrated that PtIr coatings have better mechanical properties than NiIr coatings on WC substrates. Fischbach et al. [50] compared PtIr and TiAlN coatings on WC and Si substates in industrial glass molding atmospheres and observed that PtIr coatings exhibited significantly better anti-sticking properties than TiAlN coatings.

Table 2.1 shows the different coating types, substrate materials, interlayer materials, and deposition techniques that were employed in previous PGM

applications. It is evident that the PtIr coating is the most widely adopted among the noble metal coatings, owing to its chemical inertness and anti-sticking property. Additionally, WC is extensively employed as a substrate material owing to its remarkable wear resistance and thermal stability, and nickel (Ni) or chromium (Cr) interlayers are the most applied to promote adhesion between the noble metal coatings and substrates, and PVD, in particular magnetron sputtering, is extensively applied to develop coatings. However, considering the huge cost of noble metallic materials and the further elevated PGM temperatures, efforts are still required to develop ceramic coatings or a combination of ceramic and metallic coatings. In the following section, we review the existing coatings and their performance in PGM applications.

2.2.2 Noble metal coatings

2.2.2.1 Anti-sticking property

In a PGM process, glass–mold sticking at molding temperatures is a critical problem that results in limitations in the quality of molded glass products and the lifetime of molds [109]. In addition, molding tools undergo cyclic thermomechanical and chemical loads. Therefore, coatings are required to protect and improve the service lifespans of molding tools. Friedrichs et al. [57] investigated the glass adhesion properties of four different PtIr protective coatings on cemented WC substrates. Energy-dispersive X-ray spectroscopy (EDX or EDS) data obtained from scanning electron microscopy (SEM) of four different PtIr-coated samples with and without the Cr interlayer after multiple molding cycles are shown in Fig. 2.5. When there was no interlayer, several small regions of damage appeared on the coating surface. The corresponding EDX data revealed that adhesion occurred as a significant

level of glass elements was identified on the surface. They observed that the degradation of the molding tool was due to the outward diffusion of W atoms. With the employment of a 20 nm Cr interlayer, glass adhesion was further reduced, and the Cr oxide-scale formed on the coating surface owing to the outward diffusion of Cr resulting in a roughness change and some glass adhesion. Comparing the interlayers of 20- and 5-nm Cr for 600-nm PtIr coatings, they observed that the thinner interlayer resulted in larger surface defects caused by glass adhesion. Tungsten (W) was identified in the adhesion areas, implying that before the deterioration of the Cr layer, substrate degradation occurred because of the outward diffusion and accumulation of W on the surface. Such a coating failure mechanism was further corroborated based on the result of thinner coatings, i.e., 300-nm PtIr and 20-nm Cr interlayer, which were rapidly damaged and spalled.

The study of Friedrichs et al. indicted the following challenges with the PtIr/Cr/WC system:

(i) Glass adhesion is primarily due to the diffusion of W and Cr towards the coating surface.

(ii) Selective oxidation of Cr after Cr atoms reaches the surface causes an increase in surface roughness, which is the initial stage of degradation. This oxide-scale reduces the performance of anti-stickiness, resulting in glass adhesion fragments on the top surface. The internal consumption of Cr in the interlayer causes Kirkendall voids [99], which impairs PtIr coating adhesion.

(iii) In addition to the Cr oxide scale, glass adhesion also occurs in areas containing a large amount of W atoms emanating from the substrate. The existence of W resulted in more severe glass adhesion than the Cr oxide scale.

(iv) The service lifespans of coated WC-based molding tools, indicated by the extent of loss of anti-sticking performance, are governed mainly by the outward transportation of W and secondarily by the Cr-diffusion.

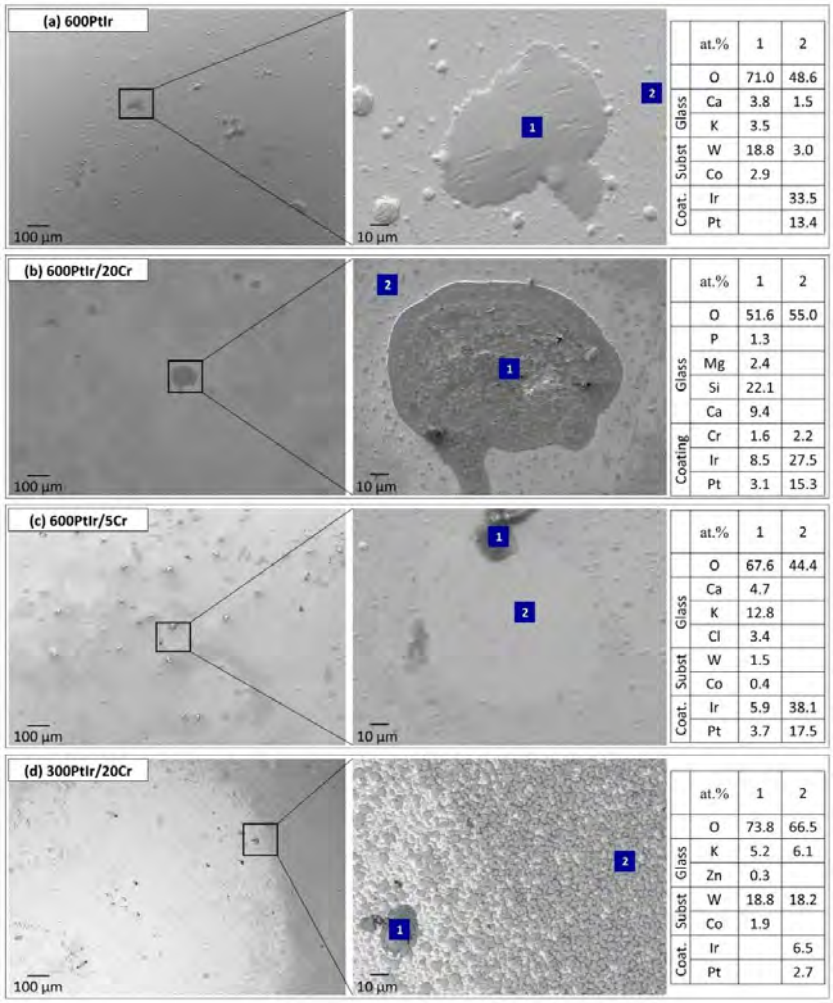

	at.%	1	2
Glass	O	71.0	48.6
	Ca	3.8	1.5
	K	3.5	
Subst	W	18.8	3.0
	Co	2.9	
Coat.	Ir		33.5
	Pt		13.4

	at.%	1	2
Glass	O	51.6	55.0
	P	1.3	
	Mg	2.4	
	Si	22.1	
	Ca	9.4	
Coating	Cr	1.6	2.2
	Ir	8.5	27.5
	Pt	3.1	15.3

	at.%	1	2
Glass	O	67.6	44.4
	Ca	4.7	
	K	12.8	
	Cl	3.4	
Subst	W	1.5	
	Co	0.4	
Coat.	Ir	5.9	38.1
	Pt	3.7	17.5

	at.%	1	2
Glass	O	73.8	66.5
	K	5.2	6.1
	Zn	0.3	
Subst	W	18.8	18.2
	Co	1.9	
Coat.	Ir		6.5
	Pt		2.7

Figure 2.5 SEM surface analysis and EDX data of four different PtIr coating systems [57].

Wei et al. [102] examined the anti-sticking property by applying the sessile drop method (wetting test). In this test, D-ZK3 glass balls were positioned on the coated

substrates in a vacuum. The temperature was increased to 631 °C, 120 °C above the T_g, for one hour. Fig. 2.6 shows the wetting angle of the glass ball on the substrate with different coatings. They observed that at 631 °C, a slight adhesion occurred between the glass ball and both the Ir and Re coatings. Surprisingly, the Re/Ir multilayer coating resulted in minimum adhesion; the glass sample remained approximately spherical with a contact angle of 168.1°, significantly larger than those resulting from Re and Ir monolayers and WC (without coating). After the wetting test on the monolayer-coated samples, the surface of the glass ball became slightly opaque. High temperatures promoted inter-diffusion (or chemical reactions) between glass/coating. Moreover, the diffusion of active substrate elements towards the surface initiated the reaction, resulting in a decrease in the wetting angle [110]. Conversely, the adherence of the optical glass ball with the substrate was reduced considerably after the multilayer Re and Ir coatings were developed, by which the glass ball remained fully transparent and no apparent sticking occurred after the wetting tests at 631 °C. Thus, a Re/Ir multilayer coating was suggested in [102]. Furthermore, this result indicated that multilayer coatings may be superior to monolayer coatings in terms of anti-sticking performance. For monolayers, diffusion is facilitated by grain boundaries [111, 112], whereas in multilayers [109, 113, 114], the interfaces of disparate elements enhance the resistance to diffusion, and therefore, better suppress the outward migration of substrate elements to react with the glass. Additionally, Refs. [115, 116] demonstrated that the ordered nanostructure resulted in higher resistance to the penetration of cations in glass (e.g., Ca, Ba) into the protective coatings, thereby facilitating the anti-sticking performance.

The main purpose of the protective coatings is to extend the mold lifespan by establishing a chemical impediment to prevent the most frequent failure, i.e., glass sticking. The above-mentioned studies indicated that at high temperatures in glass molding, the diffusion of active elements in the interlayer and substrate via the grain boundaries of the protective coatings towards the surface is the most common phenomenon that results in glass sticking. Therefore, the multilayer structure of noble metal coatings may bring about a notable improvement in anti-sticking performance, which is attributed to the impediment of atomic diffusion caused by the addition of interfaces.

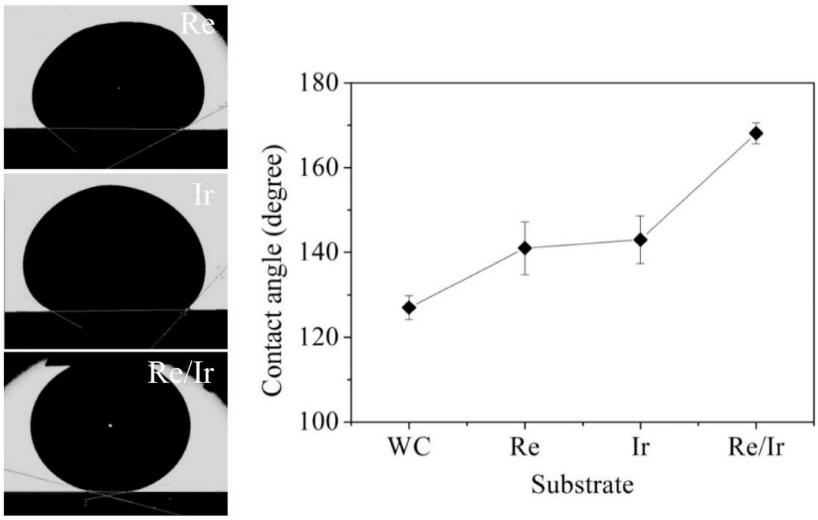

Figure 2.6 Wetting angle of different coatings at high temperatures [102].

2.2.2.2 Degradation mechanisms

PGM tools with protective coatings must undergo several hundred to thousand pressing cycles to justify their economic benefits over traditional material removal processes. This can result in changes in the surface topology, inertness, and even mechanical failure (e.g., spallation). Therefore, knowledge about the mechanism of coating failure is vital. Zirong et al. [99] examined the degradation mechanism of

$Pt_{0.3}Ir_{0.7}$ coatings on WC substrates with Cr as the adhesive interlayer at 630 °C. The degradation evolution based on the experimental observations is depicted in Fig. 2.7. The outward (external) movement of Cr-atoms associated segregation along the grain boundaries of the protective coating was suggested as the leading degradation mechanism. From a thermodynamic perspective, diffusion is driven by chemical potential gradients and activities across the interfaces of disparate materials. However, grain boundaries provide fast channels, along which diffusion is a few orders of magnitude quicker compared within a grain [117]. Therefore, at a higher temperature of 630 °C and in a short period [118, 119], the outward transport of interlayer atoms occurs primarily through grain boundary diffusion, which forms oxide scales on the coating surface.

The development of surface oxides is strongly influenced by the interior material transport. First, the decoration of solutes in PtIr grain boundaries is directed by Gibbs isotherm, that is, the reduction in interfacial energy owing to the decoration of solutes. This results in a diffusion flux into the grain boundaries. When diffusive species arrive at the surface of the film, oxidation processes occur to eliminate the solutes, in particular, those from the decorated area at the grain boundaries owing to their trapping in the oxide scale. This impact results in the decrease in the solute chemical potential in the grain boundaries; thus, a chemical potential gradient towards the surface is established, which promotes further outward diffusion [120-125]. If the oxide scale is sufficiently dense to stop oxidation, the outward transport of the diffusive species can be slowed down [126].

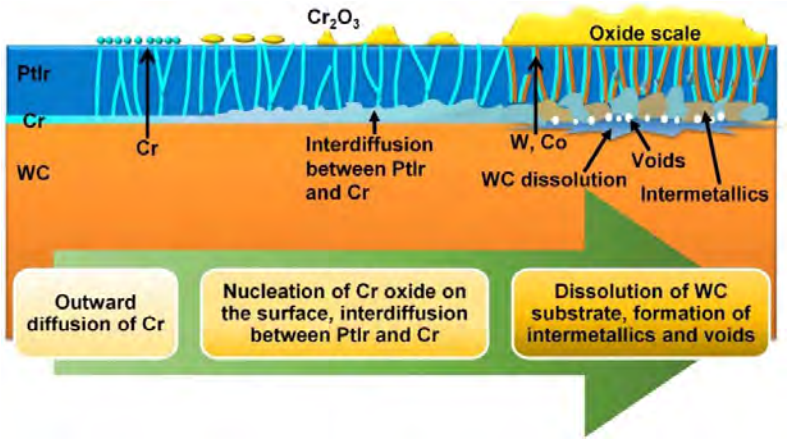

Figure 2.7 Illustration of degradation evolution mechanism of PtIr/Cr/WC at 630 °C [99].

Fig. 2.8 shows a three-dimensional element distribution of a heat-treated (at 630 °C) PtIr/Cr/WC system obtained using atom probe tomography. The appearance of Cr enrichment at both the grain boundaries of the protective coating and the interfacial areas are shown in Fig. 2.8(b) and 2.8(c), respectively. The diffusion of Cr results in the formation of intermetallic phases, which are initially Cr-rich compounds with a stoichiometry of $(Pt, Ir)_3Cr_2$ formed at the PtIr/Cr interfacial area. With continuous thermal exposure, the continuous consumption of the Cr interlayer is caused by the nuclei growth of such intermetallic compounds and oxide scale formation on the surface. When the Cr interlayer is fully consumed, the activity of Cr decreases, and the $(Pt,Ir)_3Cr_2$ formation stops. Subsequently, Cr atoms diffuse out from the intermetallic phase, resulting in the shrinkage of the $(Pt,Ir)_3Cr_2$ phase, which may change to the Cr-lean phase of $(Pt,Ir)_3Cr$ or completely vanishes. This phenomenon of second phase formation and depletion induced by supply limitation has also been observed in several previous studies [127-133].

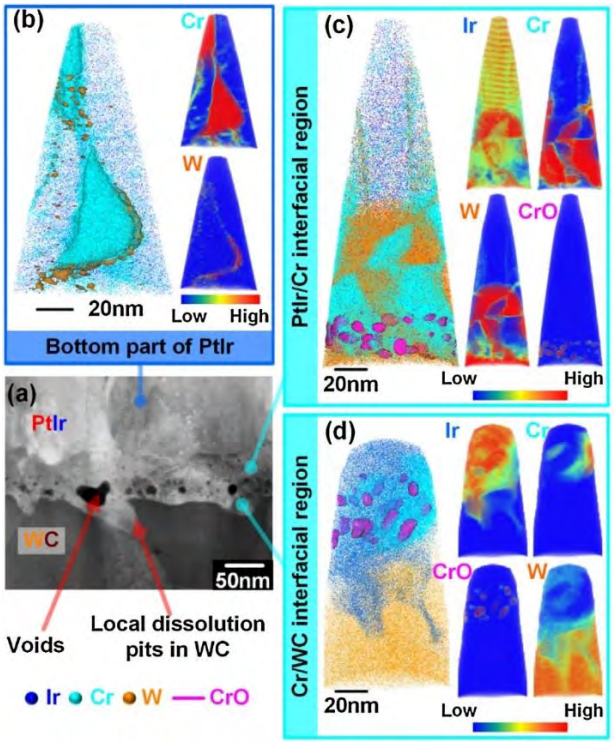

Figure 2.8 Typical characterization results acquired from the interfacial area of PtIr/Cr/WC specimen after heat-treatment at 630 °C: (a) STEM image and 3D atomic mappings of (b) PtIr layer bottom part, (c) PtIr/Cr interfacial area, and (d) Cr/WC interfacial area [99].

At the later stage of coating degradation, the involvement of the WC substrate in the diffusion process causes the development of W-enriched intermetallic compounds. Additionally, at the interfacial area, these intermetallic compounds form numerous voids, known as the Kirkendall effect [134], in which imbalance mass transportation as a consequence of the difference in diffusion rates creates free volumes. During the outward diffusion of Cr-dominant species, vacancies drift in the opposite direction. These additional vacancies may condense into voids [135, 136], which play a crucial role in the commencement of WC degradation.

Klocke et al. [30] investigated the degradation of a PtIr coating with Ni as an adhesive interlayer. The PtIr-coated samples covered with B270 glass were heated at 640 °C for several heating cycles in a vacuum or nitrogen environment. The resulting

coatings and glass are shown in Fig. 9(a). The marked regions in Fig. 2.9(a) were subjected to X-ray photoelectron spectroscopy (XPS) analysis, and the results are shown in Fig. 2.9(b). The study observed that Ni oxides formed only on the surface. At a depth of 20 nm, only metallic Ni was observed in the PtIr film. This demonstrated that external and selective oxidation occurred after the outward diffusion of Ni. Additionally, W and, to a smaller extent, cobalt (Co) oxides formed on the surface, indicating the oxidation of these species. The diffusion of nickel likely occurred through the grain boundary diffusion mechanism [92]. After sputtering to remove the 20 nm layer, nickel oxide was eliminated, and only metallic Ni was identified. An XPS analysis at a depth of 20 nm also demonstrated a considerable reduction in Co and W concentrations, which were significantly smaller than the Ni concentration. Therefore, it was hypothesized that the existence of Co and W on the surface is not the result of diffusion through the layers of PtIr and Ni. Instead, open craters were identified on the coating surface, where large fractions of W and Co were detected. The dimensions of the craters were 1–30 μm, suggesting that the PtIr/Ni layer was deformed and fractured by the media resulting from underneath, possibly because of the invasion of oxygen and the formation of W and Co oxides. Additionally, a high content of carbon was also identified using XPS analysis (zone 2); however, owing to the chemical inertness of carbon, it was not involved in glass adhesion with the surface [54, 137].

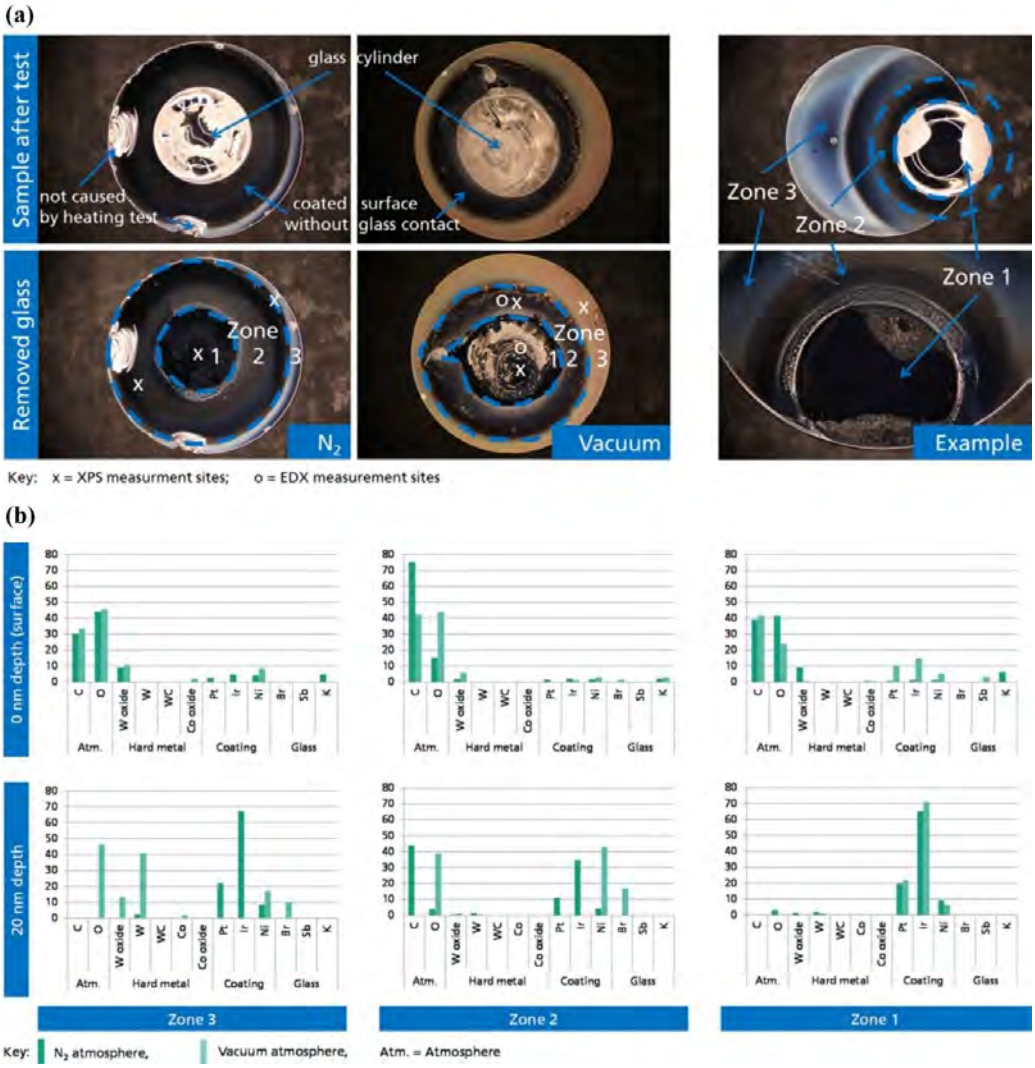

Figure 2.9 Evaluation of PtIr/Ni/WC: (a) optical images of specimens after heating tests with glass covers, and (b) XPS analysis of coating surfaces and subsurface [30].

Liu et al. [138] examined the chemical inertness of IrRe protective coatings developed on silicon (Si) substrates with B_2O_3-ZnO-L_2O_3 glasses in the temperature range of 270–600 °C. The results revealed that the invasion of Zn from the glass reduced the coating performance. Additionally, the formation of Zn compounds on the coating surface resulted in a significant increase in the surface roughness. In another study [92], IrRe and PtIr coatings were employed on Ni-P molds, and the results indicated that the diffusion of Ni was promoted in the grain boundaries of Ni and Ni_3P intermetallic in the plating structure towards the coating surface. However, Ni

diffusion was suppressed in the IrRe coating owing to the smaller diffusion coefficient of Ni in the IrRe alloy than in the PtIr alloy. MoRu coatings deposited on WC substrates have exhibited significant thermal stability in terms of surface characteristics and phase evolution, including hardness and roughness, after annealing at 600 °C [88]. Chen et al.[139] studied the annealing effect (at 600 °C) of TaRu and MoRu coatings in an oxygen-containing environment. They observed that the preferential internal oxidation phenomena occurred for tantalum (Ta) and molybdenum (Mo) in the coatings; however, the ruthenium (Ru) element remained in its metallic state. Owing to internal oxidation, the resulting laminated oxide structures converted TaRu and MoRu coatings into alternating layers of (Ta_2O_5, Ru) and (MoO_2, Ru), respectively.

Above studies have shown that the degradation of coated molds is primarily influenced by the interfacial areas of interlayers with protective (noble metal) coatings and with substrate. Owing to thermal instability, outward movement and segregation of the interlayer material along the GBs of the protective coatings appears to be the beginning of the degradation process at glass-molding temperatures. In addition, the creation of voids at the interlayer/substrate interface owing to the departure of interlayer materials results in the weakening of coating-substrate adhesion as well as the outward diffusion of substrate materials. As the service lifespan of the coated molds is vital to PGM application, further research is suggested to focus on quantitative modelling of the above degradation mechanisms to predict the lifespan of coated models for given coating structure and molding temperature.

2.2.2.3 Ruthenium as a metal coating

Ru, which is a cost-effective noble metal, has gained interest because its oxidation resistance is even higher than that of other noble metals, such as platinum (Pt) and iridium (Ir) [140]. Chen et al. [89] employed MoRu coatings on WC substrates; after annealing at 600 °C, they observed that coatings with high Ru content (at least higher than Mo content) exhibited superior oxidation resistance and higher hardness. Their results indicated that Ru is a suitable coating material for high-temperature applications. Ru has been used as a metallic film for contact switching in microelectromechanical systems (MEMS) with enhanced mechanical properties compared to Pt, gold (Au), rhodium (Rh), and silver (Ag) [141]. Although Ru, along with Pt, primarily appears as an electrocatalyst in the literature [142], owing to its higher oxidation resistance, it can be a coating material for PGM when an increase in chemical inertness is required, specifically when high-T_g glasses are subjected to molding.

Han et al.[143] deposited Ru thin films on Si substrates using pulsed CVD and ALD with the same thickness to compare the thermal stability of the surface characteristics before and after thermal annealing (Fig 2.10). The surface roughness and morphology were examined using atomic force microscopy (AFM). Fig. 2.10(a) shows the variation in roughness with rapid thermal annealing (RTA). In the as-deposited state, Ru thin films grown using pulsed CVD exhibited a smaller roughness than those grown by ALD owing to the smaller grain size. The AFM images of the annealed state (Fig. 2.10(b)) indicated that the small roughness of the CVD Ru films was maintained up to a high temperature of 800 °C, whereas the ALD Ru films had a significant increase in the roughness. In addition, ALD Ru films demonstrated void

formation owing to the excessive growth of grains, whereas a minor increase in grain size was observed for CVD Ru films. These results clearly indicated that CVD Ru films have higher thermal stability than ALD Ru films.

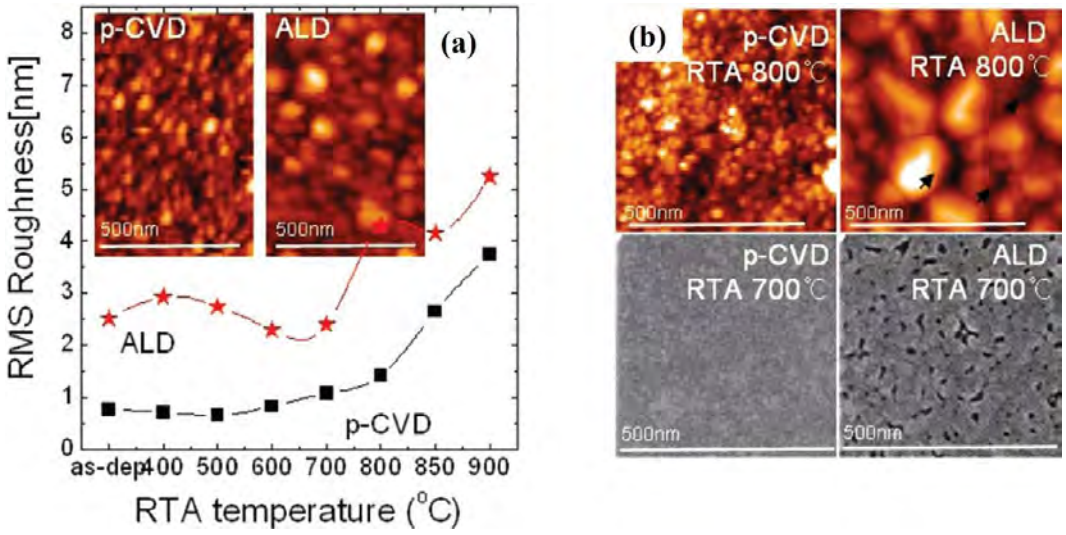

Figure 2.10 (a) Roughness comparison of Ru films deposited using p-CVD and ALD (inset AFM images), and (b) AFM images (upper part) at 800 °C and SEM images (lower part) at 700 °C of Ru films [143].

Chen et al. [144] developed TaRu coatings on WC substrates with a Cr interlayer using DC magnetron co-sputtering. Four alloy coatings ($Ta_{35}Ru_{65}$, $Ta_{45}Ru_{55}$, $Ta_{55}Ru_{45}$, $Ta_{64}Ru_{36}$) were achieved with pure metal targets (Ta, Ru, Cr) at 400 °C. To investigate the stability of TaRu coatings, they annealed the coatings in an oxygen-containing environment at 600 °C for 4 h and then cooled them to room temperature. Fig. 2.11 shows the XRD, SEM, and TEM analyses of the as-deposited and annealed TaRu coatings. In the as-deposited state, the XRD patterns revealed the reflections of hexagonal Ru, tetragonal β-Ta, and hexagonal RuTa (Fig. 2.11(a)), whereas the annealed coatings exhibited reflections of Ru, RuTa, and Ta_2O_5, indicating the oxidation of tantalum at 600 °C. The cross-sectional SEM images demonstrated the columnar morphology of the TaRu coatings on the substrate and the formation of an

oxide scale on the top surface of the coatings after annealing. The developed TaRu coatings with a relatively higher Ru content exhibited fewer thickness changes after annealing. With the minimum amount of Ru, the overall coating layer thickness $Ta_{64}Ru_{36}$ enlarged from 702 to 740 nm due to oxidation, which resulted in a layered structure (Fig. 2.11(e)). Because the $Ta_{64}Ru_{36}$ coating was annealed in an oxygen environment, the inward oxygen diffusion was faster than the outward Ta diffusion. In addition, Ta formed an oxide more easily than Ru, resulting in internal oxidation [145, 146].

Chen et al. [147] fabricated CrRu protective coatings by employing co-sputtering system with Ti (interlayer) on Si substrates. The CrRu coatings were deposited at 400 °C and then annealed in a 50 ppm O_2-N_2 environment for 2 h at 600 °C. Fig. 2.12 depicts the cross-sectioned microstructural behavior of the $Cr_{47}Ru_{53}$ and $Cr_{65}Ru_{35}$ coatings in the as-deposited and annealed state. After co-sputtering, $Cr_{47}Ru_{53}$ and $Cr_{65}Ru_{35}$ exhibited compact polycrystalline morphologies and columnar structures, respectively. After annealing, thick oxide scales formed on the surfaces of both co-sputtered coatings and the columnar structure transformed into a polycrystalline structure in the $Cr_{65}Ru_{35}$ coating. The size of the recrystallized grains was limited by the original columnar grain boundaries, resulting in smaller grains in the $Cr_{65}Ru_{35}$ coating than in $Cr_{47}Ru_{53}$. The SAED patterns indicated the CrRu and oxide-scale regions consisted of Ru-based alloys and Cr_2O_3, respectively.

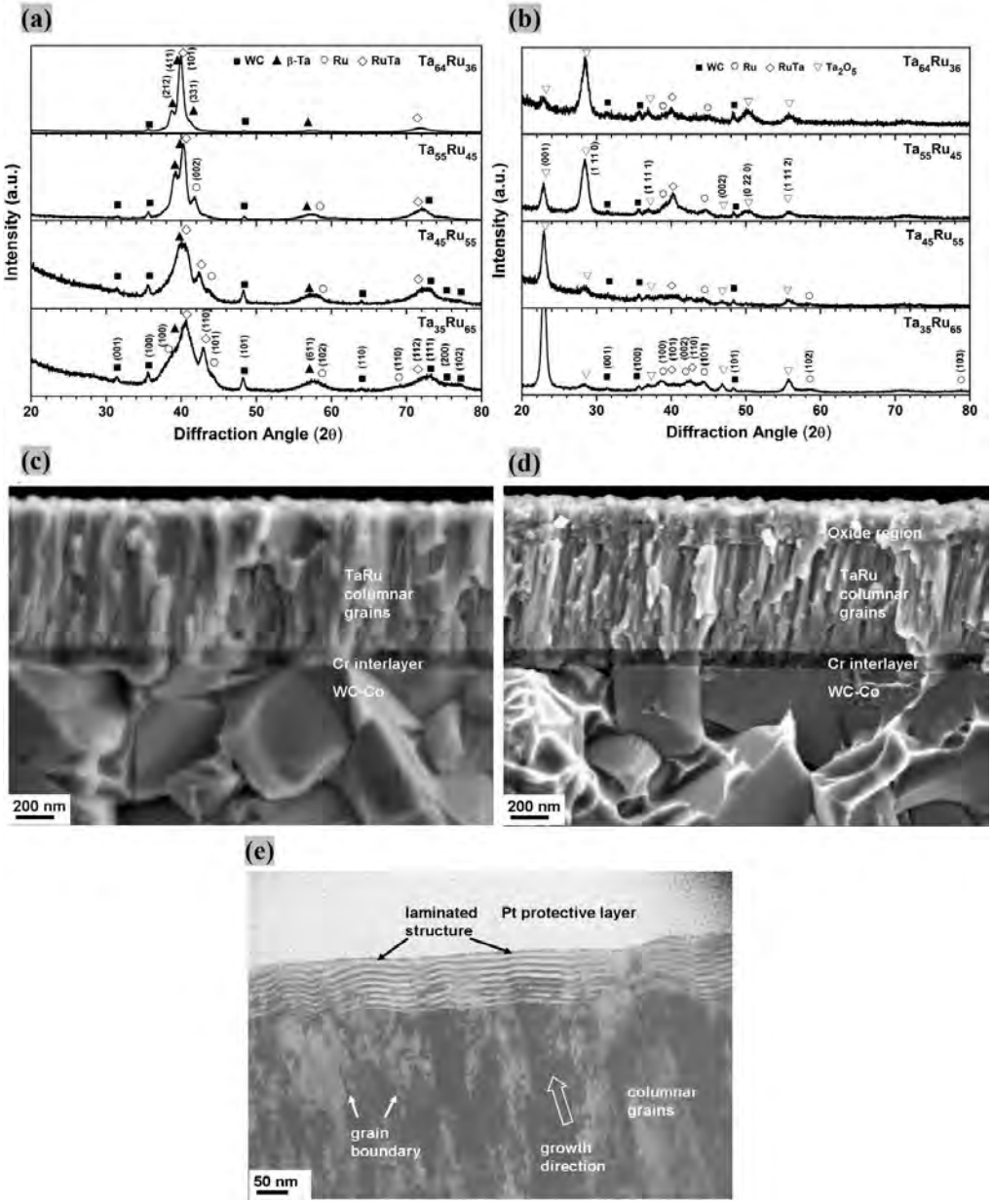

Figure 2.11 Study of $Ta_{64}Ru_{36}$ coatings: XRD patterns of the (a) as-grown and (b) annealed films, cross-sectioned SEM pictures of the (c) as-grown and (d) annealed coatings, and (e) TEM image (cross-sectioned) of the annealed films [144].

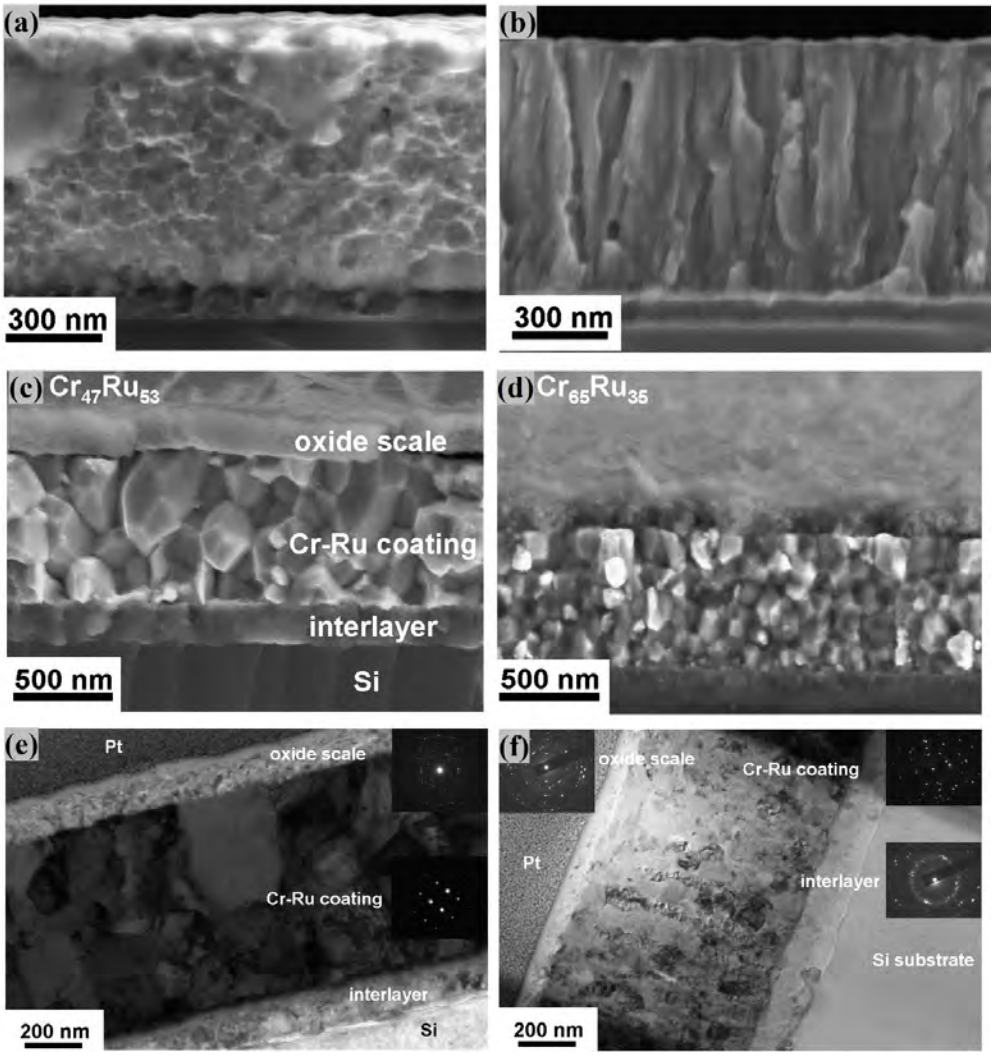

Figure 2.12 Study of $Cr_{47}Ru_{53}$ and $Cr_{65}Ru_{35}$ coatings characterized by SEM images of (a, b) as-deposited and (c, d) annealed coatings, and TEM images (cross-sectioned) of (e, f) annealed coatings [147].

2.2.3 Ceramic coatings

While noble metal coatings are more advantageous than ceramic ones in prolonging the lifetime of PGM tools, the research on ceramic coatings has not stopped because of the lower cost that can potentially achieve a better combination of cost and durability, particularly when higher temperatures in PGM are required. Li et al. [105] fabricated CrWN ($Cr_{35}W_{18}N_{47}$, $Cr_{27}W_{24}N_{49}$, $Cr_{18}W_{28}N_{54}$, and $Cr_{13}W_{31}N_{56}$) coatings on WC substrates using co-sputtering Cr and W targets in a plasma sputtering

system. The coating surfaces were analyzed using AFM before and after the pressing cycles of glass molding at a maximum temperature of 650 °C. As the W content increased, finer particle sizes and decreased surface roughness of the CrWN coatings were observed. The addition of W to CrN resulted in the formation of a dense and fine-grained structure of the coatings because the addition of W atoms in co-sputtering caused an enhancement in the collision of Cr and N. Additionally, mobility and diffusivity could be restrained by the higher W content. Previous studies [148, 149] reported that the increase in the energy of the (sputtering) W target caused a decrease in the surface roughness of the coatings. For the $Cr_{35}W_{18}N_{47}$ coating, the maximum and minimum particle sizes were 337 and 107 nm, respectively.

In addition, the formation of finer particles occurred in other coatings ($Cr_{27}W_{24}N_{49}$, $Cr_{18}W_{28}N_{54}$, and $Cr_{13}W_{31}N_{56}$) if the W target power was increased. Fig. 2.13 shows the surface morphology of the $Cr_{35}W_{18}N_{47}$ coating before and after thermal pressing cycles in a nitrogen environment. The surface roughness of the $Cr_{35}W_{18}N_{47}$ coating in the contact region with glass (Fig. 2.13(h)) and noncontact region (Fig. 2.13(i)) were 12.3 and 14.6 nm, respectively. The increase in the surface roughness of the noncontact region, associated with cracks, was caused by oxidation at high temperatures. The same phenomena were also observed for other coatings ($Cr_{27}W_{24}N_{49}$, $Cr_{18}W_{28}N_{54}$, and $Cr_{13}W_{31}N_{56}$). The extent of oxidation in the contact regions was relatively small because the cover glass inhibited the oxygen accessibility. Huang et al. [103] synthesized CrWN coatings with varying W contents using magnetron sputtering and examined the molding performance of the coatings in a nitrogen environment at 650 °C for 6 min. The fabricated coatings with varying W contents were $Cr_{34.45}W_{20.94}N_{44.61}$, $Cr_{28.03}W_{33.29}N_{38.68}$, $Cr_{18.90}W_{40.13}N_{40.97}$, and

$Cr_{15.73}W_{44.94}N_{39.33}$. In the $Cr_{34.45}W_{20.94}N_{44.61}$ coating, with a low W content, a coarse granular morphology was observed with many noticeable micro-sized pores. Although the deposition techniques were different, the effects of W content were the same as those revealed by Li et al. [105], that is, the increase in W content results in grain refinement and a smoother surface, but it aggravates oxidation.

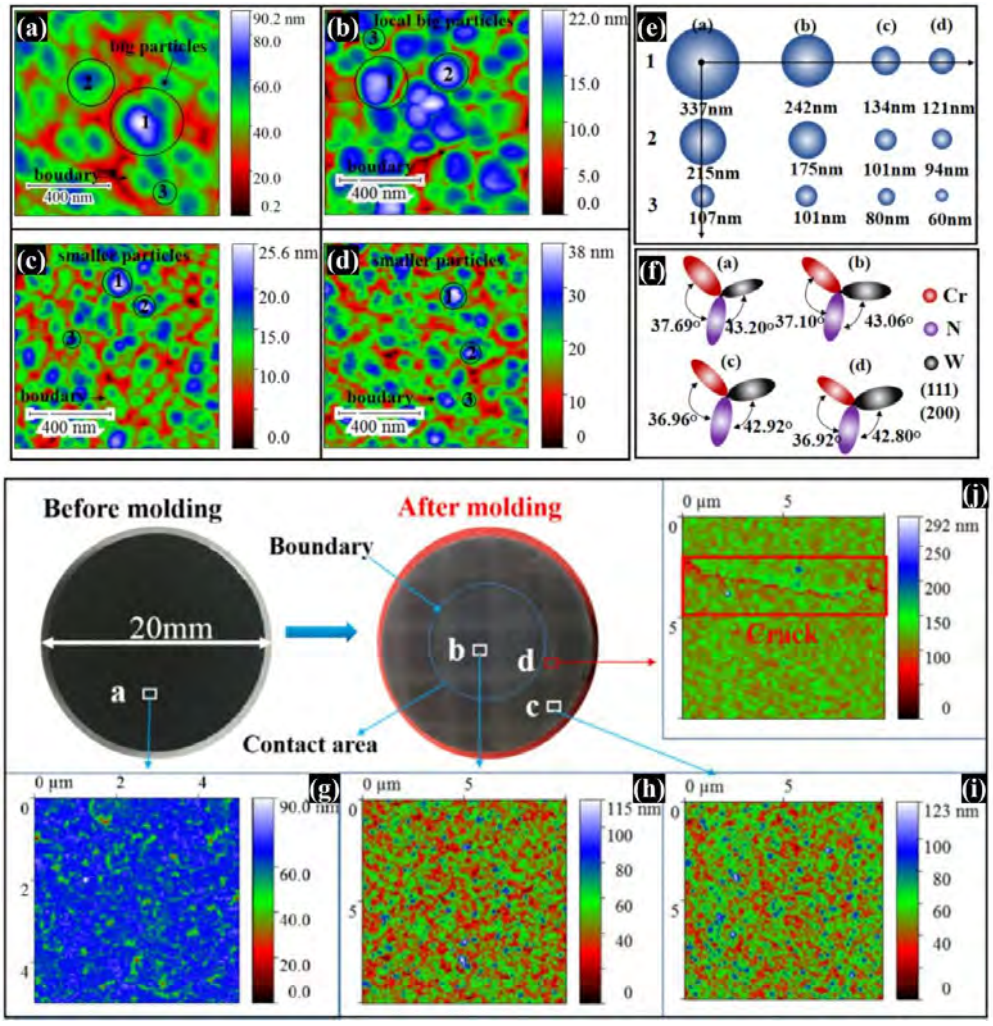

Figure 2.13 AFM study of CrWN coatings: (a–d) surface morphologies of as-deposited ($Cr_{35}W_{18}N_{47}$, $Cr_{27}W_{24}N_{49}$, $Cr_{18}W_{28}N_{54}$, and $Cr_{13}W_{31}N_{56}$) coatings, respectively, (g–j) surface morphology of annealed $Cr_{35}W_{18}N_{47}$ coating [105].

Li et al. [105] schematically revealed the degradation mechanism of CrWN coatings (Fig. 2.14). At the molding temperature in the PGM, the top surface of the

coatings experienced high pressure. As the number of thermal cycles increased, the columnar voids of the coated structure provided diffusion channels for oxygen. In addition to the formation of surface oxide layers, internal oxidation also occurred. The aggravation of W and Cr oxidation significantly reduced the integrity of the coatings. The anti-adhesion and mechanical properties decreased abruptly, and cracks were observed owing to the interfacial reaction, sticking, and oxidation. With the increase in thermo-mechanical cycles, the cracked coatings eventually fell off owing to the sticking and demolding forces.

Chen et al. [96] prepared TaSiN coatings via magnetron co-sputtering on Si substrates. The cross-sectioned TEM images of the coating before and after annealing at 600 °C are shown in Fig. 2.15. The selected-area diffraction pattern (SADP) demonstrated a non-crystalline phase. The HRTEM image revealed the stacking of the coating constitution with periodic gradient concentration; however, the lattice fringes were not identified. In the annealed state, the $Ta_{27}Si_{20}N_{53}$ coating exhibited an oxide scale formed on the surface. Underneath the oxide scale, the amorphous structure of the coatings was maintained (inset of Fig. 2.15(c)). The oxide scale continued to expand during prolonged heating and remained amorphous, whereas the internal part of the coating demonstrated crystalline domains embedded in the amorphous matrix. The crystalline domains were determined based on the apparent lattice fringes, which is attributed to the Ta_2N and TaN phases.

Chen et al. [104] further investigated the chemical inertness of silicon-nitride-based ($Cr_{28}Si_{17}N_{55}$, $Ta_{26}Si_{14}N_{60}$, $Zr_{16}Si_{20}N_{64}$) coatings in contact with SiO_2-B_2O_3-BaO glass at temperatures between 270 and 600 °C (Fig. 2.16). For the $Cr_{28}Si_{17}N_{55}$ coatings, significant glass adhesion was observed after the first ten thermal cycles.

After 100 thermal cycles, the optical microscopy (OM) and SEM images revealed a damaged surface, indicating adhesiveness with glass. The WC substrate underneath was exposed, which was also confirmed using EDS analysis. After 400 thermal cycles in the $Ta_{26}Si_{14}N_{60}$ coatings, the contact region of the coating with glass became opaque (the as-deposited coatings were transparent), possibly because of the formation of oxide islands with a maximum diameter of 200 nm, as observed in the contact region. Moreover, the original granular morphology was retained in the noncontact region.

Accordingly, after 600 thermal cycles, the TEM image (Fig. 2.16(f)) of the $Ta_{26}Si_{14}N_{60}$ coatings revealed the formation of an oxide scale on the coating surface and the expansion of the interlayer area. Based on the EDS analysis of the surface oxide, no identification of Ti was observed, which indicated that the $Ta_{26}Si_{14}N_{60}$/Ti/WC coating restricted the outward diffusion of Ti. After being heated for 400 cycles, the $Zr_{16}Si_{20}N_{64}$ coatings became translucent, i.e., the granular morphology underneath the coatings could be partially observed. This was because the island oxides were smaller (~20 nm) than those in the heated $Ta_{26}Si_{14}N_{60}$ coatings. With continued annealing after 600 and 800 thermal cycles, the oxide particles further expanded to 20–40 nm and 150 nm, respectively (Fig. 2.16(h) and 2.16(i), respectively). The elemental mapping of the $Ta_{26}Si_{14}N_{60}$ coatings in the contact region indicated that the oxide particles had high amounts of Ba and O with low levels of N and Zr. These results indicated that the $Zr_{16}Si_{20}N_{64}$ coatings demonstrated better chemical inertness than $Cr_{28}Si_{17}N_{55}$ and $Ta_{26}Si_{14}N_{60}$ against BK7 optical glass. Chang et al. [100] also studied the oxidation resistance of ZrSiN coatings at 600 °C. Their results indicated that the improved oxidation resistance was associated with the formation of dense Zr-Si-O oxide scales that inhibited oxygen diffusion.

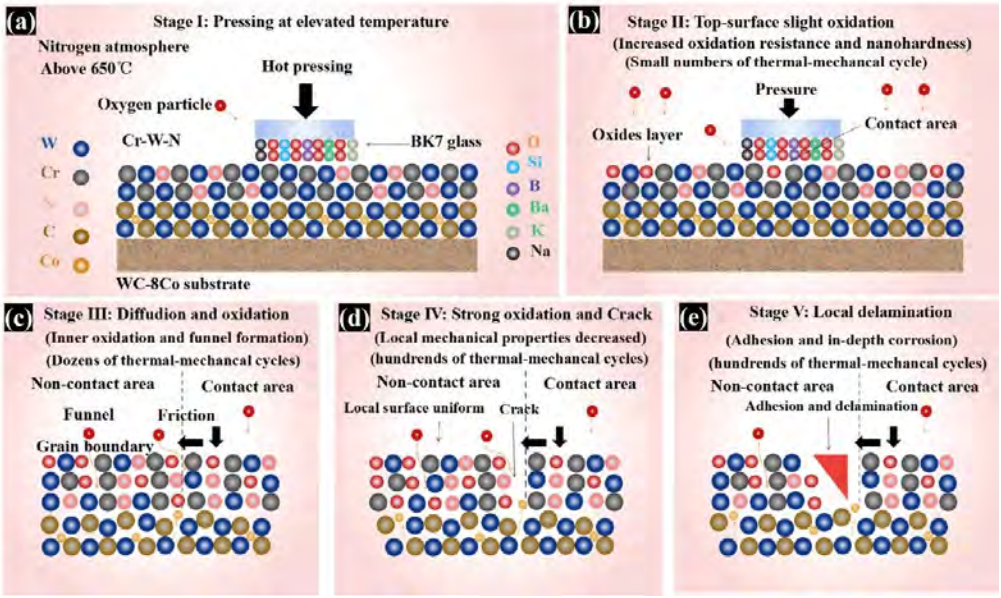

Figure 2.14 Illustration of the degradation mechanism of CrWN coatings in contact with BK7 optical glass [105].

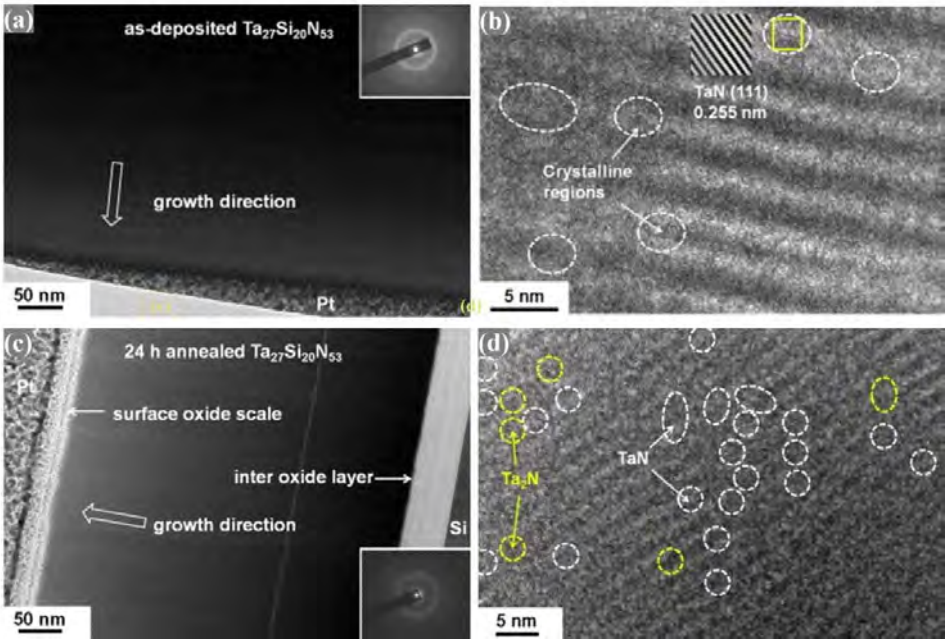

Figure 2.15 Cross-sectioned TEM/HRTEM images of $Ta_{27}Si_{20}N_{53}$ coatings in the (a, b) as-deposited and (c, d) annealed states [96].

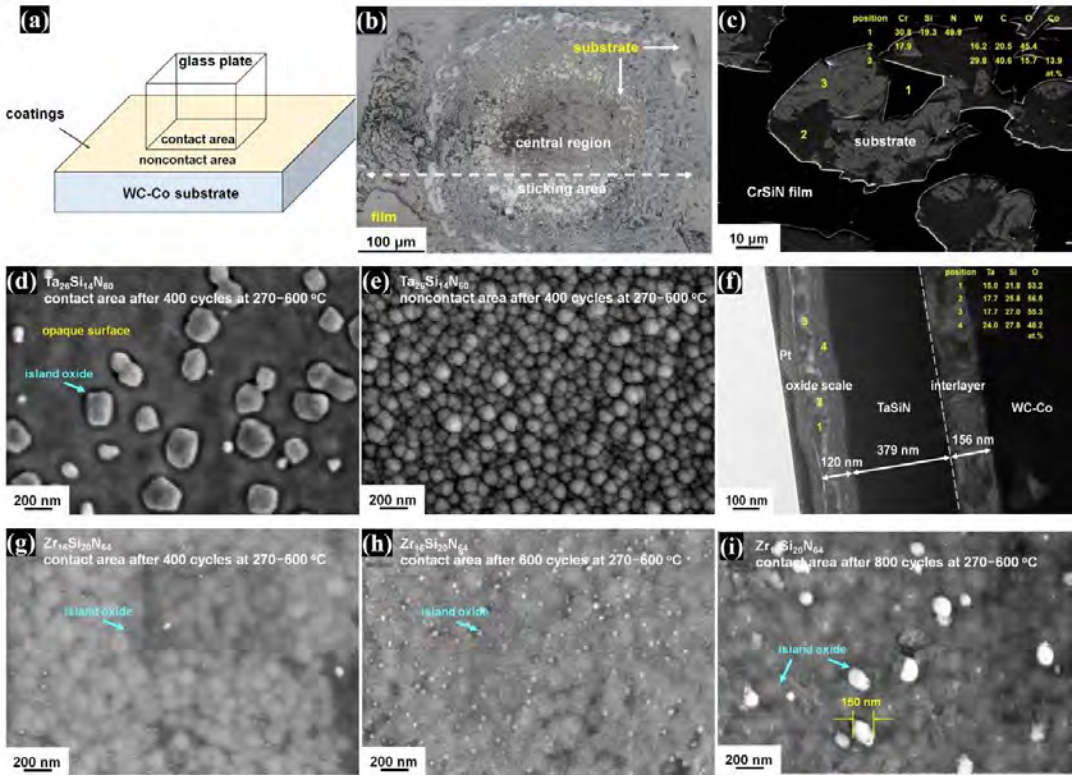

Figure 2.16 Study of SiN-based coatings: (a) schematic of glass/sample in heating test, SEM images of (b–c) $Cr_{28}Si_{17}N_{55}$ coatings, (d–f) $Ta_{26}Si_{14}N_{60}$ coatings, and (g–i) $Zr_{16}Si_{20}N_{64}$ coatings after heating [104].

2.2.4 Diamond-like carbon (DLC) coatings

DLC coatings encompass a wide range of carbon-based protective coatings. Owing to enhanced wear-resistance and low coefficient of friction, they are generally used as protective layers against friction and various applications in which low friction is required [48]. The different properties of DLC coatings, such as chemical/ mechanical properties, are evaluated by the sp^2/sp^3 content ratio as well as hydrogen content. The DLC coatings containing a high content (more than 40% [150] or 60% [54]) of sp^3-modification without any hydrogen are named as tetrahedral amorphous carbon (ta-C) coatings. These coatings have excellent properties, including high hardness, high density, low abrasion rates, and low chemical reactivity.

Generally, PVD processes such as conventional sputtering can only induce less than 40% content of sp^3 because the carbon ions are unable to gain sufficient energy and are deposited on the substrate's surface with little momentum, resulting in inadequacy in the formation of sp^3 bonds. Consequently, most carbon particles accumulate in small grains, resulting in graphite modification [151]. The deposition of (ta-C) DLC coatings with a high sp^3 content requires specialized deposition techniques such as filtered cathodic vacuum arc (FCVA) deposition, which are not commonly used in the industry.

Bernhardt et al. [54] developed ta-C coatings with an sp^3 ratio of approximately 60% using magnetron sputtering ion plating (MSIP) on a WC substrate for glass molding applications and annealed in a vacuum environment with glass at different temperatures of 590 and 630 °C. Most of the coated surfaces corrugated after annealing because of residual stresses; only few of them kept a good smoothness of the surfaces. Zhang et al. [85] fabricated DLC coatings on WC substrates using FCVA and ion-assisted magnetron sputtering methods and reported that the occurrence of graphitization at temperatures above 450 °C dramatically affects the lifespan of coated molds in PGM. Although DLC coatings offer high degree of self-lubrication with improved anti-wear properties, their poor thermal-stability and the requirement of the dedicated coating facility restricts their applications in the glass molding industry [54, 55]. Additionally, although a few attempts have been made to employ DLC coatings for PGM applications, owing to the graphitization, it tends to oxidize at high temperatures and in an industrial production environment (e.g., with a constant N_2 flow), rendering it unsuitable for glasses with high T_g (e.g., $T_g \geq 550$ °C).

2.3 Tribological Performances

In addition to thermal/chemical stability and anti-stick performance, coatings must also have high toughness, high hardness, and low friction for PGM applications that involve the flow of glass on a coating surface. Among these, hardness is the most important for industrial coating applications involving contact and sliding [152]. Nanoindentation is employed to quantify it, in which a diamond-tipped indenter is forced into a coating surface. Subsequently, the elastic properties and hardness are determined based on the recorded force-indentation curve.

Nanoindentation is considered one of the fastest and simplest methods for obtaining information about the mechanical properties of thin films [153]. To avoid the influence of the substrate, a general rule of thumb to obtain precise measurements of hardness (H) and Young's modulus (E) of thin films is that the indentation depth must be less than one-tenth of the overall coating thickness [154].

Wei et al. [102] performed nanoindentation for monolayer and multilayer Re/Ir coatings and observed that the multilayer Re/Ir coating exhibited a higher Young's modulus and hardness than those of the monolayers (Re or Ir). The significant enhancement in the mechanical properties of the multilayered coating was determined to be primarily due to dislocation blockage by interfaces [155]. In addition, as the grain size is constrained by the layer thickness, the hindrance of dislocation increases with refinement in grain size, which results in higher hardness. Moreover, the multilayer structure can also contribute to the coating toughness [116] because the interfaces result in an enhancement in the resistance to crack propagation. Based on a series of studies on Re/Ir coatings, it appears that the multilayer design has an

overwhelming advantage over monolayer coatings in terms of both tribological and chemical properties.

The nanoscratch test is also commonly used to determine the adhesive properties of coatings and thin films [156, 157], in which the lateral force is measured while moving an indenter tip that has been forced into the specimen [158]. Using a constant rate of increase in the normal force and a constant scratching speed, Klocke et al. [69] investigated the influence of the interlayer material and its thickness on the adhesion of the PtIr film. They observed that in the absence of an interlayer, a steep increase in the indentation depth was developed in the early stage of scratching and that the adhesion and hardness of the PtIr film were improved after depositing the Ni or Cr interlayer. The critical scratch load increased with the interlayer thickness, and the 50-nm Cr interlayer performed the best in resisting exfoliation. The probable reasons for the improvement in adhesion are the enhanced compatibility of the mechanical properties between the coating and substrate and the establishment of stronger bonds at the interfacial area of the material.

In the load-control mode, a nanoindenter tip can repeatedly hit a coating surface with a prescribed maximum load. This is called a nanoimpact test [159], which may determine the toughness of the coatings. In the nanoimpact test, a solenoid is employed to drag the indenter from the surface and perform the re-acceleration from a short distance opposite to the film. The repetition of impacts at the same location is enabled by proper automation. The development of indentation depth against repetitive impacts is continually monitored. Thus, the progress of film deformation is captured. For the PtIr coatings, nanoimpact tests have been performed to study the effects of interlayers (Cr and Ni) with varying thicknesses [69]. The interlayer was

observed to improve the resistance to repetitive impacts. In particular, with the employment of a Cr interlayer of 50 nm, the imprint depth remained almost unchanged up to nearly 1500 impacts. This result was ascribed to the plastic deformation of the film during several initial impacts and the work hardening effect to resist further impacts. For all other examined scenarios, a progressive film fracture occurred as the number of impacts increased, resulting in a continuous increase in the imprint depth. Consequently, it was concluded that the Cr interlayer with a thickness of 50 nm provided a significant toughening effect on the entire coating structure to withstand repetitive impact loading. Conversely, the coatings without adhesive interlayer coatings failed rapidly during the impact tests.

Huang et al. [103] determined the mechanical properties of CrWN coatings through nanoindentation. They observed that co-sputtered coatings with increased W content after annealing at 650 °C resulted in higher hardness, and coatings with a high H/E (i.e., hardness over Young's modulus) ratio demonstrated good fracture toughness. In another study, Huang et al. [160] compared the mechanical performance of CrWN coatings heated at 650 °C in vacuum, nitrogen, and air environments. The evaluation using nanoindentation demonstrated that the vacuum-annealed coatings exhibited a noticeable age-hardening effect, and therefore, the significant improvement in mechanical properties was ascribed to spinodal decomposition. In contrast, the CrWN coatings annealed in nitrogen and air environments suffered from substantial mechanical degradation caused by oxidative damage. Chang et al. [161] evaluated the hardness of Hf-Si-N coatings using nanoindentation and observed that after annealing (at 600 °C), the hardness of the coatings initially increased and then decreased with continuous annealing (100 h), owing to the formation of an oxide scale

on the surface. Guo et al. [106] examined the mechanical performance of CrWN coatings before and after annealing at 650 °C under vacuum and concluded that both the nanohardness and Young's modulus increased after annealing owing to the occurrence of an age-hardening mechanism. Thus, based on the literature, it is appeared that nanoindentation is a unique depth-sensing technology, which is employed to precisely determine the mechanical properties of the thin films.

2.4 Summary

In this chapter, major coating techniques are summarized and coating performances for PGM applications were evaluated. Glass molding tools must possess high-temperature strength as well as significant resistance to oxidation and wear, which can be accomplished through the application of an appropriate coating material and fabrication method. According to previous studies, PtIr coatings with different interlayers are the most frequently used on molding tools to achieve non-adhesive characteristics with glass and thermal stability at glass molding temperature in PGM. Nevertheless, these coatings potentially experience oxidation and glass adhesion issues at temperatures beyond 700 °C. Additionally, Ir is highly expensive. Therefore, in order to solve these issues, a new coating system is necessary. Ru possesses superior oxidation resistance and good mechanical properties within the group of noble metals, making it a possible choice for PGM at high temperatures. Moreover, Ru is significantly lower in cost than Ir. Ceramic coatings may still play a role in the future development of PGM coatings because they are less expensive than noble metals. Efforts have been made with conventional nitrides, such as, TiAlN, CrN and CrWN. However, their performance in PGM is barely adequate enough due to their reaction

and adhesion with glass. Therefore, combination of metallic and ceramic coatings can also be developed to make it cost-efficient at industrial scale.

Chapter 3: Methodology

3.1 Materials

Pure Ru (99.95%), Pt (99.99%), Cr (99.95%), and Ti (99.95%) were employed as the target materials. Graphite materials were purchased and adopted as the substrate materials. The substrate samples were initially ground mechanically with silicon carbide papers and then polished by applying diamond slurry to achieve a highly smooth surface. The grinding/polishing materials were purchased from the Buehler company.

3.2 Thin film deposition

Deposition of thin films was carried out using a magnetron sputtering system (Denton Explorer 14), which is a plasma-based physical vapor deposition (PVD) technique. This technique involves the creation of magnetically confined plasma at or near the target material surface. The collision of ions from plasma with the target material causes the ejection of atoms, which are the then sputtered or deposited onto the substrate surface to form thin films. This system is equipped with a maximum of four cathode guns. Alternative deposition was performed by switching on one target and switching off other targets by keeping their shutters closed to avoid “cross-talk.” The sputtering machine employed in the synthesis of the coatings is shown in Fig. 3.1.

Figure 3.1 Denton Explorer 14 sputtering system.

3.2.1 Ru–Pt coating design

In the past studies, protective coatings of Pt, Ir, Re, and in particular PtIr, were extensively employed on molding tools to achieve thermal stability and anti-sticking property in PGM. However, these coatings still suffer from glass adhesion and oxidation problems at temperatures beyond 700 °C. Furthermore, Ir is quite expensive, which further limits its industrial application. Therefore, to address these issues, a new coating technology is essential. Ru, which is a more cost-effective noble metal than Ir, possesses superior oxidation resistance and mechanical performance and, based on its properties, it can be a potential candidate for PGM where high temperature is required (>700 °C). Therefore, a Ru–Pt coating system was fabricated using DC magnetron sputtering to evaluate its performance for high-T_g PGM. A multilayer coating design (Ru–Pt) was adopted to achieve improved mechanical performance and better anti-sticking property.

Generally, an interface between two coating layers act as a barrier to the dislocation motion and promotes the mechanical performance of the coatings. In addition, coherency strains are formed at the interface for various nanocrystalline grains, which leads to hardness improvement. Moreover, the ordered nanostructure enhances the bonding at the interface (e.g., Pt and Ru), making it harder for the glass constituents (such as Al, Si) to penetrate the coating films and facilitating the repulsion of glass adherence to the substrate. The following section describes the fabrication of the Ru–Pt coating design.

Pure Ru, Pt, and Ti disks with diameters of 50.8, 50.8, and 76.2 mm, respectively, were utilized as the sputtering targets with constant substrate-to-target distance in the vacuum chamber. Before the deposition process, the vacuum chamber was pumped down to 8×10^{-7} torr followed by argon (Ar) gas inlet as plasma source. The Ar flow rate was maintained at 30 sccm, and all the targets were pre-sputtered to obtain clean target surfaces. A Ti interlayer with thickness of 50 nm was deposited on the graphite substrates to improve adhesion between the protective coating and substrate. Multilayer Ru–Pt coatings were accomplished by alternative deposition of coating (Ru, Pt) layers, each with an individual thickness of 40 nm. The total number of deposited layers were 21, starting and ending with Ru (Ru–Pt–Ru–Pt–Ru…Pt–Ru); thus, the total thickness of the multilayer coating was 840 nm. Monolayer Ru or Pt coatings with a thickness of 840 nm were deposited on substrates with 80 W input power as the control samples. A schematic of the monolayer and multilayer coatings is shown in Fig. 3.2. The detailed control parameters for the deposition of thin films are summarized in Table 3.1.

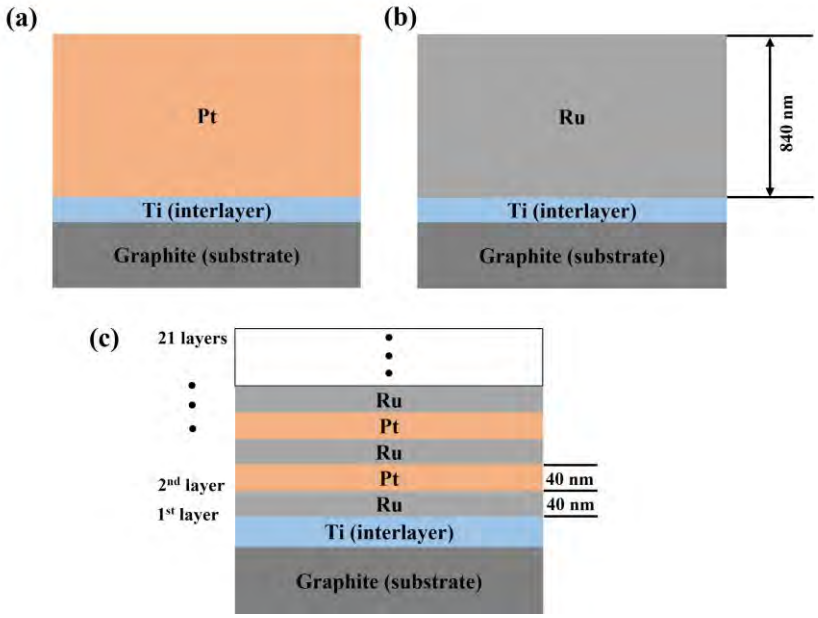

Figure 3.2 Schematic of monolayers (a) Pt, (b) Ru, and (c) multilayer Ru–Pt coatings.

Table 3.1 Deposition parameters for Ru–Pt multilayer coatings

Target	Power (DC)	Each layer time (s)	Base Pressure	Cathode gun
Ti	150 W	667	8×10^{-7}	1
Ru	80 W	533	8×10^{-7}	4
Pt	80 W	240	8×10^{-7}	2

3.2.2 Ru–Cr coating design

Hard protective coatings are widely employed as a surface engineering technique to enhance the wear resistance of tools [162]. Cr is a low-cost metal, which readily oxidizes to form a protective Cr_2O_3 film with thermal stability of up to 1200 °C [163], and it is suggested to protect the underlying coating from further degradation. Cr possesses relatively higher melting point with much lower cost than Pt and owing to its excellent corrosion/wear resistance properties, it appears to be a feasible candidate to replace Pt. Therefore, in order to significantly reduce the cost of industrial PGM

coatings while maintaining their effectiveness, Cr is employed as a coating element to further investigate its applicability in PGM. More specifically, the oxidation behavior of Cr was investigated with different thicknesses of the Ru film.

The deposition of thin films was carried out by magnetron sputtering (Denton Explorer 14 sputtering System) of metallic targets of Cr and Ru films with titanium Ti as interlayer on graphite substrates. Metal disks of Ru, Cr, and Ti with diameters of 50.8, 50.8, and 76.2 mm, respectively, were used as the sputtering targets and installed in the vacuum chamber. The dimensions of the graphite substrates were (2 * 7 * 7) mm, and they were metallographically ground and polished with diamond paste to obtain an ultrasmooth surface. The substrate samples were placed on the substrate holder and rotation speed was adjusted at 50 rpm for better uniformity. Prior to the deposition phenomena, the vacuum chamber was evacuated down to 8×10^{-7} torr followed by argon (Ar) gas inlet as plasma source. The flow rate of Ar was maintained at 50 sccm and all the targets were pre-sputtered to clean the target surfaces. A Ti interlayer with thickness of 50 nm was deposited on the substrates with DC power of 150 W. Four different Ru–Cr coating systems with varying thicknesses of Ru were deposited, as depicted in Fig. 3.3. The sputtering powers of Ru and Cr during deposition were 80 W each.

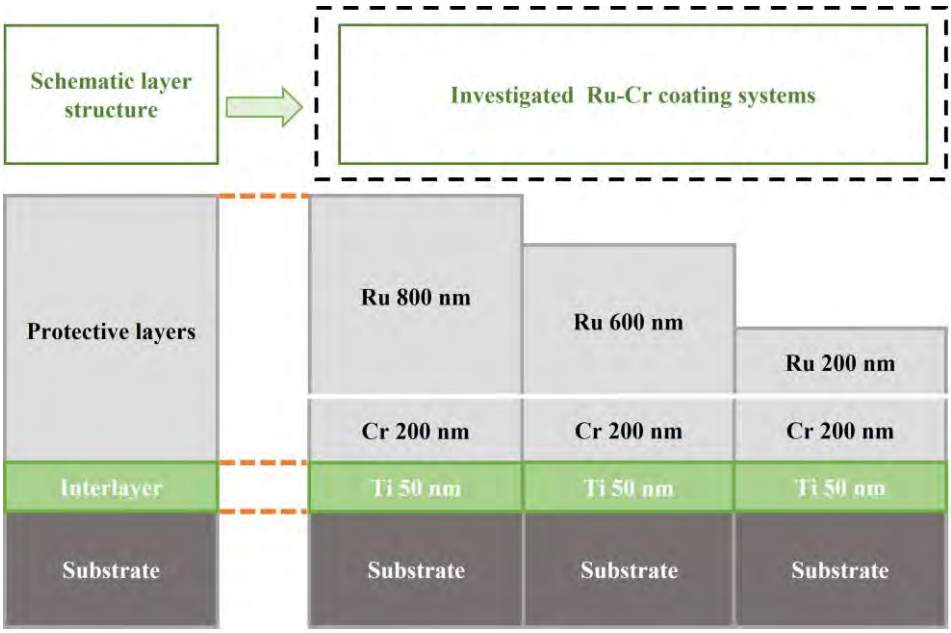

Figure 3.3 Schematic of Ru–Cr coating design.

3.3 Annealing tests

An OTF-1200X quartz tube furnace (Fig. 3.4) was used for annealing experiments at the glass molding temperature to evaluate all of the as-deposited coatings. The samples were annealed with an ASG (Corning gorilla glass 5, $T_g \approx 630$ °C) covering to examine the anti-sticking property. The coated samples were placed inside the quartz tube furnace and evacuation of the quartz tube was carried out to ~1 mbar using a vacuum pump. All of the coated design samples were annealed at the desired temperature (750 °C) with different time durations. The choice of temperature was based on the industrial production requirement, which is T_g + 120 °C.

To investigate the chemical inertness of the developed coatings (Ru–Pt), an ASG piece (Corning Gorilla glass 5, $T_g \approx 630$ °C) was positioned on the coated samples and heated in a quartz tube furnace under a rough vacuum (~1 mbar) condition. Annealing involved the rise in temperature with a heating rate of 5 °C/min from room

temperature to 750 °C and soaking for 2, 20, and 40 h, respectively. Afterwards, the annealed samples were cooled down in the tube furnace to room temperature.

The Ru–Cr as-fabricated coated samples were annealed from room temperature (25 °C) to 750 °C at a rate of 5 °C/min and maintained for 10 and 20 h. Following that, the annealed samples were subsequently cooled to room temperature inside the quartz tube furnace.

Figure 3.4 OTF-1200X quartz tube furnace.

3.4 Microstructure and mechanical characterization

The microstructural examination of the developed coatings before and after the annealing was carried out using different characterization techniques, which are described below:

3.4.1 X-ray diffraction (XRD)

XRD is a promising characterization method for materials with crystalline structures. XRD is based on the occurrence of a constructive interface between the monochromatic x-rays and crystalline samples following Bragg's law [164]. Generally, XRD is employed to identify the crystalline phases in a material. In the experiments, an X-ray diffractometer (Rigaku SmartLab) with Cu-Kα radiation operated at 45 kV and 200 mA was adopted for phase identification in the developed

coatings before and after annealing. The XRD (θ–2θ) scanning was carried out in parallel beam (PB) mode with scanning range and scanning speed of 10–90° and 5°/min, respectively. For identification of the phases, positions, and intensities of the obtained XRD data peaks, they were compared with standard XRD data peaks of known crystalline materials.

3.4.2 Scanning electron microscopy (SEM)

SEM is an extensively employed technique for visualizing the surface microscopic features of diverse materials. The images are obtained when an electron beam is focused on the specimen, and the image creation phenomenon is entirely dependent on the high energy electron beam, which is transformed into secondary electrons and back-scattered electrons, which are then recorded by detectors to produce an image. In the experimentation, the evaluation of surface morphologies of the coated samples was carried out using a SEM-TESCAN VEGA3. Another significant feature equipped with SEM characterization systems is energy dispersive x-ray spectroscopy (EDS or EDX), which provides the chemical characterization or elemental analysis of the specimen. When the tested material is irradiated with electrons, it results in x-rays emissions that are unique to the elements present. The conversion of energy emissions into varying peak intensities provides a spectrum profile, which identifies the various constituents of elements present in the sample. In the EDS testing, various areas of the coated samples were analyzed to obtain the elemental analysis on the surface of the sample.

3.4.3 Scanning probe microscope (SPM)

The SPM is an equipment employed for examining the surfaces of the sample at nanoscale level. It utilizes a highly sharp tip, known as a cantilever, to scan the surface of the sample while the scanner moves backward and forward to acquire information from the surface of the sample. The SPM examines and provides mapping of the surface morphology. The tapping mode of the SPM is a gentler mode of measuring the surface topography and subsequently, the surface roughness. In this dynamic mode, the tip oscillation at the resonance frequency interacts with the surface with constant oscillation amplitude. Several parameters are available to quantify the surface roughness, for example, either by the calculation of the surface profile (area) or cross-section (line). Owing to that reason, only those instruments that provide quantitative measurement of z data can provide data that can be examined for surface roughness. During the SPM operation, information regarding the calculation of surface roughness was acquired in the tapping mode. The two most frequently calculated surface roughness parameters are arithmetic mean deviation (S_a) and root mean square mean deviation (S_q). For the image being analyzed, S_a is defined as follows:

$$S_a = \frac{1}{n}\sum_{i=1}^{n}|y_i| \qquad (3.1)$$

Likewise, RMS roughness (S_q) is calculated as

$$S_q = \sqrt{\frac{1}{n}\sum_{i=1}^{n}y_i^2} \qquad (3.2)$$

3.4.4 X-ray photoelectron spectroscopy (XPS)

XPS is a highly surface-sensitive technology used to study the surface chemistry of various materials. In XPS analysis, high-energetic x-rays strike the sample surface and photoelectrons are ejected with a specific kinetic energy, which is recorded. The kinetic energy is directly associated to the binding energy of the photoelectrons of the parent atom and is unique of the element and its chemical state. XPS spectra are obtained during the emission of photoelectrons of specific kinetic energy from the sample surface (~1–10 nm). The chemical binding of the coating elements was studied experimentally using XPS (Thermo Scientific Nexsa) at a vacuum base pressure of < 5×10^{-10} mbar.

3.4.5 Nanoindentation

Nanoindentation is an appropriate technique to measure the mechanical properties of thin films while eliminating the substrate effect, considering that the depth of the indentation is generally less than 10% of the film thickness [165]. To determine the elastic modulus and hardness, it employs load–displacement curves through a sequence of indents having depths of several tens of nanometers. A typical load–displacement curve includes the loading section, momentary holding section at peak load, and unloading section in which the indent displacement is retracted owing to the elastic characteristic of the specimen (material). Hardness is evaluated by dividing the maximum indentation load by the mean contact area, whereas the elastic modulus is derived by the slope (unloading section), which entirely indicates the elastic behavior of the tested sample.

During the process of loading and unloading in the nanoindentation method, the machine continually records the load (*P*) against indentation depth (*h*). After recording the *P–h* curve, the H can be determined as [166]

$$H=\frac{P_{max}}{A} \qquad (3.3)$$

where P_{max} is the maximum indentation load, and A represents the projected contact area between the specimen and indenter. The effective modulus (E_{ff}) can be calculated as [166]

$$E_{eff}=\frac{\sqrt{\pi}}{2}\frac{dp}{dh}\frac{1}{\sqrt{A}} \qquad (3.4)$$

where dp/d*h* is the slope of the (load–displacement) unloading curve at the maximum indentation depth. The elastic modulus of the indented material can then be calculated by substituting E_{eff} in the Eq (3.5).

$$\frac{1}{E_{eff}}=\frac{1-\upsilon^2}{E}+\frac{1-\upsilon_i^2}{E_i} \qquad (3.5)$$

where E_i and υ_i are the elastic modulus and Poisson's ratio of indenter, respectively, and E is the elastic modulus of the indented material.

Nanoindentation tests were performed on all the coated samples to determine mechanical properties using a Berkovich indenter (Hysitron Nanoindentation system). All of the samples were cleaned with an air pump before mounting in the machine. Before performing the nanoindentation test, calibration of the machine was carried out on fuse quartz. For Ru–Pt and Ru–Cr coatings, maximum loads of 250 and 170 μN, respectively, were used to avoid the influence of the substrate.

3.5 Nanostructure Characterization

3.5.1 Focused ion beam (FIB) techniques

The FIB technique is widely utilized for micro-machining with nanoscale (nanometer) precision and is extensively used for TEM lamella preparation. In FIB, a gallium ion source with accelerating voltages of up to 30 kV is used, and material interaction with the resultant emission allows elimination (removal) of the material (Ga ions/specimen interaction) or material deposition (Ga ions/Pt precursor interaction). In the experimental procedure, a dual-beam FIB equipped with ultrahigh electron beams and ion beams was employed to prepare cross-sectional TEM specimens from the bulk samples. Before ion-beam cutting, the deposition of the Pt protection layer was carried out on the specific surface area of the sample using e-beam deposition at 2 kV and then ion-beam deposition at 30 kV. Then, the sample was deeply trenched in the Pt-coated area by the gallium ion beams. Following that, the TEM micro-sample was extracted from the bulk sample, lifted out using a micromanipulator, and then transferred and welded to a TEM sample mount. Further thinning of the lamella was conducted with FIB milling to achieve electron transparency (<100 nm).

3.5.2 Scanning/transmission electron microscopy (S/TEM)

TEM is a highly effective characterization technique, which is commonly utilized to examine the various characteristics of thin samples. In TEM, a structural image is obtained when the electrons are transmitted through ultra-thin samples [167]. STEM is a type of TEM in which an electron beam focuses on a fine spot and images are formed when a convergent electron beam passes through the specimen, whereas

in TEM, a parallel beam of electrons passes through the ultra-thin specimen. STEM provides high-resolution imaging. The nanostructures of the multilayered coatings was investigated using a scanning/transmission electron microscope (S/TEM, FEI Talos 200X) operated with 200 kV. This instrument is equipped with multi-segment detectors, which allows imaging in bright-field, dark-field, and high-angle annular dark fields. STEM analysis of ultra-thin specimens was performed at a low acceleration voltage. EDS elemental analysis and selected area electron diffraction (SAED) structural analysis were also carried out.

3.6 Phase-field modeling (PFM)

For Ru–Cr coatings, a multi-phase-field model was established to analyze quantitatively the evolution of the oxide layer during the annealing process. The derived Allen–Cahn equations and Fick's law were coupled to illustrate the interdependency between the diffusion and oxidation reaction. Based on these governing equations, the attenuation effect of the Ru layer, the growth velocity and thickness of the oxide layer, and the concentration of Cr and oxygen can be quantitively studied. Therefore, this model is an effective tool to guide experiments and predict the experimental results.

Generally, the oxidation process for Cr can be expressed as

$$3O + 2Cr \rightarrow Cr_2O_3 \qquad (3.6)$$

The total Helmholtz free energy F for the discharge and charge can be expressed as

$$F\left(\boldsymbol{\eta}, \nabla\boldsymbol{\eta}, \mathbf{c}, \mathbf{d}\right) = \int_{\Omega} f d\omega = \int_{\Omega} f_{chem} + f_{\text{int}} d\omega \qquad (3.7)$$

where Ω is the discharge domain, f represents free energy density, f_{chem} and f_{int} denote the chemical potential energy density and interface energy density, respectively. The order parameter $\boldsymbol{\eta}$ and the concentration $\mathbf{c}$ are two series of variables:

$$\boldsymbol{\eta} = \{\eta_1, \eta_2, \eta_3, \eta_4\} \tag{3.8}$$

$$\mathbf{c} = \left\{c_{Cr}, c_O, c_{Cr_2O_3}, c_{CrO}\right\} \tag{3.9}$$

where η_1, η_2, η_3, and η_4 signify the Cr layer, Ru layer, oxide layer, and air region, respectively. The oxide layer is a complex mixture consisting of metallic Cr, Cr_2O_3, and CrO. We define $\overline{c_*} = \frac{c_*}{c_*^{ref}}$ with $* \in \{Cr, Ru, O, Cr_2O_3, CrO\}$, and c_*^{ref} denotes a concentration of species $*$, which is generally considered to be the saturation concentration of species $*$.

The interfacial energy density signifies the diffuse interface in phase-field model [168, 169], expressed as:

$$f_{\text{int}} = \sum_{i}^{n=4}\left(\frac{K_i}{2}\left|\nabla \eta_i\right|^2\right) \tag{3.10}$$

where K_i is the scale factor for the interfacial energy density, which can be determined by $K_i = \sigma_i \delta_i$ [170], where σ_i is the surface energy for the solid phase η_i and δ_i is the interface width for the solid phase p_i.

The chemical potential energy density can be identified as follows:

$$f_{chem}=\sum_{i}^{n=4}\left(H_i\eta_i^2\left(1-\eta_i\right)^2\right)+c_{Cr}\left(\mu_{Cr}^0-RT\right)+c_{Cr}RT\ln\left(\overline{c_{Cr}}\right)+c_O\left(\mu_O^0-RT\right)$$
$$+c_ORT\ln\left(\overline{c_O}\right)+c_{Cr_2O_3}\left(\mu_{Cr_2O_3}^0-RT\right)+c_{Cr_2O_3}RT\ln\left(\overline{c_{Cr_2O_3}}\right)+c_{Ru}\mu_{Ru}^0 \quad (3.11)$$

where the first term is the well-known double-well function to ensure the existence stability for the phase. H_i is the height of the energy barrier for each phase, which can be determined as $H_i=18\gamma_i/\delta_i$ [170]. The other terms are the chemical potential energy density for the solid-state material and the dilute material in the discharge process with R denoting the molar gas constant, T the temperature, and μ_*^0 the standard chemical potential.

According to Equation (3.6), the chemical reaction rate *r* can be defined as

$$r=\frac{\partial c_{Cr_2O_3}}{\partial t}=c_{Cr_2O_3}^{ref}\frac{\partial\eta_3}{\partial t} \quad (3.12)$$

Chemical reaction is a kinetic process containing both forward and backward reactions. Furthermore, the reaction rate given by Eq. (3.6) is a net reaction rate with forward reaction and backward reactions taking place simultaneously, which can be expressed as: $r=r_{1\to2}-r_{2\to1}=k_0\left(\exp\left(-\frac{\left(\mu_{TS}^{ex}-\mu_1\right)}{RT}\right)-\exp\left(-\frac{\left(\mu_{TS}^{ex}-\mu_2\right)}{RT}\right)\right)$ (3.13)

where $r_{1\to2}$ and $r_{2\to1}$ are the forward reaction and backward reaction for discharge, respectively; μ_{TS}^{ex}, μ_1, and μ_2 are the excessive chemical potential for the transition, initial, and final states, respectively, k_0 is the rate coefficient.

The excessive chemical potentials can be determined by the functional derivatives of Helmholtz free energy with respect to the corresponding concentration:

$$\mu_1^{ex} = 2\frac{\delta F}{\delta c_{Cr}} + 3\frac{\delta F}{\delta c_O} = RT\ln\left(\overline{c_{Cr}}^2\right) + 2\mu_{Cr}^0 + RT\ln\left(\overline{c_O}^3\right) + 3\mu_O^0 \tag{3.14}$$

$$\mu_2^{ex} = \frac{\delta F}{\delta c_{Cr_2O_3}} = RT\ln\left(\overline{c_{Cr_2O_3}}\right) + \mu_{Cr_2O_3}^0 \tag{3.15}$$

The transition electrochemical potential can be expressed as a composition of the excessive electrochemical potential for the initial state μ_1^{ex} and the final state μ_2^{ex} with the asymmetry parameter α:

$$\mu_{TS} = \alpha\mu_1^{ex} + (1-\alpha)\mu_2^{ex} + RT\ln(a_{TS}) \tag{3.16}$$

where a_{TS} is the activity for the transition state.

In the oxide layer, Cr_2O_3, the supply of oxygen atoms can be considered sufficient. Thus, we can set $\overline{c_O}$ = 1 and $\overline{c_{Cr_2O_3}}$ = 1, and we obtain

$$r = \frac{k_0}{a_{TS}}\left(\left(\overline{c_{Cr}}^2\right)e^{\frac{(1-\alpha)\left(2\mu_{Cr}^0+3\mu_O^0-\mu_{Cr_2O_3}^0\right)}{RT}} - e^{-\frac{\alpha\left(2\mu_{Cr}^0+3\mu_O^0-\mu_{Cr_2O_3}^0\right)}{RT}}\right) \tag{3.17}$$

According to the multiphase phase field method [171] and Eq. (3.13), the Allen-Cahn equation for the order parameters $\boldsymbol{\eta}$ can be expressed as follow:

$$\frac{\partial\eta_1}{\partial t} = \sum_{j=2}^{n=4}\left(L_j\frac{\delta F}{\delta\eta_j} - L_1\frac{\delta F}{\delta\eta_1}\right) \tag{3.18}$$

$$\frac{\partial\eta_2}{\partial t} = \sum_{j=1,j\neq 2}^{n=4}\left(L_j\frac{\delta F}{\delta\eta_j} - L_2\frac{\delta F}{\delta\eta_2}\right) \tag{3.19}$$

$$\frac{\partial\eta_3}{\partial t} = \sum_{j=1,j\neq 3}^{n=4}\left(L_j\frac{\delta F}{\delta\eta_j} - L_3\frac{\delta F}{\delta\eta_3}\right) - h_{34}\frac{r}{c_{Cr_2O_3}^{ref}} \tag{3.20}$$

where L_j is the coefficient to scale the contributions of the interfacial energy to the phase migration for phase, $h_{34} = \frac{4p_3p_4}{\sum_i p_i^2}$ [169, 172], which means the reaction occurs in the interface of phase p_3 and p_4.

The concentration of Cr and oxygen can be described by the Fick's law:

$$\frac{\partial c_{Cr}}{\partial t} = D_{Cr}^{tot}\nabla^2 c_{Cr} - k_1 c_{Cr}^{ref}\frac{\partial \eta_3}{\partial t} \tag{3.21}$$

$$\frac{\partial c_O}{\partial t} = D_O^{tot}\nabla^2 c_O - 2c_o^{ref}\frac{\partial \eta_3}{\partial t} \tag{3.22}$$

with

$D_{Cr}^{tot} = h(\eta_1)D_{Cr}^{\eta_1} + h(\eta_2)D_{Cr}^{\eta_2} + h(\eta_3)D_{Cr}^{\eta_3}$,

$D_O^{tot} = h(\eta_1)D_O^{\eta_1} + h(\eta_2)D_O^{\eta_2} + h(\eta_3)D_O^{\eta_3} + h(\eta_4)D_O^{\eta_4}$,

$h(x) = x^3(10 - 15x + 6x^2)$.

In the above equation D_a^b represents the diffusion coefficient of species *a* in the region *b*. k_1 is a scaling coefficient, which is used if the oxide layer is a mixture of different oxides (i.e., Cr_xO_y). The consumption of Cr depends on the thickness of Ru and this phenomenon will be discussed in Chapter 5 (Section 5.3). Table 3.2 lists the parameters and their corresponding values that were employed in simulations.

Table 3.2 Parameters used in the simulations.

R , ideal gas constant	8.314 J/mol
T , absolute temperature	1023 K
$D_{Cr}^{\eta_1}$, diffusion coefficient for Cr in Cr layer	7.5×10^{-12} cm^2/s
$D_{Cr}^{\eta_2}$, diffusion coefficient for Cr in Ru layer	5×10^{-14} cm^2/s
$D_{Cr}^{\eta_3}$, diffusion coefficient for Cr in the oxide layer	4×10^{-13} cm^2/s[173, 174]
$D_{O}^{\eta_1}$, diffusion coefficient for oxygen in Cr layer	7×10^{-16} cm^2/s
$D_{O}^{\eta_2}$, diffusion coefficient for oxygen in Ru layer	1×10^{-16} cm^2/s
$D_{O}^{\eta_3}$, diffusion coefficient for oxygen in oxide layer	8.4×10^{-14} cm^2/s[175]
$D_{O}^{\eta_4}$, diffusion coefficient for oxygen in air	5×10^{-12} cm^2/s
L_i , coefficients to scale the contributions of the interfacial energy	3.42×10^{-13} m•s/kg
L_k , coefficients to scale the contributions of the kinetics	1×10^{-5} 1/s
α , asymmetry factor	0.5
γ_i , interfacial energy density	2.5 J/m^2[176, 177]
δ_i , interfacial thickness	40 nm
$c_{Cr_2O_3}^{ref}$, reference concentration for Cr_2O_3	34344 mol/m^3
c_{Cr}^{ref} , reference concentration for Cr metal	137500 mol/m^3

Chapter 4: Microstructural analysis of Ru–Pt anti-stick coatings

In this chapter, a multilayer Ru–Pt coating with titanium (Ti) interlayer was developed on graphite substrates by the magnetron sputtering technique. The anti-sticking performance of the coating was evaluated by annealing the coated samples with an ASG coverage. The as-deposited and annealed samples at 750 °C for 2, 20, and 40 h were designated as AD, 750-2h, 750-20h, and 750-40h, respectively. In addition, phase stability, microstructural evolution, and mechanical properties of the Ru–Pt multilayer coatings were examined. Based on these characterizations, the enhancement in mechanical and anti-sticking performances, in comparison with those of monolayer (Ru or Pt) coatings, were explained.

4.1 Results and discussion

4.1.1 Phase identification

Fig. 4.1(a) shows the photographs of the coatings in the as-deposited and annealed states. Visually, the annealed coatings (750-20h and 750-40h) remained almost identical to the as-deposited one (i.e., no delamination, color change, or surface contamination), and the glass pieces used as the coverage in annealing remained fully transparent. Fig. 4.1(b) shows the XRD patterns of the substrate and the Ru–Pt coated samples before and after annealing. These patterns exhibit a similar set of peaks before and after annealing, indicated by the reflections of Ru (HCP), Pt (FCC), Ti (HCP), and graphite substrates. In the as-deposited coatings, the primary diffraction peaks of Pt and Ru located at 39.7° and 42.2° correspond to the preferred orientation of the

(111) and (002) planes, respectively. After 2 h of annealing at 750 °C, the annealed coatings maintained the stable structure of the Pt and Ru phases except that the diffraction peak of Pt (111) slightly shifted towards the higher angles corresponding to a lattice expansion. Such a result is similar to those reported in ref. [178, 179], and it is likely due to a decrease in compressive residual stress. With continuous annealing for 20 and 40 h, the Pt (111) diffraction peak became narrower and more intensified but no longer shifted, whereas the Ru (002) weak peak shifted slightly towards lower angles. The Pt (111) and Ru (002) peaks can be utilized to estimate the average crystallite sizes. The crystallite sizes of the Pt and Ru in the as-deposited and annealed state were calculated using Scherrer's equation [180],

$$D = \frac{k\lambda}{\beta \mathrm{Cos}\theta} \qquad (4.1)$$

where D is the average crystallite size, k is a constant (0.94), λ is the x-ray wavelength (1.54 Å for CuKα), θ is the Bragg angle pertaining to a peak, and β is the full width at half maxima (FWHM). Thus, the crystallite size was calculated to be 9.7 and 16.9 nm for Pt and Ru in the as-deposited state, respectively, and 17.2 and 8.2 nm for Pt and Ru in the 40 h annealed state, respectively. It is noted that the Pt crystallite size increased after annealing, whereas, for Ru, annealing led to a decrease in crystallite size, indicating grain refinement. This grain refinement can be ascribed to the twinning-induced grain subdivision, which will be exhibited by TEM results.

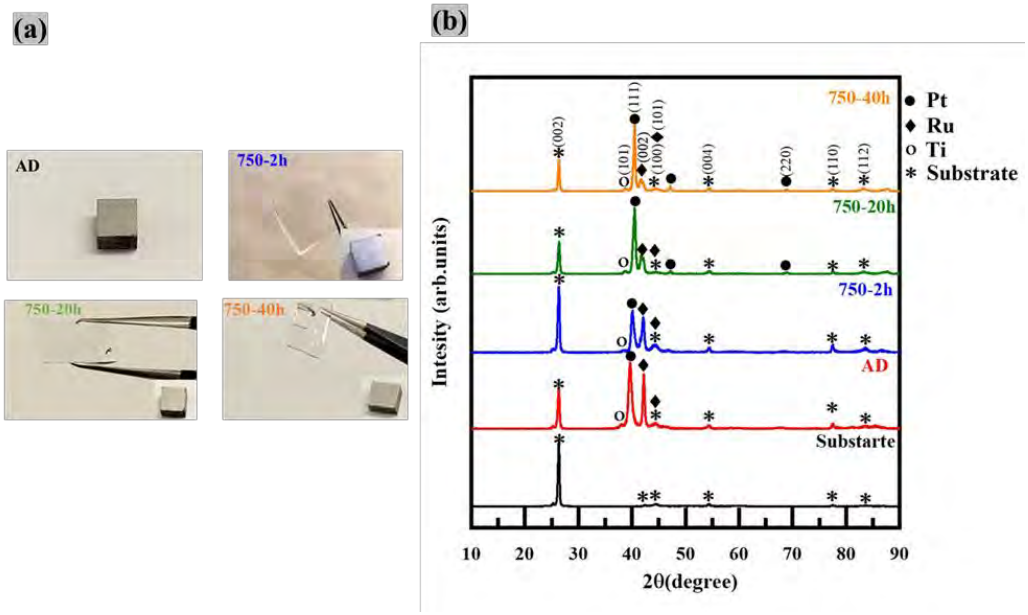

Figure 4.1 Coated and annealed samples: (a) photographs of as-deposited (AD), 750-2h, 750-20h and 750-40h annealed coated samples with their covering glass pieces and (b) XRD patterns of the substrate and of Ru–Pt multilayer coatings (AD, 750-2h,750-20h,750-40h).

4.1.2 Surface morphology and roughness studies

Surface morphologies of Ru–Pt multilayer coatings evaluated by SEM are exhibited in Fig. 4.2. It can be observed that the DC sputtering resulted in a continuous, dense, and coarse surface morphology (Fig. 4.22(a)). The associated EDS analyses showed reflections of Ru and Pt. As the sampling depth of EDS is in the micrometers range [181], larger than the overall coating thickness, reflections of carbon from the substrate were also recorded, as depicted in Fig. 4.2(b). As can be observed, the Pt and Ru grains became slightly more spherical after prolonged annealing (Fig. 4.2(e, g)). No surface cracks were observed on the multilayer-coated samples.

The surface morphologies of the 840 nm monolayer Ru and Pt coated samples before and after 2 h of annealing at 750 °C are exhibited in Fig. 4.3. A few micro-

cracks on the Pt surface without annealing were observed (Fig. 4.3(a)). After 2 h of annealing with glass coverage, the cracks became much more significant in the Pt coated surface (Fig. (4.3b)). This could possibly be owing to the lattice mismatch between Ti/Pt and the graphite substrate, which resulted in the coating deterioration and, therefore, slight glass adhesion or chemical reaction between glass/coating. The inset in Fig. 4.3(a) shows a schematic of the heteroepitaxial interface: Ti {101} || Pt {111}, which are determined based on the corresponding XRD pattern. Note that when Ti is deposited on graphite, it has FCC structure owing to the formation of TiC [182]. The crystal lattice mismatch leads to changes in the lattice constants, which can be manifested by the XRD peak shift (0.53° for Pt {111} and −0.41° for Ti {101}). The mismatch results in the accumulation of strain energy, causing irreversible deformation and defects, such as pores and cracks, in the monolayer coating. During deposition, cracks have already propagated to the Pt surface as shown in Fig. 4.3(a). After the short-term annealing, the cracks became more significant, as shown in Fig. 4.3(b). For the Ru monolayer coating, no glass adhesion was observed, and a fairly smooth surface was exhibited after 2 h of annealing (Fig. 4.3(d)). Owing to the inherent brittleness of Ru, a few micro-cracks appeared after 2 h of annealing.

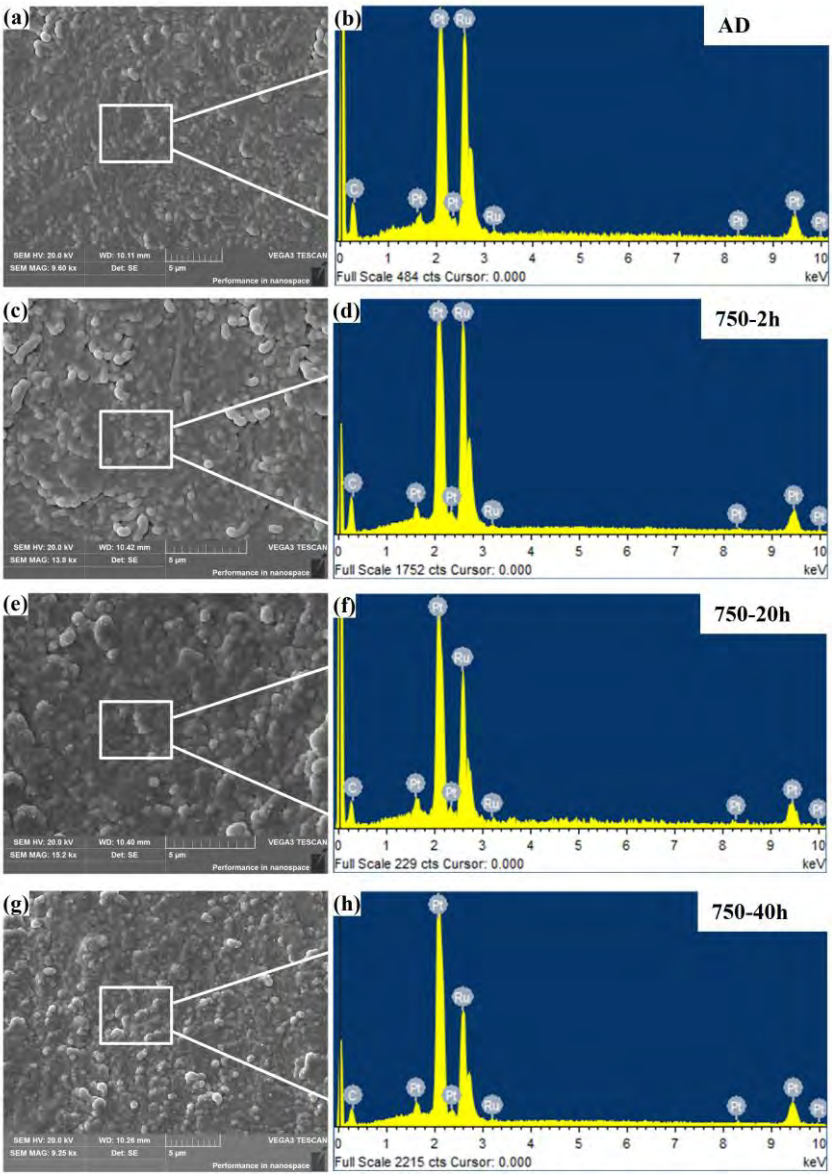

Figure 4.2 SEM surface morphology and corresponding EDS spectrum of marked areas in SEM images of (a, b) AD, (c, d) 750-2h, (e, f) 750-20h, and (g, h) 750-40h samples.

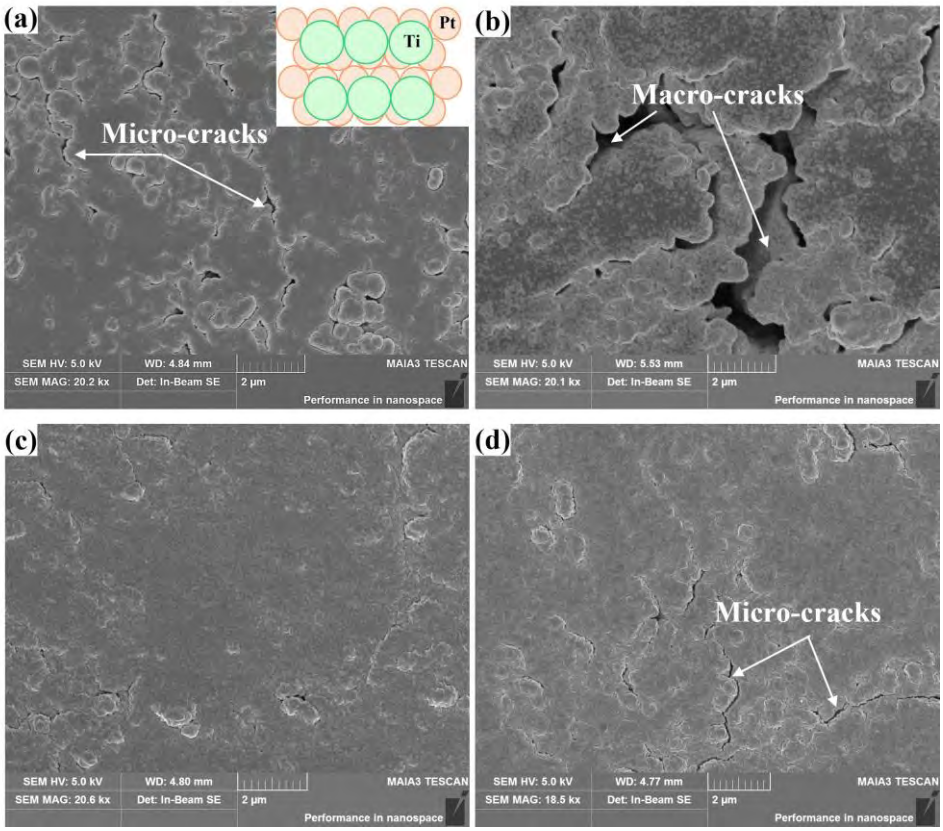

Figure 4.3 Surface morphology of (a, b) Pt and (c, d) Ru monolayers in the (a, c) AD and (b, d) annealed states.

In contrast to Ru and Pt monolayers, better surface quality and anti-sticking properties were exhibited by the Ru–Pt multilayer structure, which could be ascribed to the interfaces that inhibit the atomic diffusion on both sides (glass and substrate) [102]. In addition, the thin and ductile Pt layers prevent the cracking of Ru during annealing. Fig. 4.4(a–d) displays SEM images of the top surfaces of Ru–Pt multilayer coatings before and after annealing. These coated samples exhibited very smooth and uniform surfaces even after 40 h of annealing. The average particle size of the coatings was calculated from the SEM images by selecting isolated particles using the Image J software. In Fig. 4.4(e–h), the histogram reveals the particle size distribution of the as-deposited and heat-treated multilayer coatings. The average particle sizes of AD, 750-2h, 750-20h, and 750-40h samples were 0.35, 0.36, 0.36, and 0.39 µm,

respectively. The statistical results of Ru–Pt multilayer coatings are summarized in Fig. 4.4(e–h) and Table 4.1. As can be observed, the particles become slightly coarsened after annealing for a long time, but the increase in surface particle size is insignificant. It is noted that the average surface particle size is larger than the average grain size determined from XRD patterns. The reason is that the surface particles may be agglomerations of grains with different orientations, which form spherical shapes to minimize the surface/interface energy.

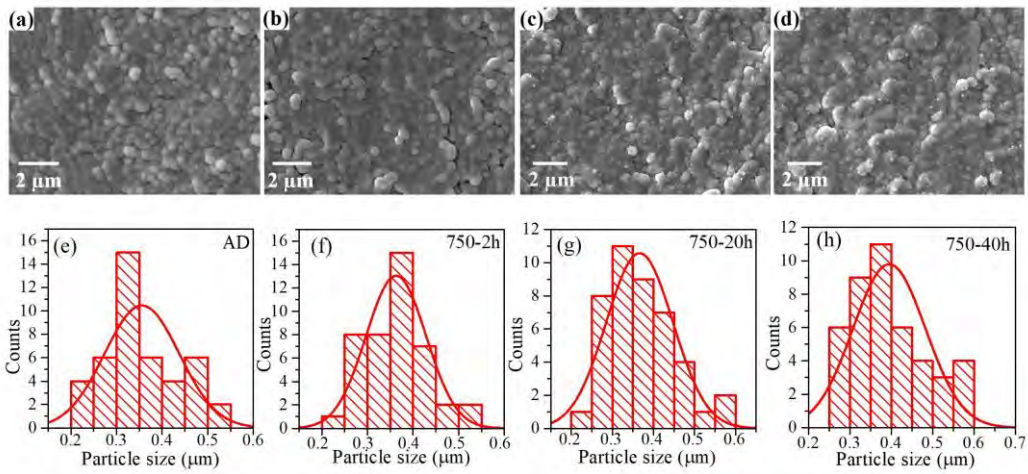

Figure 4.4 SEM images and particle size distribution of as-deposited and annealed coated samples: (a, e) AD, (b, f) 750-2h, (c, g) 750-20h, and (d, h) 750-40h.

Table 4.1 Particle size distribution and average particle size of the Ru–Pt multilayer coatings

Sample ID	Particle Size distribution (μm)	Average size (μm)
AD	0.22–0.52	0.35
750-2h	0.23–0.51	0.36
750-20h	0.20–0.55	0.36
750-40h	0.27–0.59	0.39

The morphologies of the coating surfaces were further characterized using atomic force microscopy (AFM), as shown in Fig. 4.5. The scanning scale of each image was set to 1 × 1 μm^2. All of the AFM images exhibited dense and granular structure morphology with visible agglomerated grains. The AFM 3D images

confirmed the crack-free surfaces. The average surface roughness (R_a) and root mean square roughness (R_q) of the as-deposited coatings were 16.37 and 21.33 nm, respectively. For the 2, 20, and 40 h annealed samples, the R_a/R_q values were 18.86/19.11, 19.39/22.07, and 24.57/25.03 nm, respectively. Apparently, the longer annealing facilitated the coalescence of adjacent particles, as shown in Fig. 4.5, resulting in an increase in roughness [183]. It is worth noting that the annealed coatings maintained a smooth surface with a small change in roughness after heating with glass coverage. Thereby, the observation of the surface morphology evolution leads to the assertion that the Ru–Pt multilayer coatings demonstrated significant thermal stability in terms of surface characteristics at 750 °C.

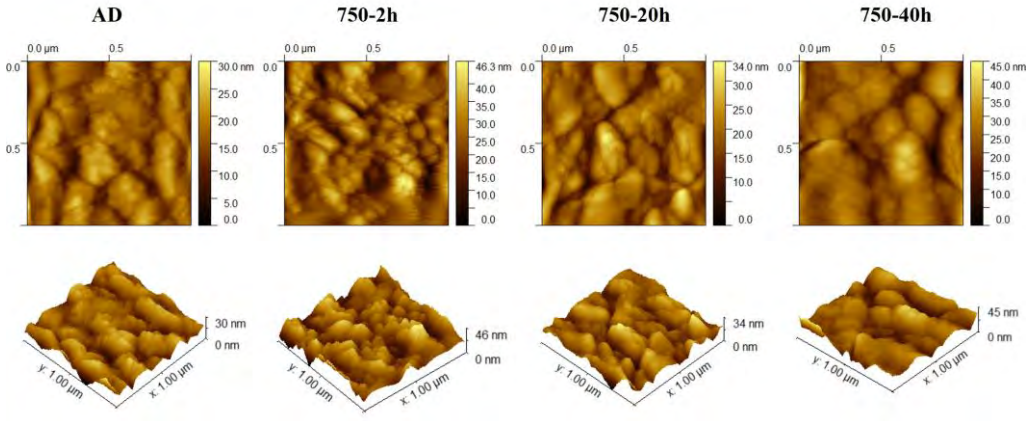

Figure 4.5 AFM surface morphology (2D, 3D) of AD, 750-2h, 750-20h, and 750-40h samples.

4.1.3 Mechanical properties and XPS analysis

Fig. 4.6 exhibits the typical curves of load versus penetration depth obtained by nanoindentation tests for the as-deposited and annealed Ru–Pt multilayer coatings. It can be observed that the maximum penetration depth was reduced for annealed coatings compared to as-deposited ones under the same load. The hardness and Young's modulus (H) and (E) were determined from the nanoindentation curves and

are reported in Table 4.2, which illustrates significant increases in *H* and *E* with annealing time. The improvement in mechanical performance is primarily due to the multilayer enhancement mechanism resulting from the dislocation blockage created by the multilayer interfaces [102].

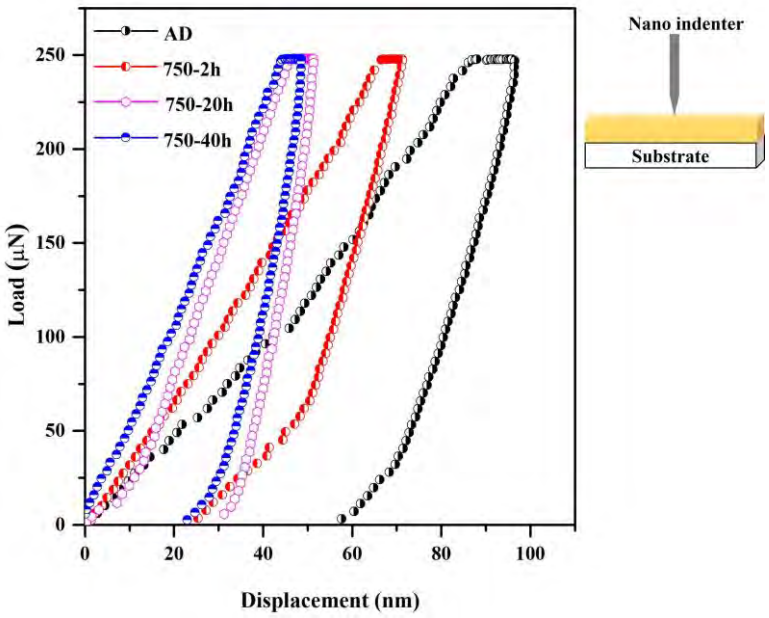

Figure 4.6 Nanoindentation (load–depth) curves of Ru–Pt multilayer coatings.

In heterostructure materials, crystallographic structures, slip plane orientations, and slip directions vary significantly across the interfaces. With lattice misfit strains, the stressed interfaces can further prevent dislocations from crossing them. This is the case in our multilayer system, wherein the Pt–Ru interfaces act as stronger barriers to dislocation motion. The interfaces were originally wavy, which allows dislocations to glide in more directions. After the brief (2 h) annealing, interfaces became flattened (see the following TEM results), which confines dislocations to move mainly in the in-plane directions. Hence, a significant increase in hardness was observed. After the long (20 and 40 h) annealing time, it was observed that the hardness further increased, which could be attributed to the effect of solid-solution hardening caused by the

interdiffusion of Pt and Ru to form their alloys. In addition, we did not observe a significant increase in grain size after the long-term annealing, probably caused by the constraint of the layered structure; hence, the softening caused by grain growth was insignificant.

Table 4.2 Mechanical properties (*H*) and (*E*) of Ru–Pt multilayer coatings

Sample ID	***H* (GPa)**	***E* (GPa)**
AD	1.14	18.99
750-2h	2.06	28.52
750-20h	3.15	59.48
750-40h	3.61	59.50

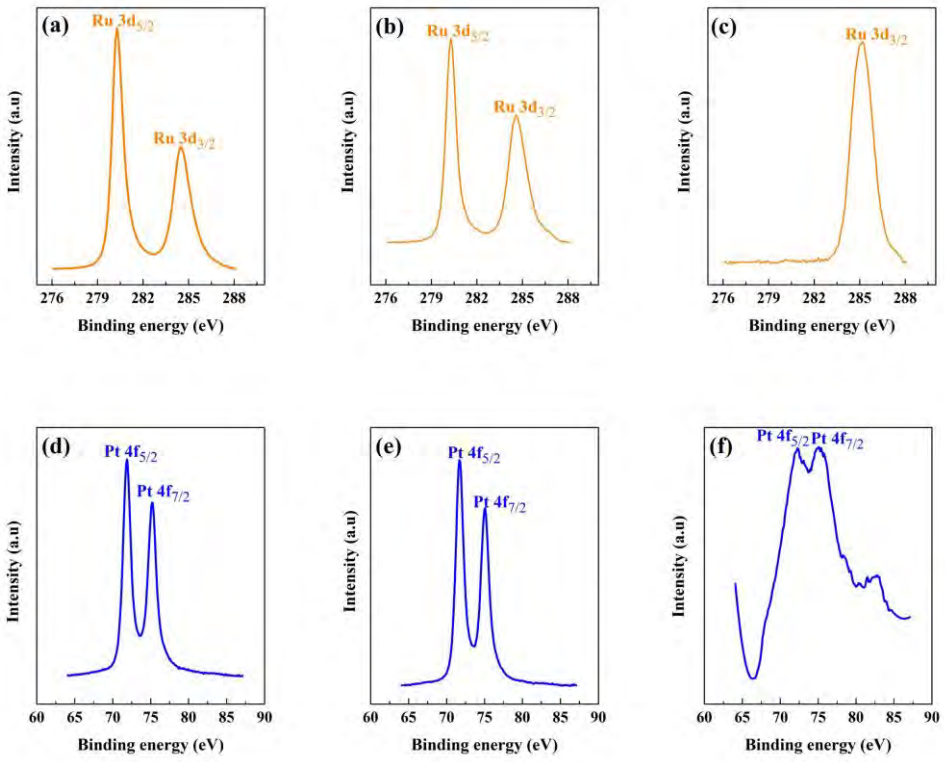

Figure 4.7 XPS spectra of (a, b, c) Ru 3d and (d, e, f) Pt 4f; (a, d) 750-2h, (b, e) 750-20h, and (c, f) 750-40h samples.

The investigation of the surface chemical states was carried out using XPS. Fig. 4.7 (a, b, c) depicts the Ru 3d XPS spectra in the annealed states. After 2 h of annealing, the Ru 3d spectra exhibited a doublet of Ru $3d_{5/2}$ and Ru $3d_{3/2}$ with binding energies of 280.3 and 284.3 eV, respectively, which are in line with the reported values for pure metallic Ru [184]. After longer annealing, no noticeable change in the binding energies was observed for the Ru 3d doublet, indicating that the Ru sustained its metallic state. However, for the 750-40h sample, the Ru 3d spectra recorded only one peak of Ru ($Ru3d_{3/2}$ = 285.1 eV), which overlapped with the same energy region of C (C1s = 285.1 eV) [184]. Therefore, this peak could correspond to elemental carbon (C–C) bonds [185, 186]. Fig. 4.7(d) exhibits the two characteristic peaks of metallic Pt (Pt $4f_{5/2}$ = 71.8 eV) and (Pt $4f_{7/2}$ = 75.2), which are in accordance with the reported values [187, 188]. Furthermore, after 40 h of annealing (Fig. 4.7(f)), the binding energy of Pt 4f shifted negatively by approximately 0.3–0.4 eV, revealing the occurrence of charge transfer from Ru to Pt (owing to the higher electronegativity of Pt), which indicates the interaction of Pt and Ru [189].

4.1.4 Microstructural evolution

Fig. 4.8 shows the typical TEM image of the cross-section of the as-deposited multilayer coatings. A homogeneous and dense cross-sectional morphology with a uniform nano-laminated structure can be observed. In Fig. 4.8, the alternating Ru and Pt layers, the Ti interlayer, and the graphite substrate can be clearly discerned. The sputtering process led to the pseudo columnar structure perpendicular to the substrate surface [190]. The dome-shaped columns resulted in the wavy structure of the nano-crystalline coating layers. Additionally, the internal stresses (due to lattice mismatch or thermal effect) developed during the deposition could also induce waviness [191].

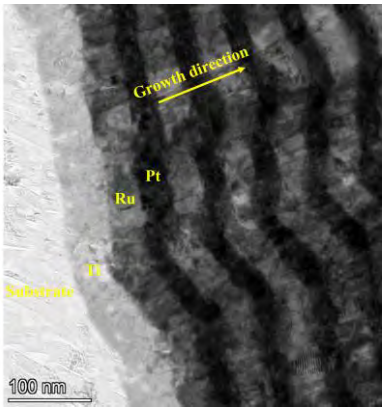

Figure 4.8 Typical cross-sectional TEM image of the as-deposited multilayer coatings.

To obtain the structural insight, HRTEM was conducted at the interfacial area of Ru–Pt. Fig. 4.9(a) depicts the HRTEM image of the as-deposited multilayer coatings with an inset showing the corresponding SAED pattern. The cross-sectional HRTEM image exhibited a dense microstructure with no porosity, and a multi-ring pattern was observed in the SAED, confirming the nano-crystalline phases. The inverse fast Fourier transform (IFFT) image of the as-deposited coatings is shown in Fig. 4.9(b). It is evident that the lattice distortion occurred at the interface owing to the dissimilar crystal lattice of Ru (HCP) and Pt (FCC). The misfit dislocations were recognized clearly and marked by the symbol “T” in the IFFT image. The wavy structure in the as-deposited state indicates the existence of compressive residual stresses. In the IFFT-TEM image, we observed dislocations formed at the interface. Furthermore, owing to the lattice mismatch between the two layers, coherency strains and lattice distortion are also generated, and the blockage of dislocation at the interfaces eventually results in mechanical strengthening and impediment of atomic diffusion [102, 192].

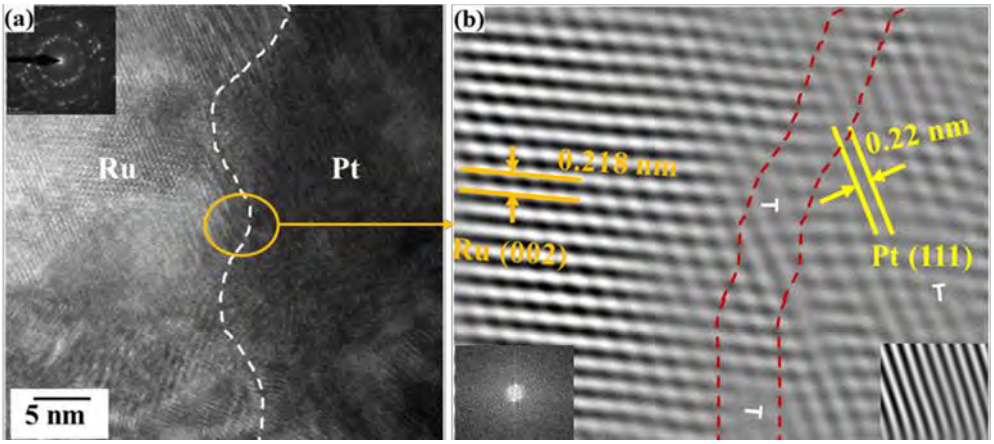

Figure 4.9 As-deposited Ru–Pt multilayer coating images of (a) HRTEM image, and (b) inverse fast Fourier transform (IFFT).

Fig. 4.10 shows the cross-sectional HRTEM images of 2 h annealed coatings. It is noted that the coated layers maintained a laminated structure after the annealing, and the waviness of the interfaces was slightly mitigated during the annealing process (Fig. 4.10(a)). No amorphous phase was observed at the interface. In the multilayer coating, restriction of dislocation movement in a strained interface results in a significant hardness enhancement. The high-temperature (750 °C) annealing leads to a stronger such effect because of the reduction in dislocation density and thus the increase in misfit strains. The dislocation movement is impeded by the coherency [193], as it is relatively more difficult for dislocation to pass through a strained lattice than an unstrained one. In the multilayer structure, the interfaces already restrict the movement of dislocations; the coherency strains further contribute to the hardness enhancement by making dislocations difficult to glide. Hence, we observed an increase in the nano-hardness in the nanoindentation experiments. Fig. 4.10(d) shows the SAED pattern taken from an area enclosing the Pt–Ru interface as indicated in Fig. 4.10(a). The spots in the SAED pattern confirm the nanocrystalline nature of the multilayered coatings. In addition, it is observed that after the short-term annealing,

the multi-ring pattern (inset of Fig. 4.9(a)) is transformed into a pattern with many spots, which can be ascribed to the change in grain sizes [194] and grain orientations. The latter could be associated with the flattened interfaces after the brief annealing.

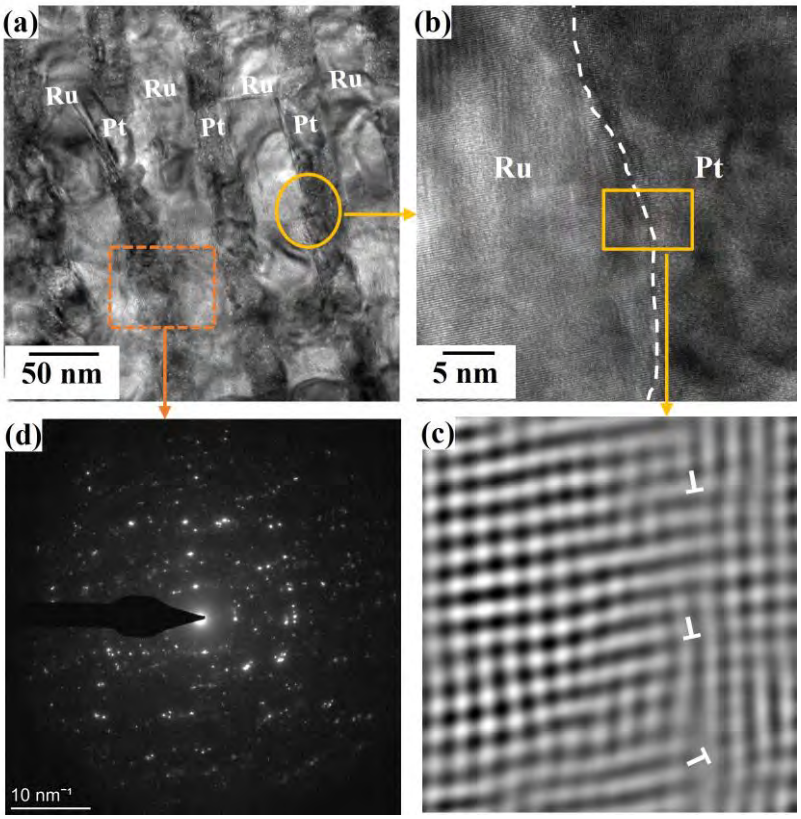

Figure 4.10 HRTEM images and SAED patterns of annealed (750-2h) coatings: (a) cross-section, (b) Ru–Pt interfacial area marked in (a), (c) IFFT image of (b), (d) SAED pattern of marked area in (a).

Fig. 4.11 shows the high angle annular dark-field (HAADF) image and the EDS mapping acquired in the STEM mode. In HAADF-STEM, the dark gray and bright gray areas correspond to Ru and Pt (opposite to those in the HRTEM image) as confirmed by EDS mapping. In Fig. 4.11(b), the elemental mapping image, a layered structure can be clearly observed. Fig. 4.11(d) confirms that the annealed coatings (sample 750-2h) sustained the multilayer structure, which indicates the thermal stability of the multilayer noble metal coatings after annealing at 750 °C for 2 h.

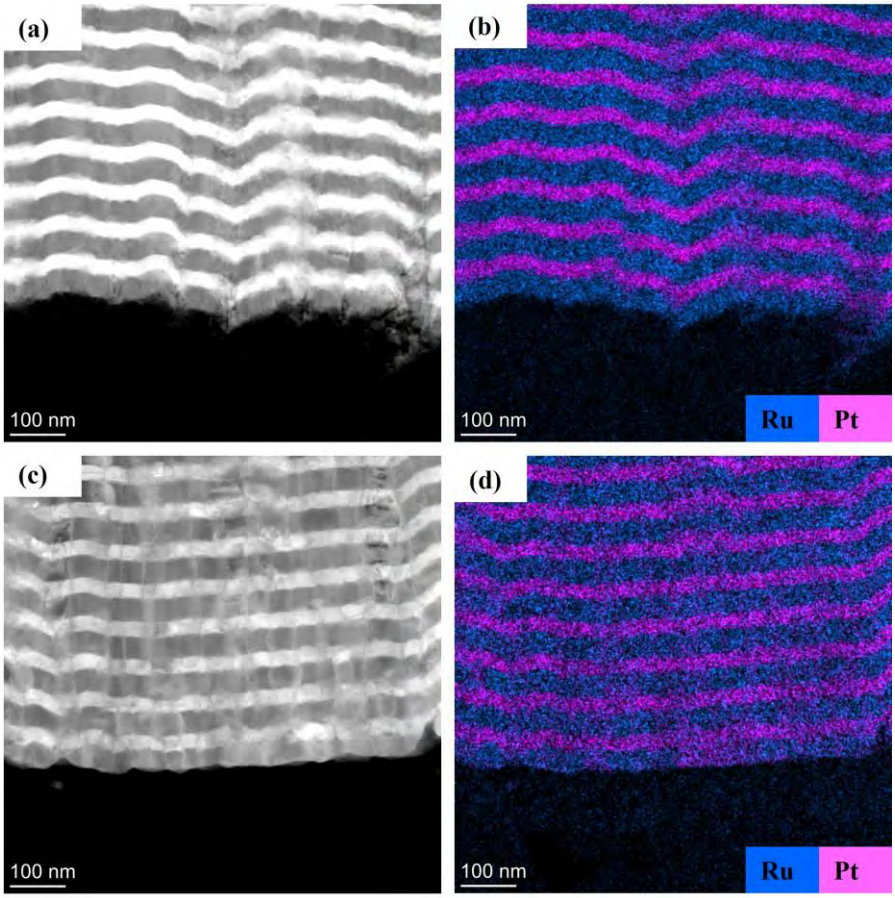

Figure 4.11 HAADF-STEM images and EDS mappings. (a, b) cross-section of sample AD and (c, d) cross-section of sample 750-2h.

Figs. 4.9–4.11 illustrate the wavy interfaces in the as-deposited coatings and the reduction in waviness after a brief annealing. It is conceived that the wavy interface is caused by residual stresses in the as-deposited thin films. However, the residual stresses were not measured because of the difficulty to determine them in the nanolayers. Hence, let us explain their possible causes here. The primary contributions of residual stress in the thin films are intrinsic and thermal stresses arising from the mismatches in the crystal structures and CTEs, respectively. The intrinsic stresses, i.e., those arisen from lattice misfit, are straightforward as the crystal structures across interfaces are disparate. The thermal stresses could be caused by the high kinetic energy of sputtered particles. They induce local heating and hence, a thermal effect.

In addition, during deposition, residual stresses may also be caused by the effect of implantation (e.g., Ru atoms are squeezed into the Pt lattice). All these effects can be mitigated through the dislocation motion and diffusion that occur during annealing. In particular, dislocation motion within nanolayers can be explained based on the confined layer slip (CLS) mechanism [195-198].

Based on the CLS mechanism, the lack of space for dislocation pile-up in a submicron or nanolayer, it is difficult for the dislocations to cross an interface, and they can only glide within a thin layer by bowing between the interfaces, which leaves misfit dislocations behind. The interaction of misfit dislocations with passing dislocations induces rise in flow stress and strain hardening. When the thickness of the layers is in nanometers, such a confinement effect becomes very significant, i.e., the dislocations are unable to bow. In this case, dislocation glide across the interface becomes the key mechanism in determining the strength. The higher the disparity in crystallographic structure across an interface, the higher is the barrier to dislocation transmission. With high interfacial barriers, the gliding dislocations are absorbed in the interfaces by forming dislocated structures (i.e., dislocation cores) spreading along the interface plane. With this spreading process, the resistance to dislocation gliding becomes stronger and the hardness increases after brief annealing.

Among the different crystalline structures, HCP metals are very likely to have twins upon straining owing to the lack of sufficient slip systems for an arbitrary change in shape [199]. Twinning results in the shearing of specific crystallographic planes, forcing the atoms to relocate into an arrangement with a different orientation from the parent crystal. In the as-deposited coatings, twinning was not observed in the HRTEM results (i.e., no growth twins); however, annealing twins were observed, as

exhibited in Fig. 4.12 (a), in the annealed sample 750-40h. This can explain the grain refinement in Ru layers as revealed by XRD analysis. IFFT image of the marked area in HRTEM image (4.12(a)) is exhibited in 4.12(b). Twinning plane can be observed which interacts with dislocation movements. In addition, annealing twins contribute to the increase in hardness with annealing time because twin boundaries (TBs) efficaciously impede mobile dislocations [199].

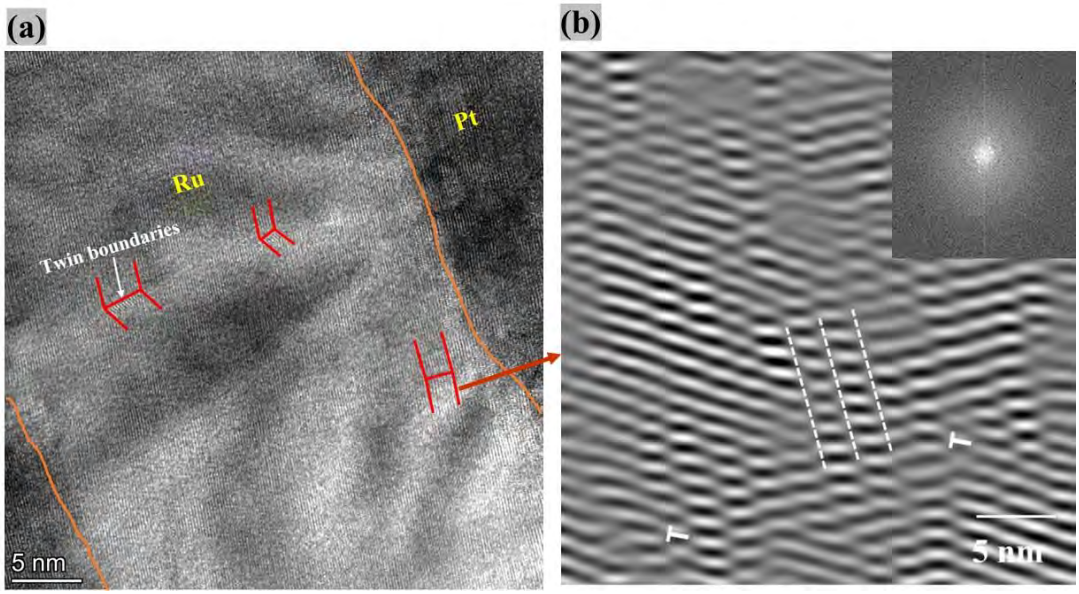

Figure 4.12 (a) HRTEM image of the annealed coated sample 750-40h (b) IFFT image with inset FFT image

The HAADF-STEM image and EDS mappings (Pt, Ru, Ti, C) of a FIB lamella as cut for sample 750-40h are exhibited in Fig. 4.13. At the top of the FIB sample, Pt protection layers were deposited to protect the free surface. As the damage caused by direct ion-beam Pt deposition could make the analysis of microscopic features difficult, a two-step Pt deposition approach [200], i.e., electron-beam deposition followed by ion-beam deposition, was adopted to avoid the damage. It can be observed that at some areas in the Ru–Pt multilayer coatings, the elemental Pt layers overlapped with Ru layers indicating the occurrence of diffusion owing to the

thermally activated motion of Pt atoms, thus forming an Ru–Pt solid solution. The Ru layers (Fig. 4.13(c)) demonstrated thermal stability even after 40 h of annealing. It is worth noting that titanium did not diffuse out, as it was restricted by the multilayer coating structure. It suggests the improved adherence of Ti with both the multilayer coatings and substrate. However, it is evident that after long-term annealing at 750 °C, carbon atoms from the substrate diffuse into the coating structure, which may lead to severe lattice distortion and embrittlement. This is evidenced by the crack extending from the top surface to the substrate, as shown in Fig. 4.13(a). The EDS mapping of C indicates that carbon atoms diffused out and likely formed a thin layer on the coating surface. In Fig. 4.13(b), the concentration of Pt in the electron-beam layer appeared to be lower than that in the top ion-beam deposited layer, which is caused by the interaction of carbon (layer) with the electron-beam deposited Pt.

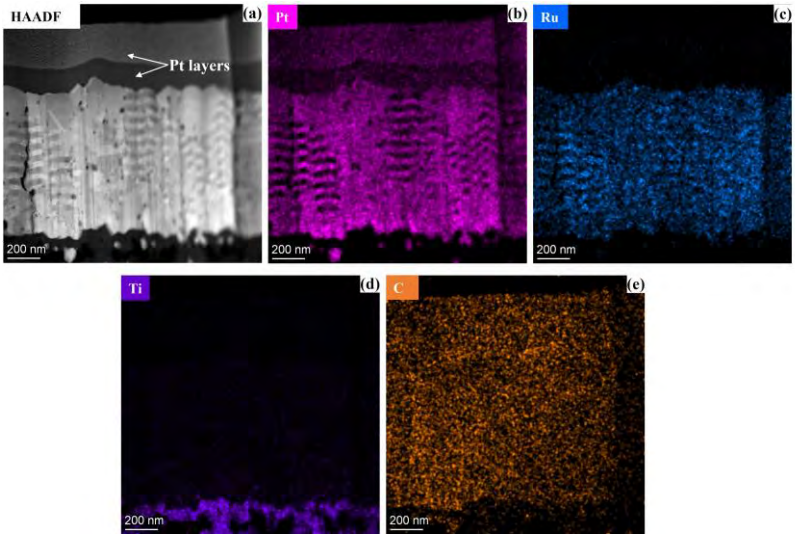

Figure 4.13 Annealed coated sample (750-40h); (a) HAADF-STEM image and EDS mappings of (b) Pt, (c) Ru, (d) Ti, and (e) C.

Fig. 4.14 shows the HRTEM image and SAED pattern of the annealed 750-40 h coatings. In Fig. 4.14(a), both layered and inter-diffused regions can be observed,

which indicates the disappearance of the multilayer structure after the long annealing. The HRTEM image in Fig. 4.14(b) shows a magnified inter-diffused region, wherein the SAED pattern of the marked area is further exhibited in Fig. 4.14(c). The SAED pattern contains many bright and weak spots, indicating multiple sets of crystal lattices. It is noted that the pattern is similar to those taken from FCC/HCP interfaces (see, e.g., [201]). Because the layered structure has vanished in Fig. 4.14(b), the SAED pattern shown in Fig. 4.14(c) indicates the mixture of Pt-rich (FCC) and Ru-rich (HCP) alloys owing to their interdiffusion.

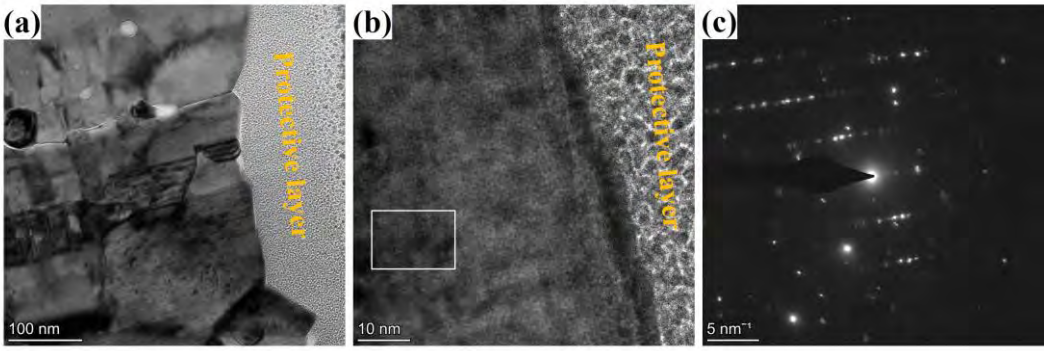

Figure 4.14 Cross-section of 750-40h sample; (a) TEM image, (b) HRTEM image, and (c) SAED pattern of the marked area in (b).

4.1.5 Cyclic glass molding experiments

The performance of the Ru–Pt coated graphite samples was further evaluated using an industrial glass molding system. Unlike laboratory experiments, the production experiments were not performed with precisely controlled process parameters. For example, an N_2 flow was maintained to ensure an approximately inert atmosphere; however, the flow rate was not measured. The temperature measurement was based on thermocouples in the heating plates contacting the molding tools; however, the measured temperature may be different from that of glass.

Fig. 4.15 presents a schematic of the industrial testing setup and a complete cycle of the molding process. A molding cycle consists of three stages: heating, pressing (molding), and cooling. In the machine, these stages were further divided into several substages. For the ASG (Corning Gorilla Glass 5) used in the test, the tool temperature in the pressing stage was 780 °C for 700 s and 700 °C for 350 s. The pressing force was ramped up to approximately 150 N for 350 s, then, 600 N for 100 s and 1850 N for 250 s at 780 °C, and maintained at 1850 N for 350 s at 700 °C. The entire molding process for one cycle took 70 min. Upon completion of one cycle, the glass piece was removed manually, and a new glass blank was inserted for the next molding round.

Fig. 4.16(a, b) depicts the Ru–Pt coated industrial samples (graphite substrate) before and after the molding experiments. The surface of the coated sample in the as-deposited state was rough (Ra ~100 nm), with a few scratches, because the graphite substrate was only manually ground using sandpapers (the finest one used was 6000 grit). The coated sample was subjected to tens of molding cycles in the actual production environment. After 40 molding cycles, the coated sample was examined, and it was revealed that Ru–Pt coatings withstood pressing without any coating degradation. Even though the surfaces of the coated industrial samples were rougher than those of the laboratory ones, no macroscopic surface defect was identified after continued molding cycles. This means that the coated graphite molds for ASG glass can have a long service life in a harsh working environment. The glass piece after the 40^{th} molding cycle is shown in Fig. 4.16(c), demonstrating the high anti-sticking behavior of the Ru–Pt coatings with the glass. Slight particle adherence can be detected on the surface of the glass piece, which is attributed to the environmental contamination (because graphite powders were everywhere in the machine) of the

testing facility. The industrial results are consistent with the in-house performance of the multilayer coatings, suggesting that Ru–Pt multilayer coatings are a strong candidate for glass molding dies, particularly for glasses with high T_g. It should be noted that we did not suggest longer usage of the coatings because of the crack found in the 750-40h sample (Fig. 4.13(a)). In the industrial test, after performing the molding for more than 40 cycles, delamination started.

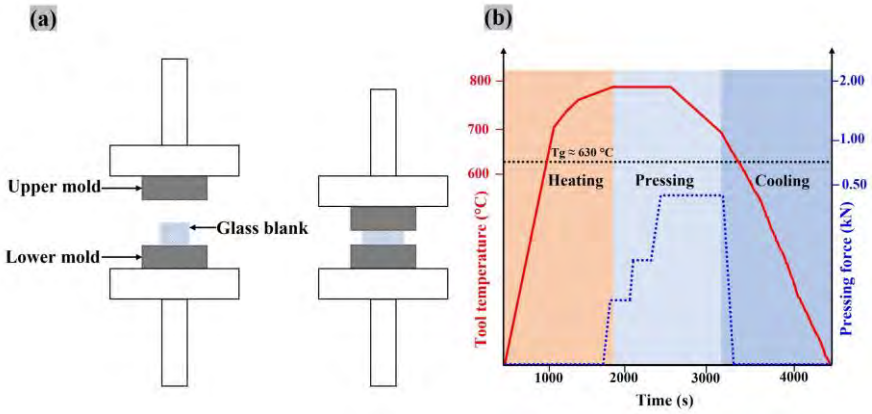

Figure 4.15 Schematic of the PGM (a) testing setup and (b) typical processing cycle.

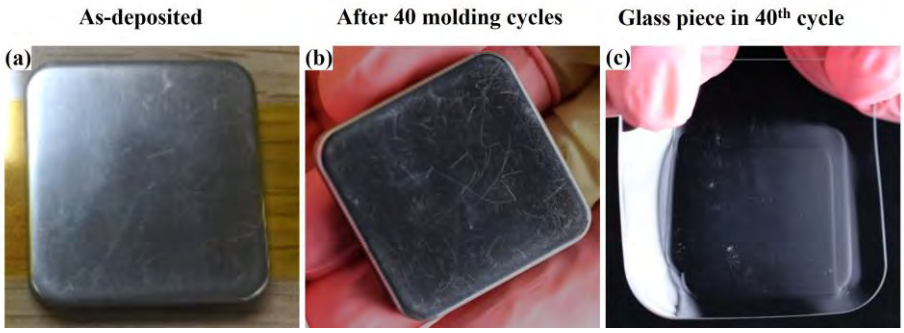

Figure 4.16 Ru–Pt multilayer-coated graphite molds in the (a) as-deposited state, (b) after 40 molding cycles (c) ASG glass in 40th molding cycle.

4.2 Summary

In this study, Ru–Pt multilayer coatings were developed on a graphite substrate with Ti interlayer using the magnetron sputtering technique. Annealing was carried

out in a rough vacuum environment to investigate the microstructure of the as-deposited coatings and their thermal stability at glass molding temperature for varied time durations. SEM and AFM analysis demonstrated the smooth and dense surface morphology of the as-deposited coatings, which almost remained unchanged after annealing, indicating thermal stability in terms of surface properties. HRTEM results showed that the layered structure was preserved even after long hours of heating at 750 °C. Impediment of atomic diffusion and dislocation movement was explained by the addition of interfaces, and this was the enhancement mechanism of mechanical performance and anti-sticking property. The experimental results indicated that the Ru–Pt multilayer coating is a preferrable candidate for glass molding dies, particularly for high-T_g glasses, which was also validated using an industrial glass molding system.

Chapter 5: Annealing and oxidation study of Ru–Cr coatings

5.1 Benefits of Cr_2O_3 and related studies

Hard coatings offer multiple functionalities such as proper adhesion, high thermal stability, and high hardness and are thus recommended to meet the necessities of surface protective coatings applied on the mold material to protect the surface from degradation and increase its service lifetime [147, 202-205].

In the last chapter [206], Ru–Pt multilayer coatings demonstrated significant thermal stability in terms of surface characteristics at glass molding temperature, high hardness, excellent anti-sticking performance and superior oxidation resistance for high T_g-glass. Ru has significantly lower cost than other noble metals (such as Ir and Pt) used as PGM protective coatings. Based on the experimental results, Ru-based coatings are preferable candidates for glass molding dies. The high cost of Pt may limit its industrial application. Consequently, low-cost coating is required for industrial applications. Cr is a low-cost metal that oxidizes easily to form Cr_2O_3 [163, 207, 208]. In general, the formation of an oxide layer on the top of the coating usually protects the underlying coating materials from degradation. In previous studies [209-212], various applications of Ru–Cr were explored including high temperature oxidation, superconductivity, and anti-ferromagnetism. The stability of Cr_2O_3 is recognized up to 1200 °C [211]. Therefore, Ru–Cr could be economical alternatives as protective coating materials for PGM. In this work, Ru–Cr coatings of varied thicknesses were fabricated on a graphite substrate by magnetron sputtering to explore their feasibility as protective coatings for glass molding dies. Further experimental details of Ru–Cr coatings are presented in Chapter 3 (Section 3.2.2). The as-

fabricated coatings were named as A1, B1, and C1, and the annealed coatings (750 °C, 10 h/20 h) were designated as A2/A3, B2/B3, and C2/C3, respectively (Table 5.1).

Table 5.1 Designs of as-deposited and annealed Ru–Cr coatings

Sample state	Sample name	(Ru–Cr/Ti) nm
As-deposited	A1	200-200/50
	B1	600-200/50
	C1	800-200/50
Annealed at 750 °C for 10 h	A2	200-200/50
	B2	600-200/50
	C2	800-200/50
Annealed at 750 °C for 20 h	A3	200-200/50
	B3	600-200/50
	C3	800-200/50

5.2 Results and discussion

5.2.1 Structural analysis

Fig. 5.1 shows the recorded XRD patterns of the graphite substrate and Ru–Cr coated samples before and after annealing with glass coverage. Before annealing, the characteristic x-ray signals of Ru (HCP) and Cr (BCC) with preferred orientation in the (002) and (110) planes, respectively, were identified. With an increase in Ru film thickness in the as-fabricated state, the Ru (002) peak became more intensified, whereas a relatively broader peak of low intensity was observed for Cr (110). The development of the preferred Cr (110) texture is intrinsic in the deposition of a thick

(>100 nm) Cr film and is induced by the minimum surface energy of (Cr) 110 intensity in Cr films [213]. After annealing, no change in the peak position was observed for Ru and Cr, and the peak intensity of Ru was slightly increased with the increased Ru thickness. Besides that, no notable difference was observed in the annealed coatings in comparison with the as-deposited ones. In addition, a Cr-oxide scale (shown in the TEM results) formed, whereas, owing to its extremely low thickness [214], this phase was not detected in the parallel beam mode of XRD measurement.

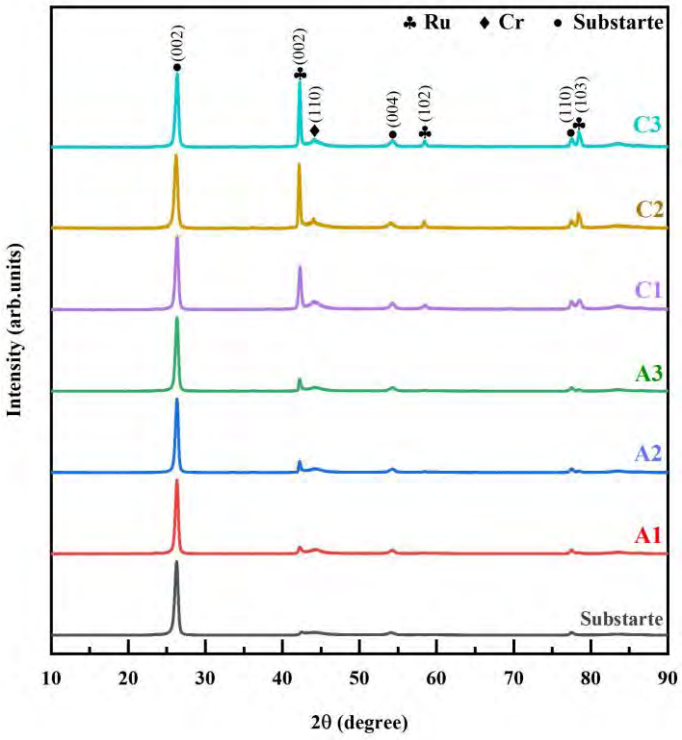

Figure 5.1 XRD patterns of the substrate and Ru–Cr coatings before and after annealing.

5.2.2 Morphology analysis

Fig. 5.2 displays the surface morphology of the developed coatings before and after annealing. In the as-fabricated state, the developed coatings exhibited a coarse surface morphology of nodular-shaped particles. With the increasing thickness of Ru (Fig. 5.2(c)), a cauliflower-like morphology was observed, which was formed by the

agglomeration of nodular nano-sized particles during the film growth. SEM images further reveal that for all coating compositions, larger particle growth was observed with a coating of maximum ruthenium thickness (sample C1). The large particle size is ascribed to the longer deposition duration, which might have permitted the adjacent atoms to reorganize themselves through surface diffusion, resulting in larger particles [215].

In the annealed coatings, surface features slightly different from those of the as-deposited coatings were observed, with newly grown nanometer particles (Fig. 5.2(d)). This indicates the development of the oxide layer covering the underneath protective coating. The EDS spectra of the annealed coatings confirm the presence of O, indicating the formation of an oxide layer on the coating surface. In addition, the annealed coatings exhibited a slightly opaque surface owing to the formation of a thin oxide layer whose thickness is insufficient to cover the underneath surface morphology.

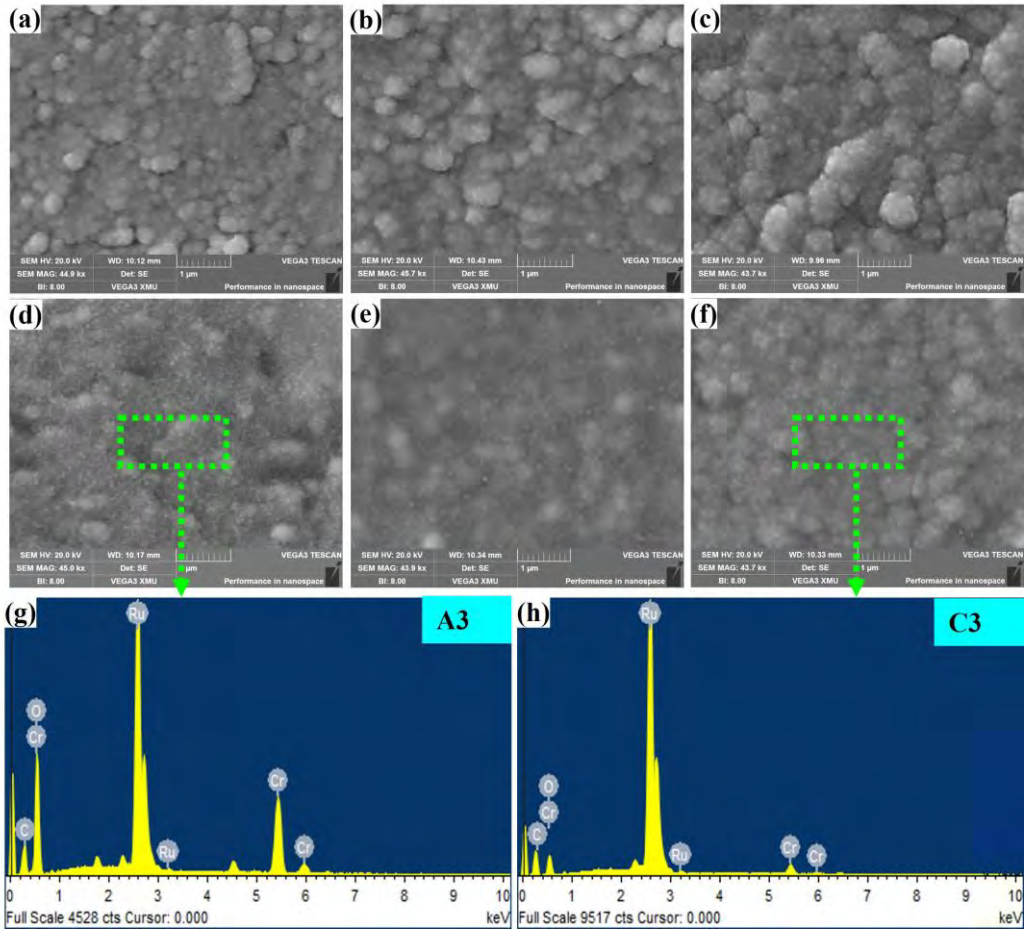

Figure 5.2 Surface morphology and EDS analysis of Ru–Cr coatings; as-deposited: (a) A1, (b) B1, (c) C1, and annealed state: (e) A3, (f) B3, and (g) C3; EDS spectra of the marked areas in (d) and (f) are exhibited in (g) and (h), respectively.

5.2.3 XPS analysis

The recorded XPS spectra of Cr 2p and O 1s for the annealed coatings are exhibited in Fig. 5.3. In Fig. 5.3(a), the high-resolution spectra for Cr 2p demonstrated two major peaks centered at 576.3 and 586.1 eV, which correspond to the Cr^{+3} species from Cr_2O_3 [216-219]. The doublet separation value of 9.8 eV between Cr $2p_{3/2}$ and $Cr_{1/2}$ further confirms the Cr bonding state in the Cr_2O_3 form [220]. The results manifest that only the Cr^{+3} valence state was observed on the top surface of the coatings after annealing. In addition, free Cr was also observed indicating the presence

of metallic Cr. The O 1s spectrum of the annealed samples (Fig. 5.3(d–f)) demonstrated one peak centered at 530.19 ± 0.1 eV, which is the typical peak of Cr_2O_3 [216]. During annealing, the chromium content diffused out to the surface, where it became oxidized and formed an oxide layer. The XPS analysis of the annealed coatings at 750 °C verified the outward diffusion of Cr and its oxidation to Cr^{+3}, which formed a stable Cr_2O_3 layer on the surface.

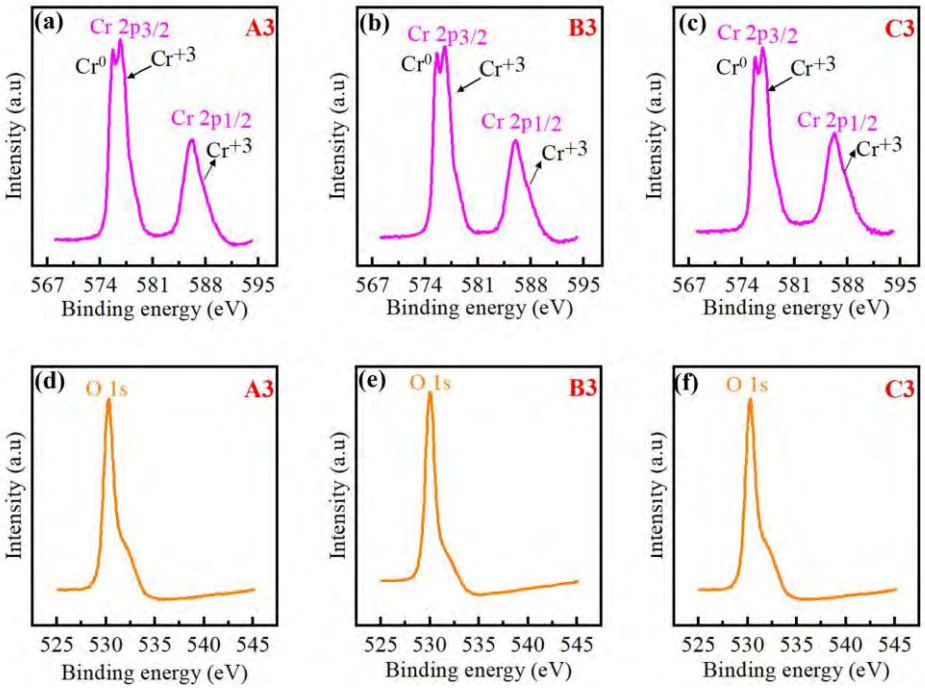

Figure 5.3 XPS spectra of (a–c) Cr and (d–f) O 1s of the annealed coated samples A3, B3, and C3.

5.2.4 Mechanical properties

The hardness *(H)* and Young's modulus *(E)* of the Ru–Cr coatings were determined using a nano-indenter and are presented in Fig. 5.4 The results demonstrated that the variation in thickness of ruthenium influences the mechanical properties of the coatings in the as-deposited state. In Fig. 5.4(a), the hardness of the annealed coatings (A2) initially increased owing to the formation of Cr_2O_3, whereas

further heating led to a decrease in hardness, which can be attributed to the change in grain size (grain growth) during longer annealing time [204]. The elastic modulus also exhibited a similar trend, just as hardness. Initially, a lower value was exhibited by the coatings before annealing. Then, the annealing temperature resulted in an increase in modulus, whereas prolonged annealing caused a slight reduction in modulus. Similar patterns were recorded in the coating designs of Fig. 5.4(b) and (c), while noticeable variations in the mechanical property values were observed due to the varied thickness of Ru film.

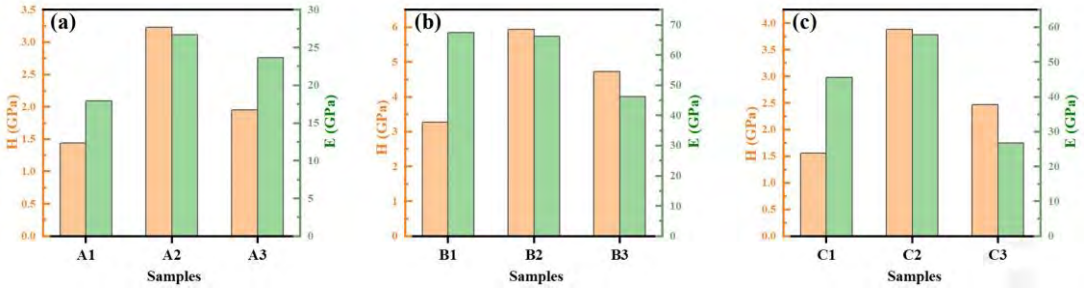

Figure 5.4 Nano-hardness and modulus of Ru–Cr coatings.

5.2.5 TEM-HRTEM analysis

5.2.5.1 As-deposited coatings

Fig. 5.5 exhibits cross-sectional TEM/HRTEM images of the Ru–Cr coating in the as-deposited state (sample A1). In Fig. 5.5(a), the Ru coating demonstrated a nano-scale columnar structure, which is preferentially oriented. The distinctive faceted column tops suggest the existence of preferential growth directions because atoms can diffuse to preferred low-energy sites following surface absorption [221]. The grain growth initiated with thin columns and remained cylindrical and a bit wider as the film grew out. Beneath the Ru layer, the Cr layer also revealed an ordered columnar structure. These results are in reasonable agreement with the XRD results explained

above, indicating that on the Cr film, the Ru film was grown with enhanced crystallinity.

In addition to the column-like structure, the intercolumnar voids were also revealed by the columnar microstructure of the Ru–Cr coating, outlining the prominent dendritic pattern. It is noted that the columnar microstructure provides tolerance against erosion and tensile stress related to the segmentation of coating by intercolumnar gaps [221]. An HRTEM image of the Ru layer is presented in Fig. 5.5(b), and the IFFT filtered-image of the marked area is displayed in the inset of Fig. 5.5(b). The measured interplanar spacing distance was 0.217 nm, which corresponds to the Ru (002) plane. Similarly, for the Cr layer, the IFFT filtered-image of the marked area shown in the inset of Fig. 5.5(c) revealed a d-spacing of 0.202 nm, which corresponds to the Cr (110) plane.

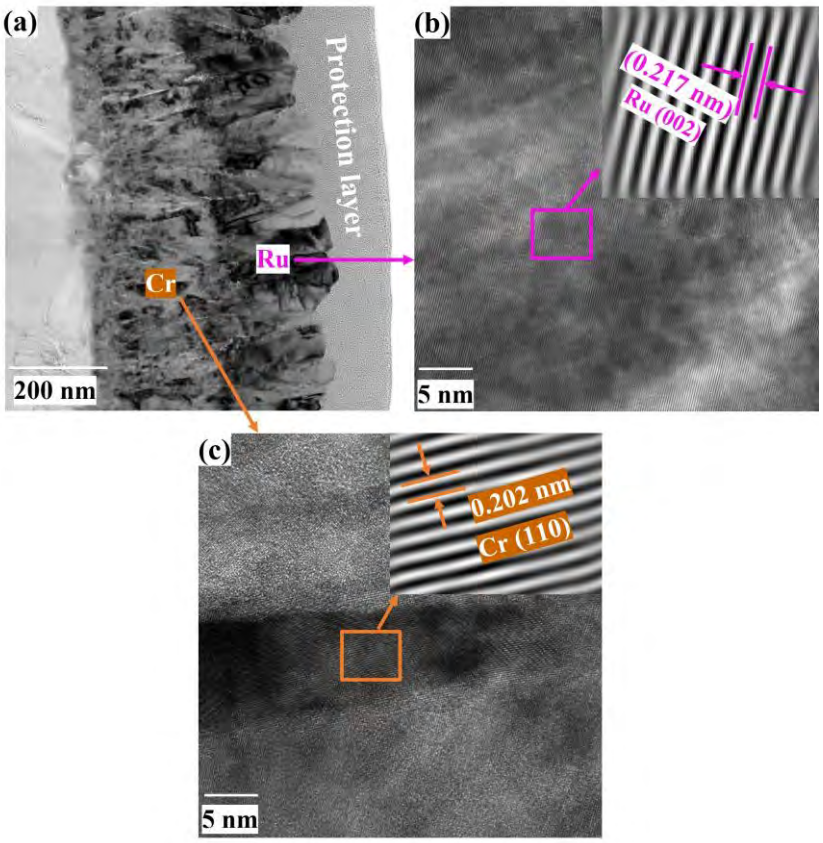

Figure 5.5 TEM and HRTEM images: (a) sample A1, (b) HRTEM image of Ru coating, and (c) HRTEM image of Cr coating.

The cross-sectional morphology of the as-deposited coatings (B1, C1) is shown in Fig. 5.6. A highly dense columnar morphology can be observed, with growth starting with narrow equiaxed columns and growing relatively wider, perpendicular to the substrate (Fig. 5.6(a, b)). A wavy structure of the nano-crystalline coatings was observed, which is attributed to the intrinsic stress (developed due to film growth dynamics) and extrinsic stress (due to external forces such as thermal stress).

The magnified TEM images of the marked areas in Fig. 5.6(a) and (c) are displayed in Fig. 5.6(c) and (d), respectively. The average columnar grain width of sample C1 was approximately 75 ± 5 nm. Inter-columnar gaps, which developed during the columnar growth, can also be observed. Owing to the preferred oriented growth of the columnar structure, a feather-like appearance can be observed between columnar voids. The growth of feathery grains is attributed to the continuity of columns in the coating layer [222]. Besides columnar gaps, the columnar structure also exhibited a small amount of internal porosity owing to the shaped tip of the columnar branches [223]. The insets of Fig. 5.6(b) and (d) display the corresponding SAED patterns of the Ru layer of samples B1 and C1, respectively. The SAED analysis depicts spots that clearly indicate the high crystallinity of the Ru layer in the developed coatings.

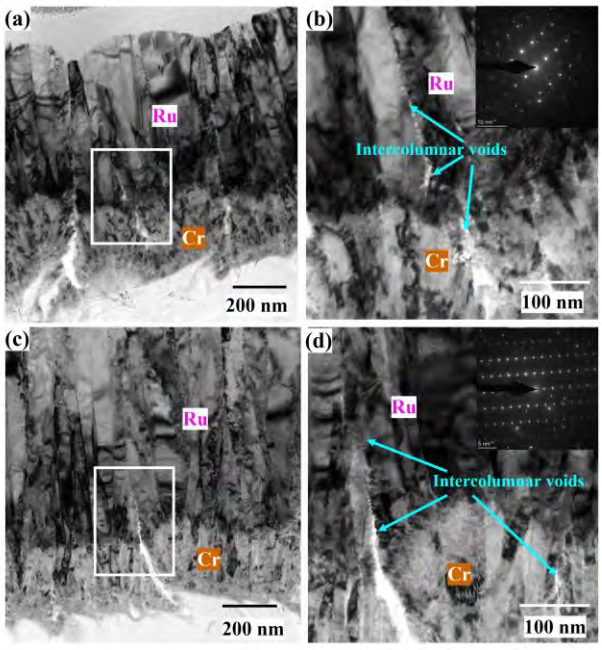

Figure 5.6 Cross-sectional BF-TEM images of as-deposited coatings: (a, b) sample B1 and (c, d) sample C1.

Fig. 5.7 shows STEM images of the as-deposited coatings acquired in HAADF mode, as well as the corresponding EDS maps of the coating elements Ru (green), Cr (orange), O (blue), and Ti (red). The EDS mappings reveal the homogenous deposition of the coating elements. One interesting finding is the existence of the O element in the as-deposited coating (Cr) layer. Based on the experimental results, it is suggested that the oxygen content is sputtered along with the chromium sputtering. Regardless of whether oxygen atoms are adhered to the surface of the chromium target or partially oxidized [224], the presence of oxygen in the chromium layer is confirmed in all the as-deposited coating designs.

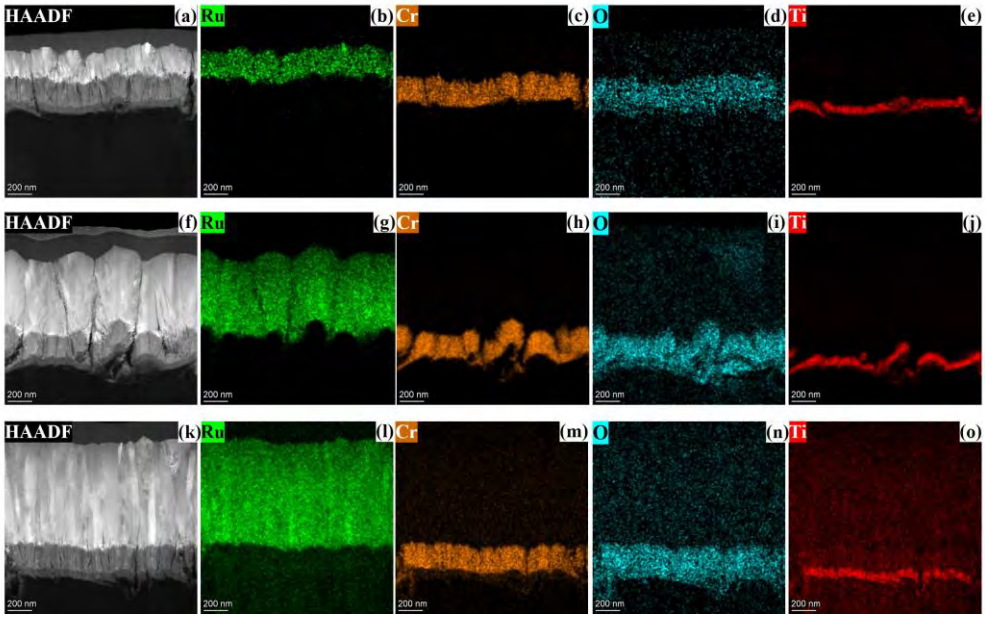

Figure 5.7 HAADF-STEM images and EDS color mappings of as-deposited coatings: (a–e) sample A1, (f–j) sample B1, and (k–o) sample C1.

5.2.5.2 Annealed coatings

The cross-sectional morphology of the annealed coatings (sample A2) is exhibited in Fig. 5.8. Annealing caused the oxidation of Cr, which formed an oxide scale via outward diffusion on the top of the Ru layer as depicted in the TEM micrograph. The SAED pattern of the oxide layer depicts crystalline diffraction rings of (012), (104), and (110), which correspond to the Cr_2O_3 phase, confirming the presence of crystalline grown Cr_2O_3 scale on the top surface.

Based on the TEM image observation (Fig. 5.8(a)), it is apparent that the external oxidation phenomena occurred predominantly, which led to the formation of oxide scale, i.e., outward movement of Cr atoms instead of inward diffusion of oxygen atoms into the bulk [225]. The growth of the pure chromia scale is attributed to the primary outward movement of cations and approximately 1% inward movement of anions in the oxide scale [208, 226]. It is suggested that the occurrence of inward

transport of oxygen along the oxide scale grain boundaries may result in compressive stress by the formation of the oxide scale at the scale–metal interface or inside the scale. As grain boundaries provide a faster channel for diffusion phenomena than the bulk [99, 117, 227], it is suggested that the outward diffusion of the oxide-forming element Cr occurred primarily through the grain boundaries of the upper layer (Ru coating) by which the chromium atoms reached the surface and formed an oxide scale via oxidation phenomena.

The inset of Fig. 5.8(a) presents the EDS (atomic percentage of elements) analysis of the marked area in the oxide scale. Based on the EDS composition, it can be deduced that when the Cr cation reaches the top surface, it starts to form Cr–O. Primarily, the oxide scale formation is of Cr_2O_3, as confirmed by the SAED pattern. Besides that, Cr is likely to be present in the metallic form near the oxide scale/metal interface and also in the Cr–O form. Beneath the oxide scale, ruthenium grains are clearly observed along with their grain boundaries owing to an increase in grain size by annealing, and their calculated average columnar width was ~110 ± 10 nm. The SAED pattern of ruthenium coating, shown in Fig. 5.8(c), showed a spot pattern, similar to the as-deposited coating, indicating the stability of the ruthenium layer. The columnar structure of the Cr coating appeared to change from that of the as-deposited coating owing to the thermally activated motion of Cr atoms. In addition, because of the presence of oxygen in the Cr layer beneath the Ru layer (as shown in Fig. 5.7), the annealing phenomena is likely to result in the partial oxidation of Cr.

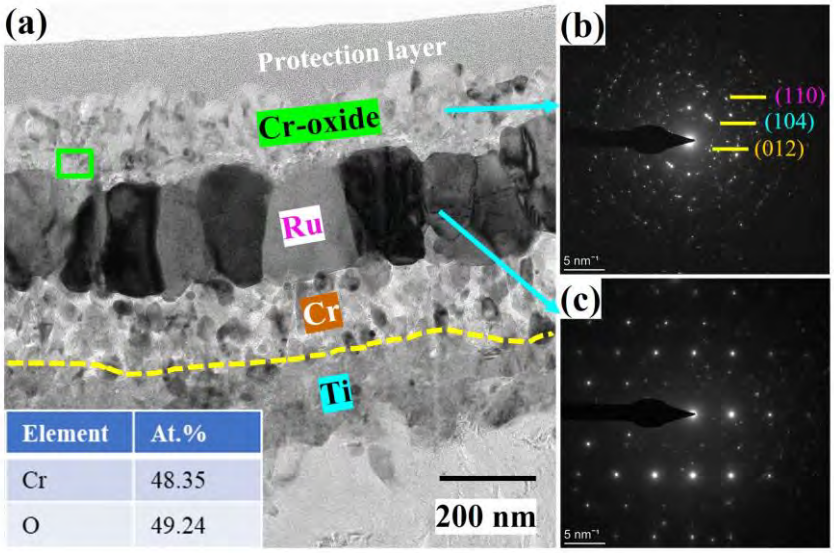

Figure 5.8 TEM characterization of annealed coating (sample A2): (a) TEM image and SAED pattern of the (b) Cr_2O_3 layer and (c) Ru layer.

The microstructural examination of annealed coated sample A3 is shown in Fig. 5.9. The cross-sectional TEM image (Fig. 5.9(a)) of the 20 h heated sample presented a similar behavior to that exhibited by the 10 h heated sample (Fig. 5.8(a)). No noticeable difference was observed in the thickness of the chromia scale, indicating the stability of the oxide scale, which further prevents the underneath coating element (Cr) from further oxidation. The width of ruthenium grains (~70 nm) was reduced with further annealing, which possibly indicates grain refinement with longer annealing.

Moreover, the SAED pattern in the inset image (Fig. 5.9(a)) indicates the enhanced preferential growth and high crystallinity of the ruthenium coating layer. According to the EDS analysis of the ruthenium coating, the maximum recorded Cr content was 2.42 at. %, indicating that no intermetallic phase (Ru–Cr) was formed. Moreover, based on the Ru–Cr phase diagram [228], intermetallic phases start to form at a temperature of 800 °C. An HRTEM image of the chromia scale is exhibited in

Fig. 5.9(b). The measured d-spacing values for different planes were 0.360 and 0.261 nm, which correspond to the (012) and (104) crystallographic planes of the chromium oxide scale. Based on the HRTEM, it is also confirmed that with 20 h of annealing, the chromium oxide scale sustained the crystalline nature [229]. Fig. 5.9(c) displays the interfacial zone of the Ru–Cr coating, which presents lattice distortion at the interface, and its IFFT-image is shown in Fig. 5.9(d). At the interfacial area, misfit dislocations were identified, which were marked with the symbol "T". At the interface, dislocations are restricted, which could contribute to the coating strength [102].

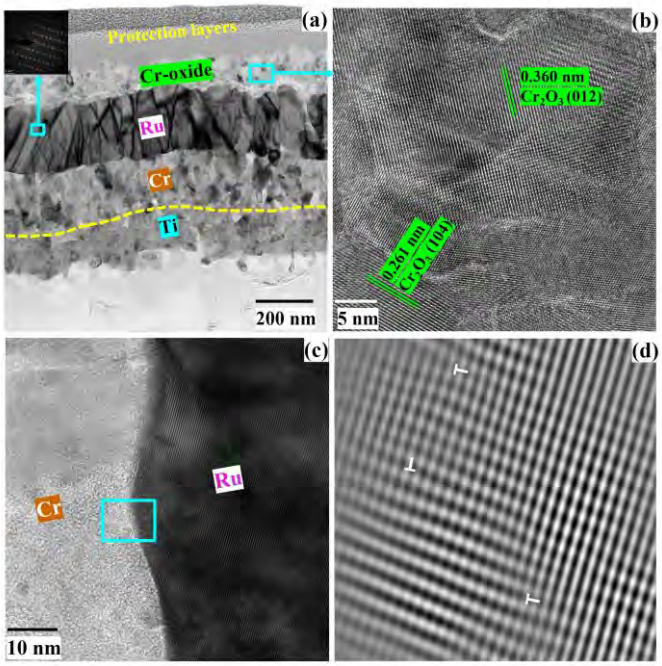

Figure 5.9 TEM analysis of annealed coating sample A3: (a) cross-sectional BF-TEM image, (b) HRTEM image of oxide scale, (c) HRTEM image of Ru–Cr interfacial area, and (d) IFFT image of the marked area in (c).

To compare the annealed coatings with the as-deposited ones, a STEM-EDX analysis was carried out on the cross-sectional annealed samples A2 and A3, as depicted in Fig. 5.10. The existence of Cr and O layers on the top of the annealed

coatings can be inferred from the observed elemental mappings, which indicate the formation of Cr_2O_3 phase. The Ru elemental mapping indicates the stability of the structure, similar to the as-deposited states. However, cracks and porosity can be observed in the Ru coating (Fig. 5.10(a, f)), which were caused by the outward diffusion of Cr and Cr–O gaseous phase due to the presence of oxygen. A significant number of micro-cracks can be observed in the annealed Cr coating layer. No significant difference in the thickness of the oxide scale was observed after 10 and 20 h of annealing, indicating that the maximum thickness is already achieved in the initial annealing hours, and during further annealing, the chromia scale act as a barrier to the outward movement of Cr and inward diffusion of oxygen [230]. Furthermore, cracks and porosity in the Ru layer can be observed in the STEM-HAADF images, which are induced during the annealing process due to outward Cr movement and oxygen diffusion from the (Cr) layer, which could possibly be accelerated by the short circuits (grain boundaries, defects etc.). It is noticed that the total thickness of the Ru layer remained stable, whereas the thickness of the Cr and Ti layers expanded to ~350 and ~190 nm, respectively.

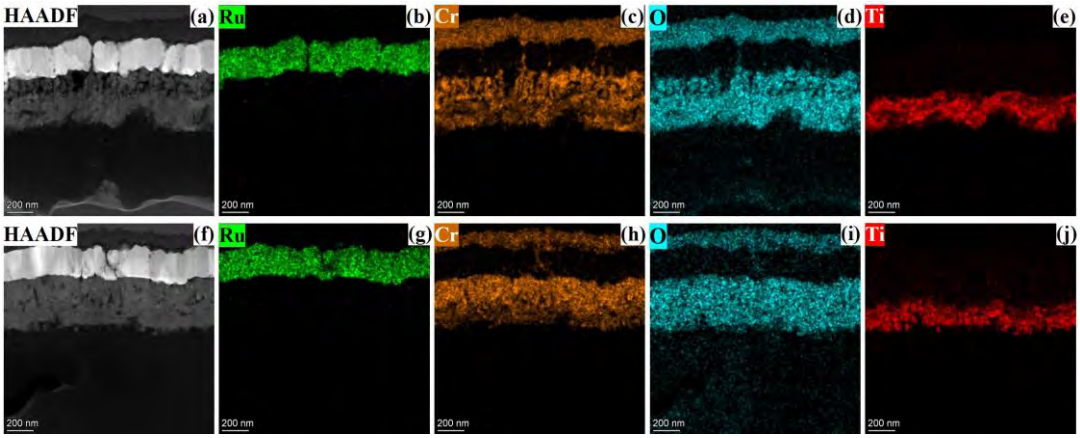

Figure 5.10 HAADF-STEM images and EDS elemental mapping of annealed coatings: (a–e) sample A2 and (f–j) sample A3.

Figure 5.11 illustrates BF-TEM images, as well as their SAED pattern and EDS mappings, of annealed coatings (sample B3). It is evident that the oxide scale has grown on the top of the Ru surface. The formation of oxide-scale is primarily controlled by outward Cr-ion diffusion. The average thickness of the oxide scale is ~140 ± 15 nm, which is the slightly lower than that observed in sample A3. It is noted that the annealed sample with increased Ru thickness (B3) restricts the Cr diffusion under the same annealing conditions in comparison with the reduced Ru thickness (A3). The black content in the HRTEM images could possibly be due to the presence of carbon atoms. It is highly possible that during long hours of annealing (750 °C), carbon atoms diffuse into the coating structure owing to the Kirkendall [135, 136, 231] effect. During annealing, nanometric voids form between the Ti–C interfacial region. These voids serve as graphite atom diffusion paths.

The SAED pattern of the Ru coating represents a similar diffraction pattern to that recorded before and after annealing of sample A1 and sample A3, respectively. This confirms that with the increased thickness of Ru, no change in the crystallinity state of Ru was observed, and its enhanced crystallinity was sustained. However, the voids in the Cr layer can be observed clearly near the Ru–Cr interfacial area (Fig. 5.11(d)). The thermally activated motion of Cr particles during annealing causes the formation of voids as the annealing process progresses in time. During annealing, the diffusion of Cr atoms creates vacancies, and the coalescence of excess vacancies results in the formation of small voids. Because of the continuity of the annealing process, vacancies form, causing void enlargement, and their coalescence results in pore formation [231]. The polycrystalline state of the Cr layer is confirmed in the SAED pattern (Fig. 5.11(e)). STEM-EDS mappings revealed a similar result as

demonstrated in Fig. 5.10. Some pores can be observed in the HAADF image. Similar mapping results were obtained, as exhibited in Fig. 5.10. No noticeable change in Ru thickness was recorded after annealing, whereas Cr expanded from 200 nm (as deposited) to 360 ± 10 nm, which is similar to that of sample A3.

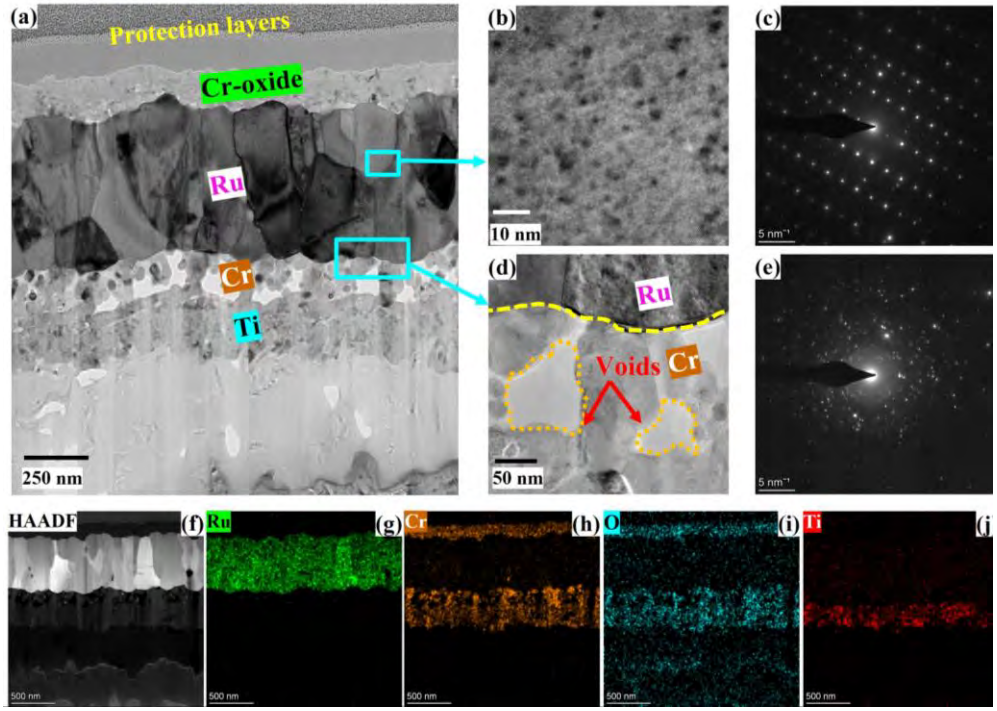

Figure 5.11 Overview of TEM micrograph and EDS mappings of annealed coatings (sample B3).

Fig. 5.12 exhibits the TEM micrographs of annealed coating samples C2 and C3. The oxide layer can clearly be seen on the top surfaces of both annealed samples, even with the maximum thickness of Ru (800 nm) in the developed coatings. It is worth noting that, in contrast to the previous results, the oxide layer thickness was reduced, with a calculated average thickness value of 70–75 nm after 10 and 20 h of annealing. The calculated columnar width of Ru grains after 10 and 20 h of annealing was 110 and 75 nm, respectively. The Cr grain (inset of Fig. 5.12(a, b)) were transformed from columnar to nodular shape of different sizes due to the annealing.

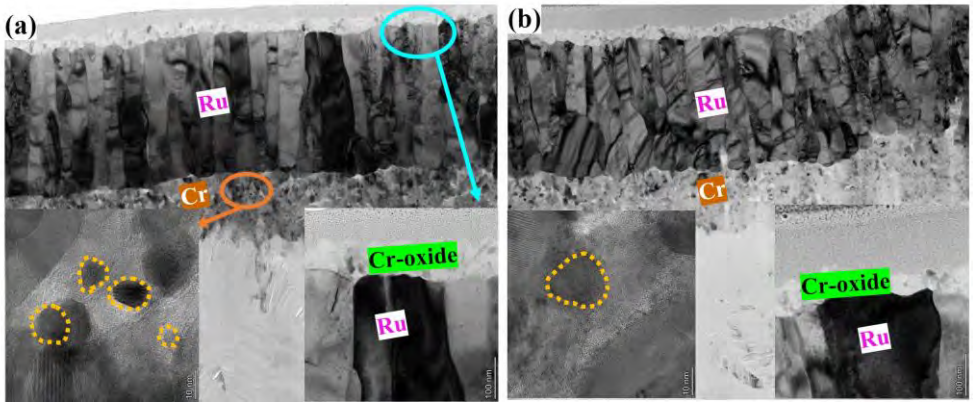

Figure 5.12 Cross-sectional BF-TEM and HRTEM micrographs of annealed coatings: (a) sample C2 and (b) Sample C3.

Fig. 5.13 depicts TEM micrographs of the annealed coatings near the interfacial areas. For the Ru–Cr interfacial area, a sharp and clear interface is observed owing to the significant thermal stability of Ru at 750 °C. The outward diffusion of Cr has primarily occurred through short circuits (grain boundaries, defects etc.). Based on the EDS data, no intermetallic formation of Ru–Cr was observed. The magnified images (Fig. 5.13(b, c)) indicate inter-diffused regions and the disappearance of the clear Ti–Cr interface. As a result of the thermally activated motion between two metals, inter-diffusion caused solid-solution phenomena and the formation of a Ti–Cr alloy layer. Moreover, as a consequence of the inter-diffusion mechanism, vacancies are created in the interfacial area. The coalescence of excess vacancies will eventually result in the formation of small voids, which are distributed at or near the interfacial region [232]. The SAED pattern of the inset images depicts a multi-ring pattern, which denotes the polycrystalline state of the inter-diffused areas.

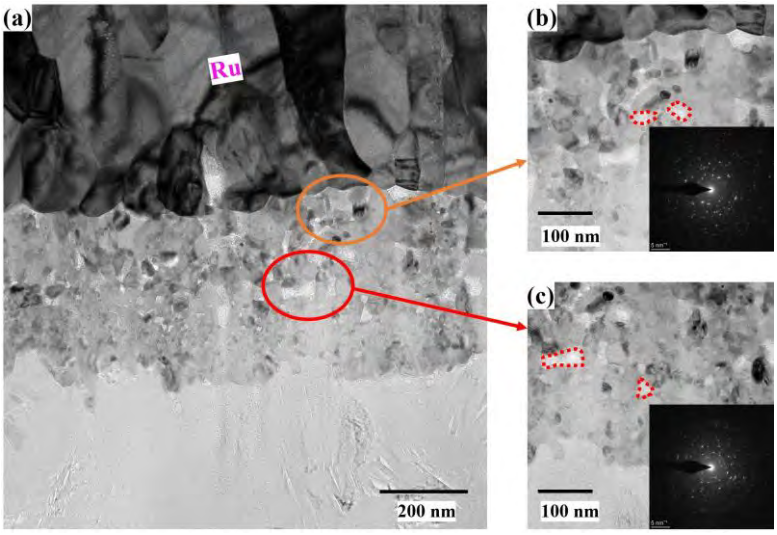

Figure 5.13 TEM micrograph of annealed sample C3 near the interfacial areas.

STEM-EDS mappings of annealed coatings (C2/C3) are shown in Fig. 5.14. As in the coated sample A2/A3 (Fig. 11), it can be observed that Cr diffused out and formed a thin oxide layer on the top free surface of the coatings. However, comparatively, its oxide layer thickness is reduced under the same annealing conditions. The expansion of the Ti layer indicates its interdiffusion with the upper Cr layer. The existence of voids near the Ru–Cr and Cr–Ti interfaces can be clearly observed, which developed during the thermal diffusion. Overall, Ru mapping demonstrates the stability of the coating owing to its increased chemical inertness.

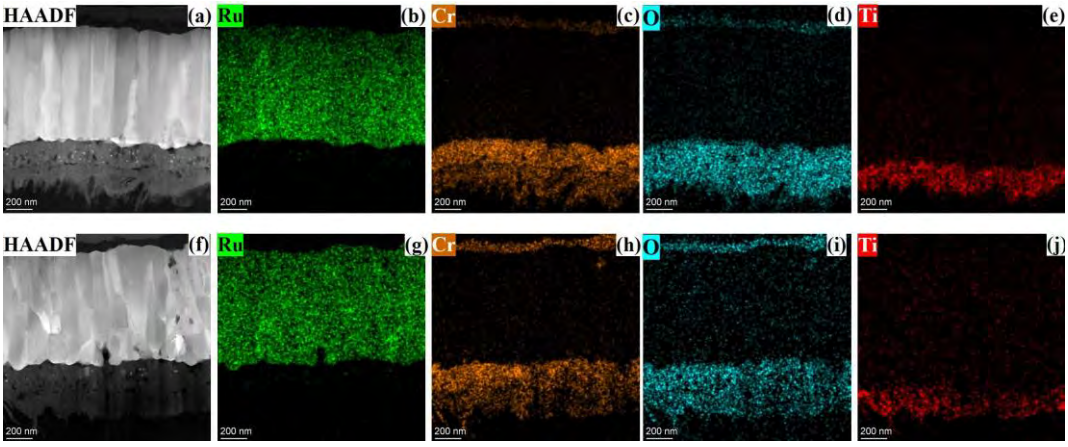

Figure 5.14 HAADF-STEM images and EDS mappings of (a–e) sample C2 and (f–j) sample C3.

Photographs of the sputtered Ru–Cr coatings in their as-grown and annealed states, as well as the tested glass specimens that were employed as coverage on the coated sample during annealing phenomena, are shown in Fig. 5.15. A silvery-gray color of the coated samples in the as-deposited state can be observed, which is due to the intrinsic color of the Ru top layer. After annealing, the coating color is changed to a slightly yellowish-brown color. The color change indicates the oxide formation on the top surface as a result of outward diffusion and oxidation of Cr. However, TEM observations revealed that the oxide layer thicknesses decrease with increased thicknesses of Ru. No glass adhesion was observed on the top surface of the annealed coatings, as revealed by the SEM-EDS and XPS analyses, indicating the stability of the Cr-oxide scale.

In addition, the tested glass specimen remained transparent in all of the annealed coated specimens. However, a compromised thickness of the Ru–Cr coating design can effectively improve their performance for PGM. In the literature [233], it is recognized that Cr oxidizes easily to form the Cr_2O_3 phase; however, its stability is recognized up to 1200 °C (significantly higher than the glass molding temperature). Moreover, the stable oxide phase protects the underneath coating layers. In the long run, the oxide coating may degrade due to the thermo-mechanical forces during the molding cycles, which would result in coating degradation and very likely compromise the glass transparency. Nevertheless, the annealing results of coated samples with glass specimens indicates that Ru–Cr coatings are reasonable cost-effective materials for glass molding dies.

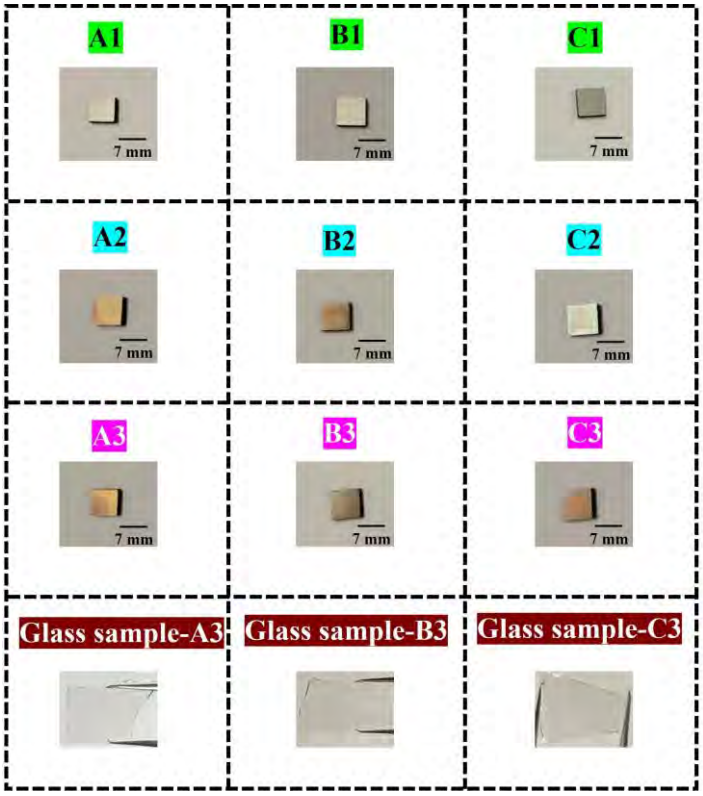

Figure 5.15 Photographs of the annealed coated (Ru–Cr) samples and tested glass specimens.

5.2.6 Simulation results

The simulation results based on the phase field modeling are shown in Fig. 5.16. All three coating designs were developed in the same manner as the experimental data, and the same parameters were used to acquire the results after 10 and 20 h of annealing. It can be observed that the computational results for all three designs are in agreement with the experimental results. The formation of oxide scale owing to the outward diffusion of Cr can be observed in all coating designs, and its thickness remained relatively similar after 10 and 20 h of heating. Moreover, as revealed in the experimental results, this oxide scale consists of metallic Cr (owing to outward movement at the top surface) and Cr–O and its subsequent oxidation to Cr_2O_3.

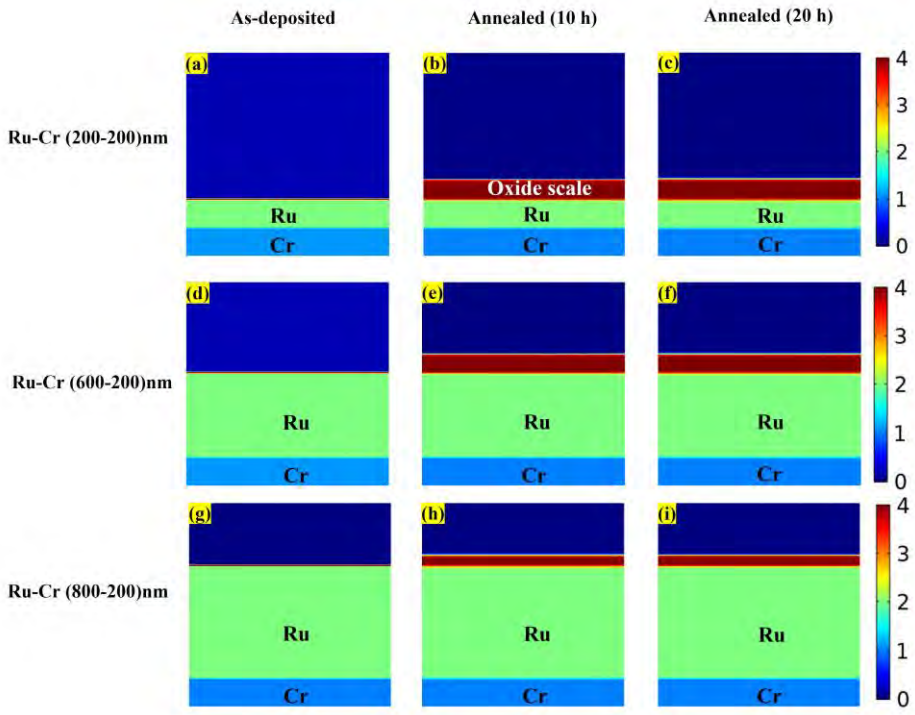

Figure 5.16 Simulation results of as deposited and annealed (10 h/20 h) coatings.

The graph of oxide layer thickness vs. annealing time for annealed coatings is displayed in Fig. 5.17. Generally, the oxidation of Cr metal leads to oxide formation on the surface, which covers the material and prevents any further oxidation. The requirement of further growth needs the metallic specie to be dissolved and its movement via oxide development [234]. During the initial heating hours, a logarithmic growth curve was observed, which reached its maximum thickness within 10 h, and then remained steady, indicating that further growth of the oxide layer stopped, and the oxide scale thickness remained stable with further heating. The values of k1 for the 200 and 800 nm Ru samples are 4 and 2, respectively, demonstrating that the 200 nm Ru samples consume (outward diffusion) more Cr during annealing than the 800 nm Ru samples. In addition, it can be observed that a variation in the Ru layer thickness resulted in a variation in the oxide layer thickness, indicating that a thicker Ru layer can inhibit the outward migration of Cr and its

subsequent oxidation. After annealing, a sample with a Ru thickness of 800 nm has nearly half the oxide layer thickness of a sample with a Ru thickness of 200 nm.

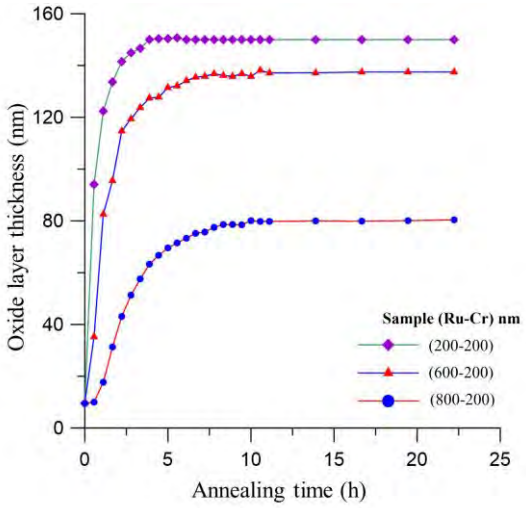

Figure 5.17 Oxide layer thickness graph with annealing time.

Fig. 5.18 presents a comparison between the experimental and simulation results of Cr in the Ru layer (sample B3) after annealing. The EDS mapping results demonstrated the distinct concentration of Cr in the oxide layer and in the Cr layer underlying the Ru layer, whereas the Cr concentration is extremely low in the Ru layer. Meanwhile, the simulation result for Cr concentration gives a similar result with a better quantitative explanation. Even though the color scale is relatively limited, it provides some indication of the traces of Cr element in the Ru layer. Therefore, based on the results, STEM EDS mapping provides a qualitative analysis in comparison with the quantitative analysis of phase field modeling.

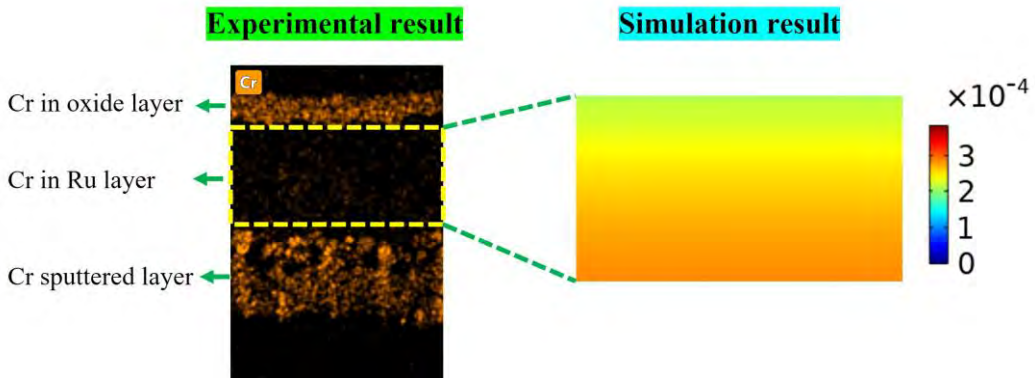

Figure 5.18 Cr concentration in Ru layer in the annealed coatings.

5. 3 Further remarks

A comparison has been made between experimental and simulation data to understand the diffusion and oxidation mechanisms of Ru–Cr coatings. Based on the results, it is revealed that increased thicknesses of Ru serve as a diffusion barrier to Cr and also suppress interdiffusion between Ru and Cr. In addition to the previous results, another interesting finding has been revealed, which is explained below.

In addition to the previously fabricated Ru–Cr coating designs, an additional coating design with Ru thickness of 400 nm while maintaining the Cr thickness consistent with the previously fabricated designs was also prepared. Fig. 5.19 displays the BF-TEM and HAADF images and EDS elemental mappings of the Ru–Cr/Ti (400-200/50 nm) coatings in the as-fabricated and annealed state. The experimental findings, such as columnar morphology and outward diffusion of Cr, were consistent with prior results; however, contrary to the previous results obtained, this design showed a reduced average oxide layer thickness (90–95 nm), less than that of the comparative Ru-thicker sample (when Ru thickness was 600 nm). This observation was surprising and indicates that some other process was likely involved, which resulted in the reduced thickness of the oxide layer in comparison with the B2 and B3

sample. Initially, after the first annealing test (10 h), it was presumed that there was an experimental error. However, the second annealing test on a different sample (20 h) showed the same result, which verified the unpredictable findings regarding the oxide scale thickness. Consequently, this finding provides insights for future research.

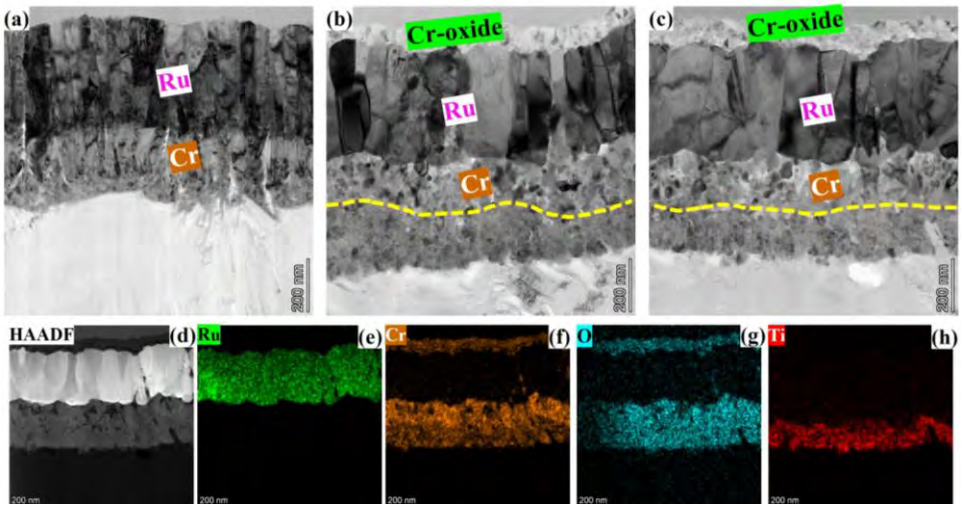

Figure 5.19 BF-TEM images of Ru–Cr/Ti coated sample (400-200/50 nm): (a) as-fabricated, (b) 10 h annealing, and (c) 20 h annealing; (d) and (e–f) show the HAADF image and corresponding elemental mappings, respectively.

5.4 Summary

Ru–Cr coatings with different thickness of Ru were fabricated using the magnetron sputtering technique. The effect of annealing time (10 h/20 h) at 750 °C on the mechanical properties and microstructures of the coatings were investigated. After annealing, Cr-oxide scale was developed on the Ru–Cr coatings. During annealing, outward movement of Cr and its oxidation to Cr^{+3} resulted in the stable Cr_2O_3 formation, which enhanced the hardness of the developed coatings. The Ru–Cr deposits exhibited a columnar feature with preferred crystalline orientation, as revealed by the nanostructure characterization. According to the TEM results, the Ru–Cr coatings with increased thickness of ruthenium relatively impeded the outward

transportation of Cr and acted as a diffusion barrier. Furthermore, due to the annealing effect, the thickness of the Cr and Ti interlayer was increased, and the disappearance of the interface (Ti–Cr) induced inter-diffusion and alloy formation, whereas the Ru thickness remained the same. Glass adhesion of the developed coating designs was not observed for different time durations, predicting the feasibility of Ru–Cr coatings for PGM. The phase field modeling data reflected the experimental findings of annealed Ru–Cr coatings and demonstrated that increased thicknesses of Ru result in relative inhibition of the outward diffusion of Cr.

Chapter 6: Conclusion and suggestions for future research

The aim of this thesis was to design and develop stable thin film protective coatings for glasses with high glass transition temperature glasses in PGM technology. In this chapter main conclusion of this thesis is summarized, and future research directions are suggested.

6.1 Conclusion

PGM is a modern manufacturing technology that allows mass production of optical and precision glass components. Glass molding tools must exhibit high-temperature strength as well as significant wear and oxidation resistance. Previous studies have reported that PtIr coatings with various interlayers are the most widely employed molding tools to achieve anti-sticking properties and thermal stability in PGM. For high-T_g glasses (e.g., ASGs), noble metal coatings may still suffer from oxidation and sticking problems when $T > 700$ °C. Furthermore, Ir is three to four times more expensive than Pt, which discourages its use in the glass industry. Thus, new coating systems must be explored to address these challenges. In the noble metal group, Ru has a superior oxidation resistance and better mechanical properties, and it can be a potential candidate for PGM at high temperatures. In addition, the cost of Ru is significantly lower than that of Ir. Therefore, Ru seems a viable choice for PGM coatings. Sputtering, which is widely utilized as an industrial deposition method for PGM coatings, was used to develop the new coating systems owing to its adaptability in depositing various types of thin film materials.

For the first coating design, Ru–Pt multilayer coatings (40 nm × 21 layers) were prepared on a graphite substrate with a 50 nm Ti interlayer using the DC magnetron

sputtering technique. The coatings were annealed at glass molding temperature of 750 °C in a rough vacuum environment with glass coverage to study its anti-stick performance for glass molding. SEM and AFM analyses demonstrated the smooth and dense surface morphology of the as-deposited coatings, which remained almost unchanged after annealing with different time durations, indicating adequate thermal stability at the molding temperature in terms of surface characteristics. Glass sticking was not detected in SEM and XPS analyses, indicating the inertness of the coatings. Nanoindentation revealed an increase in mechanical performance with annealing time, caused by the improved coherency of Ru/Pt interfaces after short-term annealing and solid solution hardening after long-term annealing. The HRTEM results are well correlated with the above observations. Most importantly, it is shown that the layered structure was preserved even after 40 h of heating at 750 °C. These results indicate that the Ru–Pt multilayer structure is a preferable candidate for glass molding dies, especially for thermoforming high-T_g glass in the temperature range of 700–800 °C. This has been confirmed in the industry with a glass molding system.

In the Ru–Cr coating design, Ru–Cr coatings were developed on graphite substrates with varying thicknesses of Ru to study the oxidation phenomena of the new design due to annealing and its feasibility for PGM coatings for high-T_g glasses. All of the coated designs were annealed with ASGs glass pieces to analyze the anti-adhesion of the developed coatings to glass samples. Considerable transparency of the glass samples was achieved, showing the viability of the protective coatings. The microstructural and mechanical properties of the Ru–Cr coatings were evaluated in the as-fabricated state and annealed state after a long-time annealing (10 and 20 h). The annealed coatings revealed the formation of an external oxide scale owing to the

outward diffusion of Cr. An enhancement in mechanical properties was observed in the annealed coatings in comparison with the as-deposited ones owing to the hard oxide scale. Nanostructure analysis of the Ru–Cr coatings revealed a columnar morphology with a preferred crystalline orientation. Furthermore, based on the TEM results, a greater thickness of Ru relatively hindered the outward transport of Cr and acted as a diffusion barrier. Moreover, an expansion in the coating thicknesses of Cr and Ti was observed, which likely led to the alloy formation, whereas the Ru coating thickness remained unchanged, indicating the stability and protection of underlying materials from coating degradation.

Finally, a phase field model was established to study the diffusion and oxidation behavior of the Ru–Cr coating system. Based on Fick's law, outward diffusion of Cr occurred, resulting in the formation of an oxide scale, which was in accordance with the experimental findings. In addition, it was revealed that the oxide scale formed in the initial heating hours and its subsequent growth stopped before 10 h, whereas with further annealing, the oxide scale thickness remained approximately unchanged, predicting its stability.

Overall, this thesis addressed the study and application of new stable coating design systems for thermoforming high-T_g glasses with PGM technology, where high molding temperatures are required.

6.2 Suggestions for future research

In this thesis, the primary focus was to develop stable PGM coatings for thermoforming high-T_g glasses in order to protect the mold material, prolong its service lifetime, and to enhance the anti-sticking performance. In this regard, various

pure metallic targets were employed to develop and investigate their performance for PGM coatings in a multilayer design, which combined the attractive characteristics of different materials to enhance the microstructural and mechanical performances. For future research, experimental investigation (with varied Ru thickness) as well as simulation modeling of the Ru-Cr coating design is suggested to explore the formation of various transition oxides of Cr during annealing.

Second, in terms of mechanical evaluation, hardness is the most important mechanical property for industrial coating applications involving contact and sliding. Several studies have demonstrated the mechanical performances of the various PGM coatings; however, it is unclear how the room-temperature performances correlate with high-temperature ones or with the lifetime of coatings in PGM cycles. This indicates the limitation of the study of coatings for PGM. This is probably caused by the unavailability of accurate devices to explore the tribological behavior at glass-molding temperatures. The measurements of high temperature tribological performances and the development of quantitative models revealing the influence of various degradation mechanisms are therefore suggested for future studies.

Finally, study of thin film alloy coatings, including metallic, ceramic, and metallic–ceramic alloy coatings, is suggested to explore and investigate their practicality in order to maximize the performance of PGM coatings.

References

[1] Y. Zhang, G. Yan, Z. Li, and F. Fang, "Quality improvement of collimating lens produced by precision glass molding according to performance evaluation," *Optics Express,* vol. 27, no. 4, pp. 5033-5047, 2019.

[2] P. He *et al.*, "Bulk metallic glass mold for high volume fabrication of micro optics," *Microsystem Technologies,* vol. 22, no. 3, pp. 617-623, 2016.

[3] Z. Xiao-Qun, B. N. K. Ann, and K. S. Seong, "Single aspherical lens for deastigmatism, collimation, and circularization of a laser beam," *Applied Optics,* vol. 39, no. 7, pp. 1148-1151, 2000.

[4] M. Serkan and H. Kirkici, "Optical beam-shaping design based on aspherical lenses for circularization, collimation, and expansion of elliptical laser beams," *Applied optics,* vol. 47, no. 2, pp. 230-241, 2008.

[5] H. Yumoto *et al.*, "Focusing of X-ray free-electron laser pulses with reflective optics," *Nature Photonics,* vol. 7, no. 1, pp. 43-47, 2013.

[6] V. V. Strelkov, "High-order optical processes in intense laser field: Towards nonperturbative nonlinear optics," *Physical Review A,* vol. 93, no. 5, p. 053812, 2016.

[7] K. Matsusaka, S. Ozawa, R. Yoshida, T. Yuasa, and Y. Souma, "Ultracompact optical zoom lens for mobile phone," in *Digital Photography III*, 2007, vol. 6502: SPIE, pp. 9-18.

[8] Y. C. Fang, H. L. Tsai, and Y. H. Chien, "2x optical digital zoom lens with short total length and extremely small front aperture for two million pixel cmos on mobile phone," in *International Optical Design Conference*, 2006: Optica Publishing Group, p. WB6.

[9] M. Clampin, "Recent progress with the JWST Observatory," in *Space Telescopes and Instrumentation 2014: Optical, Infrared, and Millimeter Wave*, 2014, vol. 9143: SPIE, p. 914302.

[10] A. Saksena, "Quantum mechanically guided design of noble metal coatings for precision glass molding technology," Dissertation, Rheinisch-Westfälische Technische Hochschule Aachen, 2020, 2020.

[11] L. Zhang and W. Liu, "Precision glass molding: Toward an optimal fabrication of optical lenses," *Frontiers of Mechanical Engineering,* vol. 12, no. 1, pp. 3-17, 2017.

[12] C. Wagner and N. Harned, "Lithography gets extreme," *Nature Photonics,* vol. 4, no. 1, pp. 24-26, 2010.

[13] J. Li, S. Hu, and L. Zhao, "Study of the influence of the shape of projection lens focal plane on the focus control of advanced lithography," *Optik,* vol. 125, no. 22, pp. 6775-6777, 2014.

[14] K. Bobzin, F. Klocke, N. Bagcivan, M. Ewering, K. Georgiadis, and T. Münstermann, "Impact behaviour of PtIr-based coatings with different interlayers for glass lens moulding," in *Key Engineering Materials*, 2010, vol. 438: Trans Tech Publ, pp. 57-64.

[15] R. N. Doetsch, "History of the Microscope," *Science,* vol. 133, no. 3456, pp. 946-947, 1961.

[16] L. Gonick and W. Alschuler, "A brief history of the telescope," *Science,* vol. 323, no. 5912, pp. 330-331, 2009.

[17] C.-L. Chao, C.-B. Huo, W.-C. Chou, Y.-R. Lin, K.-J. Ma, and H.-H. Chien, "Study on the design of precious metal based protective films for glass moulding process," *Surface and Coatings Technology,* vol. 231, pp. 567-572, 2013.

[18] W. Liu and L. Zhang, "Thermoforming mechanism of precision glass moulding," *Applied optics,* vol. 54, no. 22, pp. 6841-6849, 2015.

[19] W. Ming *et al.*, "A comprehensive review of theory and technology of glass molding process," *The International Journal of Advanced Manufacturing Technology,* vol. 107, no. 5, pp. 2671-2706, 2020.

[20] J. Yan, T. Oowada, T. Zhou, and T. Kuriyagawa, "Precision machining of microstructures on electroless-plated NiP surface for molding glass components," *Journal of Materials Processing Technology,* vol. 209, no. 10, pp. 4802-4808, 2009.

[21] J. Y. Hou, C. S. Wang, and Y. Bai, "Research on crafts of Ni-P-SiC electroless composite plating on surface performances of the mould," in *Advanced Materials Research*, 2011, vol. 221: Trans Tech Publ, pp. 389-393.

[22] Y. Sawa, K. Yamashita, T. Kitadani, D. Noda, and T. Hattori, "Fabrication of high hardness Ni mold with electroless nickel–boron thin layer," *Microsystem technologies,* vol. 16, no. 8, pp. 1369-1375, 2010.

[23] K. S. Chon and Y. Namba, "Single-point diamond turning of electroless nickel for flat X-ray mirror," *Journal of mechanical science and technology,* vol. 24, no. 8, pp. 1603-1609, 2010.

[24] T. Yamaguchi, M. Higuchi, S. Shimada, and T. Kaneeda, "Tool life monitoring during the diamond turning of electroless Ni–P," *Precision Engineering,* vol. 31, no. 3, pp. 196-201, 2007.

[25] R. Parkinson, "Status of the nickel plating and electroforming industry," *Transactions of the Metal Finishers' Association of India(India),* vol. 5, no. 4, pp. 231-236, 1996.

[26] C.-L. Chao, C.-J. Chang, C.-C. Chen, W.-C. Chou, and K.-J. Ma, "Precision grinding of tungsten carbide mold insert for molding of sub-millimeter glass aspheric lenses," in *International Conference on Optics in Precision Engineering and Nanotechnology (icOPEN2013)*, 2013, vol. 8769: SPIE, pp. 491-497.

[27] J. Shin, S. Tanaka, and M. Esashi, "Nanostructured silicon carbide molds for glass press molding," in *2007 2nd IEEE International Conference on Nano/Micro Engineered and Molecular Systems*, 2007: IEEE, pp. 250-253.

[28] K.-O. Min, S. Tanaka, and M. Esashi, "Micro/nano glass press molding using silicon carbide molds fabricated by silicon lost molding," in *18th IEEE International Conference on Micro Electro Mechanical Systems, 2005. MEMS 2005.*, 2005: IEEE, pp. 475-478.

[29] A. N. Kumar and K. Kurokawa, "Spark plasma sintering of ultrafine WC powders: A combined kinetic and microstructural study," *Tungsten Carbide-Processing and Applications. InTech Open Publisher,* pp. 21-56, 2012.

[30] F. Klocke, O. Dambon, M. Rohwerder, F. Bernhardt, M. Friedrichs, and S. V. Merzlikin, "Model of coating wear degradation in precision glass molding," *The International Journal of Advanced Manufacturing Technology,* vol. 87, no. 1, pp. 43-49, 2016.

[31] H. Maehara and H. Murakoshi, "Quartz glass molding by precision glass molding method," *Transactions-institute of electrical engineers of japan e publication of sensors and micromachines society,* vol. 122, no. 10, pp. 494-497, 2002.

[32] W. Liu, M. Liu, and L. Zhang, "Oxidation-induced mechanical deterioration and hierarchical cracks in glassy carbon," *Carbon,* vol. 100, pp. 178-186, 2016.

[33] K.-H. Kim, K.-J. Hwang, H. Lee, S.-M. Jeong, M.-H. Lee, and S.-Y. Bae, "Improvement of adhesion properties of glass prepared using SiC-deposited graphite mold via low-temperature chemical vapor deposition," *Journal of the Korean Ceramic Society,* vol. 57, no. 1, pp. 112-118, 2020.

[34] K. J. Ma, H. Chien, W. Chuan, C. L. Chao, and K. Hwang, "Design of protective coatings for glass lens molding," in *Key Engineering Materials*, 2008, vol. 364: Trans Tech Publ, pp. 655-661.

[35] Y. Song, "Introduction: Progress of Thin Films and Coatings," *Inorganic and Organic Thin Films: Fundamentals, Fabrication and Applications,* vol. 1, pp. 1-58, 2021.

[36] S. Kumar and D. Aswal, "Thin Film and Significance of Its Thickness," in *Recent Advances in Thin Films*: Springer, 2020, pp. 1-12.

[37] S. Baydoun, P. Arnaud, and S. Fouvry, "Explicit formulations of adhesive wear extension in fretting interfaces applying the contact oxygenation concept," *Wear,* vol. 488, p. 204147, 2022.

[38] M. Lavella and D. Botto, "Fretting wear damage mechanism of CoMoCrSi coatings," *Wear,* vol. 477, p. 203896, 2021.

[39] C. Glynn and C. O'Dwyer, "Solution processable metal oxide thin film deposition and material growth for electronic and photonic devices," *Advanced Materials Interfaces,* vol. 4, no. 2, p. 1600610, 2017.

[40] C.-Y. Kang, Y.-I. Chen, C.-H. Lin, and J.-G. Duh, "Mechanical properties of Mo–Ru thin films with Ni interlayer of different thickness," *Applied surface science,* vol. 253, no. 14, pp. 6191-6195, 2007.

[41] F. Vaz and L. Rebouta, "Superhard nanocomposite ti-si-n coatings," in *Materials science forum*, 2002, vol. 383: Trans Tech Publ, pp. 143-150.

[42] S. Anders, A. Anders, J. Kortright, K. M. Yu, I. Brown, and I. Ivanov, "Vacuum arc deposition of multilayer X-ray mirrors," *Surface and Coatings Technology,* vol. 61, no. 1-3, pp. 257-261, 1993.

[43] E. Bemporad, M. Sebastiani, C. Pecchio, and S. De Rossi, "High thickness Ti/TiN multilayer thin coatings for wear resistant applications," *Surface and Coatings Technology,* vol. 201, no. 6, pp. 2155-2165, 2006.

[44] C. L. Chao, C. B. Huo, W.-C. Chou, Y. R. Lin, K. J. Ma, and H. H. Chien, "Study on the design of precious metal based protective films for glass moulding process," *Surface and Coatings Technology,* vol. 231, pp. 567-572, 2013.

[45] L. Zhang, G. Liu, X. Zhao, O. Dambon, F. Klocke, and A. Yi, "Precision molding of optics: a review of its development and applications," in *Polymer Optics and Molded Glass Optics: Design, Fabrication, and Materials 2016*, 2016, vol. 9949: International Society for Optics and Photonics, p. 994906.

[46] G. S. Upadhyaya, *Cemented tungsten carbides: production, properties and testing*. William Andrew, 1998.

[47] F. Bernhardt, "Faster mold coating tests make glass processing more efficient," *Photonics Spectra,* vol. 47, no. 8, pp. 36-39, 2013.

[48] J. Brand, R. Gadow, and A. Killinger, "Application of diamond-like carbon coatings on steel tools in the production of precision glass components," *Surface and Coatings Technology,* vol. 180, pp. 213-217, 2004.

[49] Y.-I. Chen, B.-L. Lin, Y.-C. Kuo, J.-C. Huang, L.-C. Chang, and Y.-T. Lin, "Preparation and annealing study of TaNx coatings on WC-Co substrates," *Applied surface science,* vol. 257, no. 15, pp. 6741-6749, 2011.

[50] K. D. Fischbach *et al.*, "Investigation of the effects of process parameters on the glass-to-mold sticking force during precision glass molding," *Surface and Coatings Technology,* vol. 205, no. 2, pp. 312-319, 2010.

[51] C.-H. Lin, J.-G. Duh, and B.-S. Yau, "Processing of chromium tungsten nitride hard coatings for glass molding," *Surface and Coatings Technology,* vol. 201, no. 3-4, pp. 1316-1322, 2006.

[52] C. L. Chao *et al.*, "Investigation of the interfacial reaction between optical glasses and various protective films and mold materials," in *Defect and Diffusion Forum*, 2010, vol. 297: Trans Tech Publ, pp. 808-813.

[53] S.-C. Liu, Y.-I. Chen, H.-Y. Tsai, K.-C. Lin, and Y.-H. Chen, "Thermal stability of Ir–Re coatings annealed in oxygen-containing atmospheres," *Surface and Coatings Technology,* vol. 237, pp. 105-111, 2013.

[54] F. Bernhardt, K. Georgiadis, L. Dolle, O. Dambon, and F. Klocke, "Development of a ta-C diamond-like carbon (DLC) coating by magnetron sputtering for use in precision glass molding," *Materialwissenschaft und Werkstofftechnik,* vol. 44, no. 8, pp. 661-666, 2013.

[55] Z. Xie, L. Wang, X. Wang, L. Huang, Y. Lu, and J. Yan, "Influence of high temperature annealing on the structure, hardness and tribological properties of diamond-like carbon and TiAlSiCN nanocomposite coatings," *Applied surface science,* vol. 258, no. 3, pp. 1206-1211, 2011.

[56] T.-N. Lin, S. Han, K.-W. Weng, and C.-T. Lee, "Investigation on the structural and mechanical properties of anti-sticking sputtered tungsten chromium nitride films," *Thin Solid Films,* vol. 529, pp. 333-337, 2013.

[57] M. Friedrichs, Z. Peng, T. Grunwald, M. Rohwerder, B. Gault, and T. Bergs, "PtIr protective coating system for precision glass molding tools: Design, evaluation and mechanism of degradation," *Surface and Coatings Technology,* vol. 385, p. 125378, 2020.

[58] H. Toku, R. Pessoa, H. Maciel, M. Massi, and U. Mengui, "Influence of process parameters on the growth of pure-phase anatase and rutile TiO2 thin films deposited by low temperature reactive magnetron sputtering," *Brazilian Journal of Physics,* vol. 40, no. 3, pp. 340-343, 2010.

[59] J. Alami, "Plasma Characterization & Thin Film Growth and Analysis in Highly Ionized Magnetron Sputtering," Institutionen för fysik, kemi och biologi, 2005.

[60] S. Hashmi, *Comprehensive materials processing*. Newnes, 2014.

[61] P. Martin, *Introduction to surface engineering and functionally engineered materials*. John Wiley & Sons, 2011.

[62] P. M. Martin, *Handbook of deposition technologies for films and coatings: science, applications and technology*. William Andrew, 2009.

[63] M. Aliofkhazraei and N. Ali, "PVD Technology in fabrication of micro-and nanostructured coatings," 2014.

[64] S. Tung and Y. Cheng, "Tribological characteristics and microstructures of PVD thin film coatings on steel substrates," in *Proceedings of the International Wear Conference, San Francisco, California*, 1993, pp. 12-17.

[65] M. Okumiya and M. Griepentrog, "Mechanical properties and tribological behavior of TiN–CrAlN and CrN–CrAlN multilayer coatings," *Surface and Coatings Technology,* vol. 112, no. 1-3, pp. 123-128, 1999.

[66] S. Schiller, K. Goedicke, J. Reschke, V. Kirchhoff, S. Schneider, and F. Milde, "Pulsed magnetron sputter technology," *Surf. Coat. Technol,* vol. 61, pp. 331-337, 1993.

[67] F.-b. Wu, W.-y. Chen, J.-g. Duh, Y.-y. Tsai, and Y.-i. Chen, "Ir-based multi-component coating on tungsten carbide by RF magnetron sputtering process," *Surface and Coatings Technology,* vol. 163, pp. 227-232, 2003.

[68] Y.-I. Chen, Y.-R. Cheng, L.-C. Chang, and J.-W. Lee, "Chemical inertness of Cr–W–N coatings in glass molding," *Thin Solid Films,* vol. 593, pp. 102-109, 2015.

[69] F. Klocke, K.-D. Bouzakis, K. Georgiadis, S. Gerardis, G. Skordaris, and M. Pappa, "Adhesive interlayers' effect on the entire structure strength of glass molding tools' Pt–Ir coatings by nano-tests determined," *Surface and Coatings Technology,* vol. 206, no. 7, pp. 1867-1872, 2011.

[70] K. Bewilogua *et al.*, "Surface technology for automotive engineering," *CIRP annals,* vol. 58, no. 2, pp. 608-627, 2009.

[71] D. M. Mattox and V. H. Mattox, "years of vacuum coating technology and the growth of the Society of Vacuum Coaters," in *Society of Vacuum Coaters*, 2007, pp. 32-86.

[72] C. Metzner and B. Scheffel, "Special aspects concerning the electron beam deposition of multi-component alloys," *Surface and Coatings Technology,* vol. 146, pp. 491-497, 2001.

[73] A. Lokhande *et al.*, "Development of Cu2SnS3 (CTS) thin film solar cells by physical techniques: A status review," *Solar Energy Materials and Solar Cells,* vol. 153, pp. 84-107, 2016.

[74] A. Zoeller, R. Goetzelmann, H. Hagedorn, W. Klug, and K. Matl, "Plasma-ion-assisted deposition: a powerful technology for the production of optical coatings," in *Optical thin films V: new developments*, 1997, vol. 3133: International Society for Optics and Photonics, pp. 196-204.

[75] S. Wen, R. Zong, F. Zeng, Y. Gu, Y. Gao, and F. Pan, "Thermal stability of microstructure and mechanical properties of Ni/Ru multilayers," *Surface and Coatings Technology,* vol. 202, no. 10, pp. 2040-2046, 2008.

[76] A. Jilani, M. S. Abdel-Wahab, and A. H. Hammad, "Advance deposition techniques for thin film and coating," *Modern Technologies for Creating the Thin-film Systems and Coatings,* vol. 2, pp. 137-149, 2017.

[77] J.-W. Seong and K. Yoon, "Effect of oxygen content on barrier properties of silicon oxide thin film deposited by dual ion-beam sputtering," *Journal of non-crystalline solids,* vol. 352, no. 1, pp. 84-91, 2006.

[78] E. Schäffer and G. Kleer, "Mechanical behavior of (Ti, Al) N coatings exposed to elevated temperatures and an oxidative environment," *Surface and Coatings Technology,* vol. 133, pp. 215-219, 2000.

[79] G. Wang and H. Zreiqat, "Functional coatings or films for hard-tissue applications," *Materials,* vol. 3, no. 7, pp. 3994-4050, 2010.

[80] O. O. Abegunde, E. T. Akinlabi, O. P. Oladijo, S. Akinlabi, and A. U. Ude, "Overview of thin film deposition techniques," *AIMS Materials Science,* vol. 6, no. 2, p. 174, 2019.

[81] S. Kommu, G. M. Wilson, and B. Khomami, "A theoretical/experimental study of silicon epitaxy in horizontal single-wafer chemical vapor deposition reactors," *Journal of The Electrochemical Society,* vol. 147, no. 4, p. 1538, 2000.

[82] H. Pedersen and S. D. Elliott, "Studying chemical vapor deposition processes with theoretical chemistry," *Theoretical Chemistry Accounts,* vol. 133, no. 5, p. 1476, 2014.

[83] K. Seshan, *Handbook of thin film deposition processes and techniques*. William Andrew, 2001.

[84] P. He, L. Li, H. Li, J. Yu, L. J. Lee, and Y. Y. Allen, "Compression molding of glass freeform optics using diamond machined silicon mold," *Manufacturing Letters,* vol. 2, no. 2, pp. 17-20, 2014.

[85] Y. Zhang, G. Yan, K. You, and F. Fang, "Study on α-Al2O3 anti-adhesion coating for molds in precision glass molding," *Surface and Coatings Technology,* vol. 391, p. 125720, 2020.

[86] S.-M. Park, T. Ikegami, K. Ebihara, and P.-K. Shin, "Structure and properties of transparent conductive doped ZnO films by pulsed laser deposition," *applied surface science,* vol. 253, no. 3, pp. 1522-1527, 2006.

[87] J.-O. Carlsson and P. M. Martin, "Chemical vapor deposition," in *Handbook of Deposition Technologies for films and coatings*: Elsevier, 2010, pp. 314-363.

[88] Y.-I. Chen, K.-T. Liu, F.-B. Wu, and J.-G. Duh, "Mo–Ru coatings on tungsten carbide by direct current magnetron sputtering," *Thin solid films,* vol. 515, no. 4, pp. 2207-2212, 2006.

[89] Y.-I. Chen, L.-C. Chang, J.-W. Lee, and C.-H. Lin, "Annealing and oxidation study of Mo–Ru hard coatings on tungsten carbide," *Thin Solid Films,* vol. 518, no. 1, pp. 194-200, 2009.

[90] H. H. Chien, K. J. Ma, C. H. Kuo, C. B. Huo, C. L. Chao, and Y. T. Chen, "The effect of TaN interlayer on the performance of Pt-Ir protective coatings in glass molding process," in *Defect and Diffusion Forum*, 2010, vol. 297: Trans Tech Publ, pp. 869-874.

[91] J. Sakurai, S. Hata, R. Yamuchi, M. Abe, and A. Shimokohbe, "Searching for Pt–Zr–Ni thin film amorphous alloys for optical glass lenses molding materials," *Precision Engineering,* vol. 34, no. 3, pp. 431-439, 2010.

[92] J. Masuda, J. Yan, T. Zhou, T. Kuriyagawa, and Y. Fukase, "Thermally induced atomic diffusion at the interface between release agent coating and mould substrate in a glass moulding press," *Journal of Physics D: Applied Physics,* vol. 44, no. 21, p. 215302, 2011.

[93] S.-F. Tseng, C.-T. Lee, K.-C. Huang, D. Chiang, C.-Y. Huang, and C.-P. Chou, "Mechanical properties of Pt-Ir and Ni-Ir binary alloys for glass-molding dies coating," *Journal of nanoscience and nanotechnology,* vol. 11, no. 10, pp. 8682-8688, 2011.

[94] K. Bobzin, N. Bagcivan, M. Ewering, R. Brugnara, and T. Münstermann, "Influence of interlayer thickness of a thin noble metal MSIP-PVD coating on compound and system properties for glass lens moulding," *Production Engineering,* vol. 6, no. 3, pp. 311-318, 2012.

[95] K. Bobzin and N. Bagcivan, "Correlation between chemical glass components and the glass sticking on sputtered PtIr physical vapour deposition coatings for precision blank moulding," *Materials sciences and applications,* vol. 2014, 2014.

[96] Y.-I. Chen, K.-Y. Lin, H.-H. Wang, and Y.-R. Cheng, "Characterization of Ta–Si–N coatings prepared using direct current magnetron co-sputtering," *Applied surface science,* vol. 305, pp. 805-816, 2014.

[97] Y.-I. Chen, K.-Y. Lin, H.-H. Wang, and K.-C. Lin, "Thermal stability of TaN, CrTaN, TaSiN, and CrTaSiN hard coatings in oxygen-containing atmospheres," *Surface and Coatings Technology,* vol. 259, pp. 159-166, 2014.

[98] Y.-I. Chen and H.-H. Wang, "Oxidation resistance and mechanical properties of Cr–Ta–Si–N coatings in glass molding processes," *Surface and Coatings Technology,* vol. 260, pp. 118-125, 2014.

[99] Z. Peng *et al.*, "Atomic diffusion induced degradation in bimetallic layer coated cemented tungsten carbide," *Corrosion Science,* vol. 120, pp. 1-13, 2017.

[100] L.-C. Chang, Y.-Z. Zheng, Y.-I. Chen, S.-C. Chang, and B.-W. Liu, "Bonding characteristics and chemical inertness of Zr–Si–N coatings with a high Si content in glass molding," *Coatings,* vol. 8, no. 5, p. 181, 2018.

[101] S.-H. Lee, I.-H. Ko, and T.-Y. Kim, "Surface failure analysis of AlCrN coating on WC substrate subjected to high-temperature oxidation in glass-molding machine," *Applied Surface Science,* vol. 452, pp. 210-216, 2018.

[102] J. Wei, X. Zhu, L. Chen, J. Liu, and C. Li, "High quality anti-sticking coating based on multilayer structure," *Surface and Coatings Technology,* vol. 362, pp. 72-77, 2019.

[103] X. Huang *et al.*, "Microstructure, wear and oxidation resistance of CrWN glass molding coatings synthesized by plasma enhanced magnetron sputtering," *Vacuum,* vol. 174, p. 109206, 2020.

[104] Y.-I. Chen, Y.-E. Ke, M.-C. Sung, and L.-C. Chang, "Rapid thermal annealing of Cr–Si–N, Ta–Si–N, and Zr–Si–N coatings in glass molding atmospheres," *Surface and Coatings Technology,* vol. 389, p. 125662, 2020.

[105] K. Li, G. Xu, X. Huang, Q. Chen, Z. Xie, and F. Gong, "Surface evolution analysis of CrxWyNz coatings on WC mold in glass molding process," *Surface and Coatings Technology,* vol. 393, p. 125839, 2020.

[106] F. Guo *et al.*, "Understanding the age-hardening mechanism of CrWN coating," *Thin Solid Films,* vol. 711, p. 138298, 2020.

[107] F. Klocke, T. Bergs, K. Georgiadis, H. Sarikaya, and F. Wang, "Coating systems for precision glass molding tools," in *Proc. 7th Int. Conf. Coatings Manuf. Eng*, 2008, pp. 209-218.

[108] F. Klocke, O. Dambon, and K. Georgiadis, "Comparison of nitride and noble metal coatings for precision glass molding tools," in *Key Engineering Materials*, 2010, vol. 438: Trans Tech Publ, pp. 9-16.

[109] X.-y. Zhu *et al.*, "Anti-sticking Re-Ir coating for glass molding process," *Thin Solid Films,* vol. 584, pp. 305-309, 2015/06/01/ 2015.

[110] D. Zhong *et al.*, "Wettability of NiAl, Ni-Al-N, Ti-B-C, and Ti-B-C-N films by glass at high temperatures," *Surface and Coatings Technology,* vol. 133-134, pp. 8-14, 2000/11/01/ 2000.

[111] H.-K. Lyeo and D. G. Cahill, "Thermal conductance of interfaces between highly dissimilar materials," *Physical Review B,* vol. 73, no. 14, p. 144301, 2006.

[112] B. C. Gundrum, D. G. Cahill, and R. S. Averback, "Thermal conductance of metal-metal interfaces," *Physical Review B,* vol. 72, no. 24, p. 245426, 2005.

[113] S. Bull, Jones, and AM, "Multilayer coatings for improved performance," *Surface and Coatings Technology,* vol. 78, no. 1-3, pp. 173-184, 1996.

[114] M. Khadem, O. V. Penkov, H.-K. Yang, and D.-E. Kim, "Tribology of multilayer coatings for wear reduction: A review," *Friction,* vol. 5, no. 3, pp. 248-262, 2017.

[115] Q. Yang and L. Zhao, "Thermal stability of polycrystalline TiN/CrN superlattice coatings," *Journal of Vacuum Science & Technology A: Vacuum, Surfaces, and Films,* vol. 21, no. 3, pp. 558-562, 2003.

[116] X. Chu and S. A. Barnett, "Model of superlattice yield stress and hardness enhancements," *Journal of Applied Physics,* vol. 77, no. 9, pp. 4403-4411, 1995.

[117] A. Brown and M. Ashby, "Correlations for diffusion constants," *Acta Metallurgica,* vol. 28, no. 8, pp. 1085-1101, 1980.

[118] H. Mehrer, *Diffusion in solids: fundamentals, methods, materials, diffusion-controlled processes*. Springer Science & Business Media, 2007.

[119] L. Harrison, "Influence of dislocations on diffusion kinetics in solids with particular reference to the alkali halides," *Transactions of the Faraday Society,* vol. 57, pp. 1191-1199, 1961.

[120] J. Poate, P. Turner, W. DeBonte, and J. Yahalom, "Thin-film interdiffusion. I. Au-Pd, Pd-Au, Ti-Pd, Ti-Au, Ti-Pd-Au, and Ti-Au-Pd," *Journal of Applied Physics,* vol. 46, no. 10, pp. 4275-4283, 1975.

[121] H. Tompkins and M. Pinnel, "Low-temperature diffusion of copper through gold," *Journal of Applied Physics,* vol. 47, no. 9, pp. 3804-3812, 1976.

[122] C. A. Chang, "Effect of CO on the low temperature diffusion of Cr and Si through thin gold films," *Journal of The Electrochemical Society,* vol. 127, no. 6, p. 1331, 1980.

[123] J. Lee, H. Jeong, C. S. Yoon, C. K. Kim, B. G. Park, and T. D. Lee, "Interdiffusion in antiferromagnetic/ferromagnetic exchange coupled NiFe/IrMn/CoFe multilayer," *Journal of applied physics,* vol. 91, no. 3, pp. 1431-1435, 2002.

[124] J. Rairden, C. Neugebauer, and R. Sigsbee, "Interdiffusion in thin conductor films—chromium/gold, nickel/gold and chromium silicide/gold," *Metallurgical Transactions,* vol. 2, no. 3, pp. 719-722, 1971.

[125] A. Hiraki, E. Lugujjo, and J. W. Mayer, "Formation of silicon oxide over gold layers on silicon substrates," *Journal of Applied Physics,* vol. 43, no. 9, pp. 3643-3649, 1972.

[126] H. Tompkins and M. Pinnel, "Relative rates of nickel diffusion and copper diffusion through gold," *Journal of Applied Physics,* vol. 48, no. 7, pp. 3144-3146, 1977.

[127] U. Gösele and K.-N. Tu, "Growth kinetics of planar binary diffusion couples:''Thin-film case''versus''bulk cases'','' *Journal of Applied Physics,* vol. 53, no. 4, pp. 3252-3260, 1982.

[128] C. Canali, F. Catellani, G. Ottaviani, and M. Prudenziati, "On the formation of Ni and Pt silicide first phase: the dominant role of reaction kinetics," *Applied Physics Letters,* vol. 33, no. 2, pp. 187-190, 1978.

[129] G. Ottaviani, "Review of binary alloy formation by thin film interactions," *Journal of vacuum science and technology,* vol. 16, no. 5, pp. 1112-1119, 1979.

[130] G. Ottaviani and M. Costato, "Compound formation in metal—semiconductor interactions," *Journal of Crystal Growth,* vol. 45, pp. 365-375, 1978.

[131] E. Colgan, B. Tsaur, and J. Mayer, "Phase formation in Cr-Si thin-film interactions," *Applied Physics Letters,* vol. 37, no. 10, pp. 938-940, 1980.

[132] K.-N. Tu, "Interdiffusion in thin films," *Annual Review of Materials Science,* vol. 15, no. 1, pp. 147-176, 1985.

[133] J. M. Poate, K.-n. Tu, and J. W. Mayer, *Thin films: interdiffusion and reactions*. John Wiley & Sons, 1978.

[134] K. Zeng, R. Stierman, T.-C. Chiu, D. Edwards, K. Ano, and K.-N. Tu, "Kirkendall void formation in eutectic SnPb solder joints on bare Cu and its effect on joint reliability," *Journal of applied physics,* vol. 97, no. 2, p. 024508, 2005.

[135] A. Paul, T. Laurila, V. Vuorinen, and S. V. Divinski, *Thermodynamics, diffusion and the Kirkendall effect in solids*. Springer, 2014.

[136] H. Springer, A. Kostka, J. F. Dos Santos, and D. Raabe, "Influence of intermetallic phases and Kirkendall-porosity on the mechanical properties of

joints between steel and aluminium alloys," *Materials Science and Engineering: A,* vol. 528, no. 13-14, pp. 4630-4642, 2011.

[137] P. He *et al.*, "Graphene-coated Si mold for precision glass optics molding," *Optics letters,* vol. 38, no. 14, pp. 2625-2628, 2013.

[138] S.-C. Liu *et al.*, "The chemical inertness of Ir–Re and Ta–Ru coatings in molding B2O3–ZnO–La2O3-based glass," *Surface and Coatings Technology,* vol. 259, pp. 352-357, 2014.

[139] Y.-I. Chen and B.-N. Tsai, "Internal oxidation mechanism for Ta–Ru and Mo–Ru coatings," *Thin solid films,* vol. 519, no. 15, pp. 4974-4980, 2011.

[140] S. Bajt *et al.*, "Oxidation resistance of Ru-capped EUV multilayers," in *Emerging Lithographic Technologies IX*, 2005, vol. 5751: SPIE, pp. 118-127.

[141] H. Lee, R. A. Coutu, S. Mall, and K. D. Leedy, "Characterization of metal and metal alloy films as contact materials in MEMS switches," *Journal of Micromechanics and Microengineering,* vol. 16, no. 3, p. 557, 2006.

[142] C. Li, R. Dai, R. Qi, X. Wu, and J. Ma, "Electrodeposition of Pt–Ru alloy electrocatalysts for direct methanol fuel cell," *Int. J. Electrochem. Sci,* vol. 12, pp. 2485-2494, 2017.

[143] J. H. Han *et al.*, "Chemical vapor deposition of Ru thin films with an enhanced morphology, thermal stability, and electrical properties using a RuO4 precursor," *Chemistry of Materials,* vol. 21, no. 2, pp. 207-209, 2009.

[144] Y.-I. Chen and B.-N. Tsai, "Annealing and oxidation study of Ta–Ru hard coatings," *Surface and Coatings Technology,* vol. 205, no. 5, pp. 1362-1367, 2010.

[145] A. S. Khanna, *Introduction to high temperature oxidation and corrosion*. ASM international, 2002.

[146] D. Douglass, "A critique of internal oxidation in alloys during the post-Wagner era," *Oxidation of Metals,* vol. 44, no. 1, pp. 81-111, 1995.

[147] Y.-I. Chen, Y.-C. Kuo, and S.-M. Chen, "Oxidation study of Cr–Ru hard coatings," *Thin solid films,* vol. 520, no. 6, pp. 2066-2072, 2012.

[148] R. Wuhrer and W. Yeung, "Grain refinement with increasing magnetron discharge power in sputter deposition of nanostructured titanium aluminium nitride coatings," *Scripta Materialia,* vol. 50, no. 6, pp. 813-818, 2004.

[149] P. Hones, R. Consiglio, N. Randall, and F. Levy, "Mechanical properties of hard chromium tungsten nitride coatings," *Surface and Coatings Technology,* vol. 125, no. 1-3, pp. 179-184, 2000.

[150] R. Kalish, Y. Lifshitz, K. Nugent, and S. Prawer, "Thermal stability and relaxation in diamond-like-carbon. A Raman study of films with different sp 3 fractions (ta-C to a-C)," *Applied physics letters,* vol. 74, no. 20, pp. 2936-2938, 1999.

[151] J. Schwan *et al.*, "Tetrahedral amorphous carbon films prepared by magnetron sputtering and dc ion plating," *Journal of applied physics,* vol. 79, no. 3, pp. 1416-1422, 1996.

[152] S. Zhang, D. Sun, Y. Fu, and H. Du, "Recent advances of superhard nanocomposite coatings: a review," *Surface and Coatings Technology,* vol. 167, no. 2-3, pp. 113-119, 2003.

[153] K.-D. Bouzakis *et al.*, "The influence of the coating thickness on its strength properties and on the milling performance of PVD coated inserts," *Surface and Coatings Technology,* vol. 174, pp. 393-401, 2003.

[154] W. D. Nix, "Mechanical properties of thin films," *Metallurgical transactions A,* vol. 20, no. 11, p. 2217, 1989.

[155] K. Yu-Zhang, J. Embury, K. Han, and A. Misra, "Transmission electron microscopy investigation of the atomic structure of interfaces in nanoscale Cu–Nb multilayers," *Philosophical Magazine,* vol. 88, no. 17, pp. 2559-2567, 2008.

[156] J. Tomastik and R. Ctvrtlik, "Nanoscratch test—A tool for evaluation of cohesive and adhesive properties of thin films and coatings," in *EPJ web of conferences*, 2013, vol. 48: EDP Sciences, p. 00027.

[157] B. Beake, A. Harris, and T. Liskiewicz, "Review of recent progress in nanoscratch testing," *Tribology-Materials, Surfaces & Interfaces,* vol. 7, no. 2, pp. 87-96, 2013.

[158] I. Kartsonakis, A. Balaskas, E. Koumoulos, C. Charitidis, and G. Kordas, "Incorporation of ceramic nanocontainers into epoxy coatings for the corrosion protection of hot dip galvanized steel," *Corrosion science,* vol. 57, pp. 30-41, 2012.

[159] E. Frutos, J. L. González-Carrasco, and T. Polcar, "Repetitive nano-impact tests as a new tool to measure fracture toughness in brittle materials," *Journal of the European Ceramic Society,* vol. 36, no. 13, pp. 3235-3243, 2016.

[160] X. Huang *et al.*, "Effect of annealing environment on the microstructure and mechanical property of CrWN glass molding coating," *Surface and Coatings Technology,* vol. 383, p. 125281, 2020.

[161] L.-C. Chang, B.-W. Liu, and Y.-I. Chen, "Mechanical properties and oxidation behavior of multilayered Hf–Si–N coatings," *Coatings,* vol. 8, no. 10, p. 354, 2018.

[162] C. Mitterer, "2.16 - PVD and CVD Hard Coatings," in *Comprehensive Hard Materials*, V. K. Sarin Ed. Oxford: Elsevier, 2014, pp. 449-467.

[163] X. Li *et al.*, "Effect of annealing on the hardness and microstructure of Cr-Zr-O coatings," *Surface and Coatings Technology,* vol. 426, p. 127792, 2021/11/25/ 2021.

[164] D. D. Le Pevelen, "Small Molecule X-Ray Crystallography, Theory and Workflow," in *Encyclopedia of Spectroscopy and Spectrometry (Second Edition)*, J. C. Lindon Ed. Oxford: Academic Press, 2010, pp. 2559-2576.

[165] R. Saha and W. D. Nix, "Effects of the substrate on the determination of thin film mechanical properties by nanoindentation," *Acta materialia,* vol. 50, no. 1, pp. 23-38, 2002.

[166] W. C. Oliver and G. M. Pharr, "Measurement of hardness and elastic modulus by instrumented indentation: Advances in understanding and refinements to methodology," *Journal of materials research,* vol. 19, no. 1, pp. 3-20, 2004.

[167] B. Fultz and J. M. Howe, *Transmission electron microscopy and diffractometry of materials*. Springer Science & Business Media, 2012.

[168] D. Fan and L. Q. Chen, "Computer simulation of grain growth using a continuum field model," *Acta Materialia,* vol. 45, no. 2, pp. 611-622, 1997, doi: 10.1016/s1359-6454(96)00200-5.

[169] N. Moelans, B. Blanpain, and P. Wollants, "A phase field model for the simulation of grain growth in materials containing finely dispersed incoherent second-phase particles," *Acta Materialia,* vol. 53, no. 6, pp. 1771-1781, 2005, doi: 10.1016/j.actamat.2004.12.026.

[170] K. Ammar, B. Appolaire, G. Cailletaud, F. Feyel, and S. Forest, "Finite element formulation of a phase field model based on the concept of generalized stresses," *Computational Materials Science,* vol. 45, no. 3, pp. 800-805, 2009, doi: 10.1016/j.commatsci.2008.09.015.

[171] J. Kundin, R. Siquieri, and H. Emmerich, "A quantitative multi-phase-field modeling of the microstructure evolution in a peritectic Al–Ni alloy," *Physica D: Nonlinear Phenomena,* vol. 243, no. 1, pp. 116-127, 2013, doi: 10.1016/j.physd.2012.10.004.

[172] J. Li, S. Hu, Y. Li, and S.-Q. Shi, "A multi-phase-field model of topological pattern formation during electrochemical dealloying of binary alloys," *Computational Materials Science,* vol. 203, 2022, doi: 10.1016/j.commatsci.2021.111103.

[173] A. C. S. Sabioni, A. M. Huntz, F. Millot, and C. Monty, "Self-diffusion in cr2o3III. Chromium and oxygen grain-boundary diffusion in polycrystals," *Philosophical Magazine A,* vol. 66, no. 3, pp. 361-374, 1992, doi: 10.1080/01418619208201562.

[174] P. Kofstad and K. P. Lillerud, "Chromium transport through Cr2O3 scales I. On lattice diffusion of chromium," *Oxidation of Metals,* vol. 17, no. 3-4, pp. 177-194, 1982, doi: 10.1007/bf00738381.

[175] A. C. S. Sabioni, A. M. Huntz, F. Millot, and C. Monty, "Self-diffusion in cr2o3II. Oxygen diffusion in single crystals," *Philosophical Magazine A,* vol. 66, no. 3, pp. 351-360, 1992, doi: 10.1080/01418619208201561.

[176] L. Chen *et al.*, "Modulation of dendritic patterns during electrodeposition: A nonlinear phase-field model," *Journal of Power Sources,* vol. 300, pp. 376-385, 2015, doi: 10.1016/j.jpowsour.2015.09.055.

[177] H. Jones, "The Surface Energy of Solid Metals," *Metal Science Journal,* vol. 5, no. 1, pp. 15-18, 2013, doi: 10.1179/030634571790439342.

[178] J. Manguele *et al.*, "Highly textured Pt thin film grown at very low temperature using Ca 2 Nb 3 O 10 nanosheets as seed layer," *SN Applied Sciences,* vol. 2, no. 3, pp. 1-10, 2020.

[179] M. Sreemany and S. Sen, "Effect of substrate temperature and annealing temperature on the structural, electrical and microstructural properties of thin

Pt films by rf magnetron sputtering," *Applied Surface Science,* vol. 253, no. 5, pp. 2739-2746, 2006.

[180] M. Arif, A. Sanger, P. M. Vilarinho, and A. Singh, "Effect of Annealing Temperature on Structural and Optical Properties of Sol-Gel-Derived ZnO Thin Films," *Journal of Electronic Materials,* vol. 47, no. 7, 2018.

[181] A. S. Gorzalski, C. Donley, and O. Coronell, "Elemental composition of membrane foulant layers using EDS, XPS, and RBS," *Journal of Membrane Science,* vol. 522, pp. 31-44, 2017.

[182] E. Kusano, A. Sato, N. Kikuchi, H. Nanto, and A. Kinbara, "Preparation of TiC films by alternate deposition of Ti and C layers using a dual magnetron sputtering source," *Surface and Coatings Technology,* vol. 120, pp. 378-382, 1999.

[183] Y.-J. Chiu *et al.*, "Nanoindentation study of FePt thin films deposited by radio frequency magnetron sputtering," *Nanoscience and Nanotechnology Letters,* vol. 8, no. 3, pp. 260-265, 2016.

[184] K. Vinokurov, Y. Bekenstein, V. Gutkin, I. Popov, O. Millo, and U. Banin, "Rhodium growth on Cu 2 S nanocrystals yielding hybrid nanoscale inorganic cages and their synergistic properties," *CrystEngComm,* vol. 16, no. 40, pp. 9506-9512, 2014.

[185] A. Obrosov *et al.*, "Chemical and morphological characterization of magnetron sputtered at different bias voltages Cr-Al-C coatings," *Materials,* vol. 10, no. 2, p. 156, 2017.

[186] M. Smith, L. Scudiero, J. Espinal, J.-S. McEwen, and M. Garcia-Perez, "Improving the deconvolution and interpretation of XPS spectra from chars by ab initio calculations," *Carbon,* vol. 110, pp. 155-171, 2016.

[187] E. Ciftyürek, K. Sabolsky, and E. M. Sabolsky, "Platinum thin film electrodes for high-temperature chemical sensor applications," *Sensors and Actuators B: Chemical,* vol. 181, pp. 702-714, 2013.

[188] K. Dückers, H. Bonzel, and D. Wesner, "Surface core level shifts of Pt (111) measured with Y Mχ radiation (132.3 eV)," *Surface Science,* vol. 166, no. 1, pp. 141-158, 1986.

[189] D. Chen *et al.*, "Ultra-high-performance core–shell structured Ru@Pt/C catalyst prepared by a facile pulse electrochemical deposition method," *Scientific Reports,* vol. 5, no. 1, p. 11604, 2015/08/03 2015, doi: 10.1038/srep11604.

[190] A. S. Ramos, S. Simões, L. Maj, J. Morgiel, and M. T. Vieira, "Effect of Deposition Parameters on the Reactivity of Al/Ni Multilayer Thin Films," *Coatings,* vol. 10, no. 8, p. 721, 2020.

[191] Z. Czigány and G. Radnóczi, "Columnar growth structure and evolution of wavy interface morphology in amorphous and polycrystalline multilayered thin films," *Thin Solid Films,* vol. 347, no. 1-2, pp. 133-145, 1999.

[192] N. Liu, L. Dong, S. Jin, R. Wan, H. Gu, and D. Li, "Significant impact of individual surface and modulation structure on mechanical properties of NbN/NbB2 multilayers," *Journal of Alloys and Compounds,* vol. 695, pp. 3225-3232, 2017.

[193] S.-D. Kim *et al.*, "Strain hardening recovery mediated by coherent precipitates in lightweight steel," *Scientific Reports,* vol. 11, no. 1, p. 14468, 2021/07/14 2021, doi: 10.1038/s41598-021-93795-4.

[194] E. Shkondin, H. Alimadadi, O. Takayama, F. Jensen, and A. V. Lavrinenko, "Fabrication of hollow coaxial Al2O3/ZnAl2O4 high aspect ratio freestanding nanotubes based on the Kirkendall effect," *Journal of Vacuum Science & Technology A: Vacuum, Surfaces, and Films,* vol. 38, no. 1, p. 013402, 2020.

[195] J. Embury and J. Hirth, "On dislocation storage and the mechanical response of fine scale microstructures," *Acta metallurgica et materialia,* vol. 42, no. 6, pp. 2051-2056, 1994.

[196] A. Misra, J. Hirth, R. Hoagland, J. Embury, and H. Kung, "Dislocation mechanisms and symmetric slip in rolled nano-scale metallic multilayers," *Acta materialia,* vol. 52, no. 8, pp. 2387-2394, 2004.

[197] Z. Yang and J. Wang, "Coupled annealing temperature and layer thickness effect on strengthening mechanisms of Ti/Ni multilayer thin films," *Journal of the Mechanics and Physics of Solids,* vol. 88, pp. 72-82, 2016.

[198] W.-R. Jian, S. Xu, Y. Su, and I. J. Beyerlein, "Role of layer thickness and dislocation distribution in confined layer slip in nanolaminated Nb," *International Journal of Plasticity,* vol. 152, p. 103239, 2022.

[199] J. Wang and X. Zhang, "Twinning effects on strength and plasticity of metallic materials," *Mrs Bulletin,* vol. 41, no. 4, pp. 274-281, 2016.

[200] W. Kwong and W. Zhang, "Electron-beam assisted platinum deposition as a protective layer for FIB and TEM applications," in *ISSM 2005, IEEE International Symposium on Semiconductor Manufacturing, 2005.*, 2005: IEEE, pp. 469-471.

[201] B. Wei, S. Ni, Y. Liu, X. Liao, and M. Song, "Phase Transformation and Deformation Mechanisms in a Cold-Rolled Ti-5at.% Al Alloy," *Available at SSRN 3390933,* 2019.

[202] U. Rothhaar and H. Oechsner, "Temperature induced dissolution of Cr2O3 into polycrystalline tantalum," *Thin Solid Films,* vol. 302, no. 1-2, pp. 266-269, 1997.

[203] P. Hones, M. Diserens, and F. Levy, "Characterization of sputter-deposited chromium oxide thin films," *Surface and coatings technology,* vol. 120, pp. 277-283, 1999.

[204] X. Pang *et al.*, "Annealing effects on microstructure and mechanical properties of chromium oxide coatings," *Thin Solid Films,* vol. 516, no. 15, pp. 4685-4689, 2008.

[205] F. Lai, C. Huang, C. Chang, L. Wang, and W. Cheng, "Ultra-thin Cr2O3 well-crystallized films for high transmittance APSM in ArF line," *Microelectronic engineering,* vol. 67, pp. 17-23, 2003.

[206] A. Akhtar, J. Wang, R. He, E. Yi Chun Wong, K. Hung, and H. Ruan, "Microstructural evaluation of sputtered Ru–Pt multilayer anti-stick coatings for glass molding," *Materials & Design,* vol. 220, p. 110898, 2022/08/01/ 2022.

[207] T. Nishino, T. Sakurai, and S. Nishiyama, "Oxidation Reaction of Chromium Oxide (Cr 2 O 3) in the Presence of Mm'O 3 (M: Ca, Sr, Ba; M': Ti, Zr)," in *Reactivity of Solids*: Springer, 1977, pp. 149-153.

[208] C. M. Cotell, G. J. Yurek, R. J. Hussey, D. F. Mitchell, and M. J. Graham, "The influence of grain-boundary segregation of Y in Cr2O3 on the oxidation of Cr metal," *Oxidation of Metals,* vol. 34, no. 3, pp. 173-200, 1990/10/01 1990, doi: 10.1007/BF00665014.

[209] Y. Nishihara, Y. Yamaguchi, M. Tokumoto, K. Takeda, and K. Fukamichi, "Superconductivity and magnetism of bcc Cr-Ru alloys," *Physical Review B,* vol. 34, no. 5, p. 3446, 1986.

[210] B. Matthias, T. Geballe, V. Compton, E. Corenzwit, and G. Hull Jr, "Superconductivity of chromium alloys," *Physical Review,* vol. 128, no. 2, p. 588, 1962.

[211] C. S. Tedmon, "The high-temperature oxidation of ductile Cr-Ru alloys," *Journal of the Less Common Metals,* vol. 10, no. 5, pp. 301-311, 1966/05/01/ 1966.

[212] L. Reddy, H. L. Alberts, A. R. E. Prinsloo, and A. M. Venter, "Antiferromagnetism in a Cr86Ru14 alloy," *Journal of Alloys and Compounds,* vol. 426, no. 1, pp. 83-92, 2006/12/21/ 2006.

[213] D. Sidelev *et al.*, "A comparative study on the properties of chromium coatings deposited by magnetron sputtering with hot and cooled target," *Vacuum,* vol. 143, pp. 479-485, 2017.

[214] S. Rezaee *et al.*, "Effect of annealing on the micromorphology and corrosion properties of Ti/SS thin films," *Superlattices and Microstructures,* vol. 146, p. 106681, 2020.

[215] A. Ul-Hamid, "Deposition, microstructure and nanoindentation of multilayer Zr nitride and carbonitride nanostructured coatings," *Scientific Reports,* vol. 12, no. 1, p. 5591, 2022/04/04 2022, doi: 10.1038/s41598-022-09449-6.

[216] V. Maurice, S. Cadot, and P. Marcus, "XPS, LEED and STM study of thin oxide films formed on Cr(110)," *Surface Science,* vol. 458, no. 1, pp. 195-215, 2000/06/20/ 2000.

[217] H. C. Barshilia and K. S. Rajam, "Growth and characterization of chromium oxide coatings prepared by pulsed-direct current reactive unbalanced magnetron sputtering," *Applied Surface Science,* vol. 255, no. 5, Part 2, pp. 2925-2931, 2008/12/30/ 2008.

[218] L. Zhong, Y. Yu, W. Cai, X. Geng, and Q. Zhong, "Structure–activity relationship of Cr/Ti-PILC catalysts using a pre-modification method for NO oxidation and their surface species study," *Physical Chemistry Chemical Physics,* vol. 17, no. 22, pp. 15036-15045, 2015.

[219] J. H. Chang *et al.*, "X-ray photoelectron spectroscopy study on the CrN surface grown on sapphire substrate to control the polarity of ZnO by plasma-assisted molecular beam epitaxy," *Applied Surface Science,* vol. 255, no. 20, pp. 8582-8586, 2009/07/30/ 2009.

[220] D. K. H. Briggs, "Handbook of X-ray Photoelectron Spectroscopy C. D. Wanger, W. M. Riggs, L. E. Davis, J. F. Moulder and G. E.Muilenberg Perkin-Elmer Corp., Physical Electronics Division, Eden Prairie, Minnesota, USA, 1979. 190 pp. ," *Surface and Interface Analysis,* vol. 3, 1981.

[221] G. Mauer and R. Vaßen, "Coatings with columnar microstructures for thermal barrier applications," *Advanced engineering materials,* vol. 22, no. 6, p. 1900988, 2020.

[222] V. Brien, P. Miska, B. Bolle, and P. Pigeat, "Columnar growth of ALN by rf magnetron sputtering: Role of the {1 0 1 3} planes," *Journal of crystal growth,* vol. 307, no. 1, pp. 245-252, 2007.

[223] S. Rezanka, C. Somsen, G. Eggeler, G. Mauer, R. Vaßen, and O. Guillon, "A TEM Investigation of columnar-structured thermal barrier coatings deposited by plasma spray-physical vapor deposition (PS-PVD)," *Plasma Chemistry and Plasma Processing,* vol. 38, no. 4, pp. 791-802, 2018.

[224] O. Cortazar-Martínez, J.-A. Torres-Ochoa, J.-G. Raboño-Borbolla, and A. Herrera-Gomez, "Oxidation mechanism of metallic chromium at room temperature," *Applied Surface Science,* vol. 542, p. 148636, 2021.

[225] D. Tytko, P.-P. Choi, and D. Raabe, "Oxidation behavior of AlN/CrN multilayered hard coatings," *Nano Convergence,* vol. 4, no. 1, pp. 1-5, 2017.

[226] R. Hussey and M. Graham, "The influence of reactive-element coatings on the high-temperature oxidation of pure-Cr and high-Cr-content alloys," *Oxidation of metals,* vol. 45, no. 3, pp. 349-374, 1996.

[227] N. Peterson, "Grain-boundary diffusion in metals," *International metals reviews,* vol. 28, no. 1, pp. 65-91, 1983.

[228] B. A. Watson, R. Süss, and L. Cornish, "Building a thermodynamic database for platinum-based superalloys: Part II," *Platinum Metals Review,* vol. 51, no. 4, pp. 189-198, 2007.

[229] K. Abu-Shgair, H. H. Abu-Safe, A. Aryasomayajula, B. Beake, and M. H. Gordon, "Characterizing crystalline chromium oxide thin film growth parameters," *Rev. Adv. Mater. Sci,* vol. 24, pp. 64-68, 2010.

[230] Z. Yang and S. C. Singhal, "Fuel cells –solid oxide fuel cells-Cell Interconnection," in *Encyclopedia of Electrochemical Power Sources*, J. Garche Ed. Amsterdam: Elsevier, 2009, pp. 63-76.

[231] A.-A. El Mel, R. Nakamura, and C. Bittencourt, "The Kirkendall effect and nanoscience: hollow nanospheres and nanotubes," *Beilstein journal of nanotechnology,* vol. 6, no. 1, pp. 1348-1361, 2015.

[232] M. Goral, R. Swadźba, and T. Kubaszek, "TEM investigations of TGO formation during cyclic oxidation in two-and three-layered Thermal Barrier Coatings produced using LPPS, CVD and PS-PVD methods," *Surface and Coatings Technology,* vol. 394, p. 125875, 2020.

[233] C. Tedmon Jr, "The high-temperature oxidation of ductile Cr-Ru alloys," *Journal of the Less Common Metals,* vol. 10, no. 5, pp. 301-311, 1966.

[234] R. Franchy, "Growth of thin, crystalline oxide, nitride and oxynitride films on metal and metal alloy surfaces," *Surface Science Reports,* vol. 38, no. 6-8, pp. 195-294, 2000.